Effect of Anisotropy on the Mechanical Testing of Ni-Based Single-Crystal Superalloys

Celal Polatoğlu

St Anne's College

University of Oxford

A thesis submitted for the degree of
M.Sc. by Research in Engineering Science

Supervised by
Prof. Roger C. Reed

Michaelmas Term 2023

بسم الله الرحمن الرحيم

Abstract

With the objective of generating the maximum energy possible from a given fuel supply, both the aerospace and power generation sectors are engaged in a continuous endeavour to enhance the efficiencies of gas turbine engines. Elevating the turbine entry temperature (TET) theoretically promises improved performance; but material limitations restrict the extent to which this can be achieved. Ni-based single-crystal superalloys, renowned for retaining their high yield strengths at extreme temperatures, have been created to break these boundaries. In this thesis, we investigate the mechanical properties of the Ni-based single-crystal superalloy STAL15 from three distinct angles.

Firstly, we conduct a comparative analysis of the material's mechanical behaviour in its $\langle 001 \rangle$ and $\langle 011 \rangle$ crystallographic orientations, aiming to add to the understanding of how the material is affected by changes in temperature and strain rate.

Secondly, we explore different yield strength definitions in order to understand how they are related to the anomalous yield phenomena, and if the presence of anomalous yield is dependent on the definition used.

Finally, we employ an orthogonal dual-camera setup using multiple digital extensometers to better analyse the mechanical properties of the single-crystal STAL15. This configuration proves instrumental for characterising the elastic anisotropy of both crystallographic orientations for different temperatures and strain rates.

Our approach combines mechanical tests, Digital Image Correlation (DIC), Scanning Electron Microscopy (SEM), and optical profilometry to analyse the material's mechanical properties and microstructural characteristics. We aim to provide the reader with an alternative perspective on how to approach not only the mechanical properties of STAL15, but all Ni-based single-crystal superalloys in general; potentially contributing to our understanding of this area.

Acknowledgements

I would like to begin by expressing my heartfelt gratitude to my supervisor, Prof. Roger C. Reed, for his unwavering support over the years. He consistently encouraged and guided me towards achieving excellence.

I am also grateful to our postdoctoral researchers, Dr. Yuanbo Tang and Dr. Satoshi Utada, for their invaluable contributions and assistance throughout the duration of this study. They have been exceptional mentors, and I couldn't have asked for better guidance.

Also a big thank you to my research group members and staff: Jieming Zhang, Hirokazu Usuki, Dr. Joseph Ghoussoub, Ryo Sasaki, Mrs. Karen Bamford, Prof. Graham McCartney, Dr. Yilun Gong, Hisham Elamin, Stuart Carter, Dr. Kalin Dragnevski and Chris Salter. You were all very helpful and kind. It was certainly a pleasure to meet you all.

Furthermore, I would like to thank the National Ministry of Education of the Republic of Türkiye (T.C.M.E.B.) for providing the scholarship that supported my academic pursuit. I would also like to extend my appreciation to Siemens Energy AB for generously providing the materials used in this research. Their support and resources have been pivotal in conducting experiments and ensuring the success of this study.

I would also like to extend my sincere gratitude to my examiners, Prof. Daniel Eakins and Prof. Cathie Rae, for their insightful feedback and constructive criticism during the examination of this thesis. Their expertise and thorough review have been invaluable in refining and improving my work.

Finally, I want to thank my family and friends. Your support has been a constant source of strength, and you have always been there for me whenever I've needed it.

Contents

1 Introduction **2**

2 Literature Review **6**

2.1 Nickel-Based Superalloys 6

2.1.1 Physical Metallurgy of Superalloys 7

2.1.1.1 The γ phase 7

2.1.1.2 The γ' phase 8

2.1.1.3 Carbides and Borides 8

2.1.1.4 Other Phases 9

2.2 Strengthening Mechanisms in Ni-Based Single-Crystal Superalloys . . 9

2.3 The Yield Strength Anomaly 12

2.4 Tensile Testing of Ni-based Single-Crystal Superalloys 17

2.5 Strain Localisation in Anisotropic Materials 21

2.6 Fractography Analysis of Ni-based Superalloys 22

2.6.1 Fracture Mechanisms 23

2.6.2 Effect of Temperature and Crystallographic Orientation on Fracture Characteristics 26

3 Comparison of Mechanical Properties in ⟨001⟩ and ⟨011⟩ Crystal Orientations of STAL15 Ni-Based Single-Crystal Superalloy **29**

3.1 Introduction 29

3.2 Experimental Procedures 30

3.2.1 Materials 30

3.2.2 Methods 30

3.3 Results and Discussion 32

3.3.1 Mechanical Testing 32

3.3.1.1 Effect of Temperature on ⟨001⟩ 33

3.3.1.2 Effect of Temperature on ⟨011⟩ 35

3.3.1.3 Effect of Strain Rate on ⟨011⟩ . . . 37
3.3.1.4 Comparison of Mechanical Properties . . . 39
3.4 Conclusions . . . 43

4 Defining Anomalous Yield: Is There Really an Increase in Yield Strength? 45
4.1 Introduction . . . 45
4.2 Experimental Procedures . . . 46
4.2.1 Materials . . . 46
4.2.2 Methods . . . 46
4.3 Results . . . 48
4.3.1 Mechanical Testing . . . 48
4.3.2 Scanning Electron Microscopy . . . 49
4.4 Discussion . . . 49
4.5 Conclusions . . . 57

5 Measurement Difficulties in Tensile Testing of Ni-Based Single-Crystal Superalloys 59
5.1 Introduction . . . 59
5.2 Experimental Procedures . . . 61
5.2.1 Materials . . . 61
5.2.2 Methods . . . 62
5.3 Results . . . 64
5.3.1 Mechanical Testing . . . 64
5.3.1.1 AD730 vs. STAL15 ⟨001⟩ . . . 64
5.3.1.2 STAL15 ⟨001⟩ vs. STAL15 ⟨011⟩ . . . 67
5.3.1.3 Strain Rates of 10^{-3} s^{-1}, 10^{-2} s^{-1}, 10^{-1} s^{-1} . . . 69
5.3.1.4 Temperatures of 825 °C, 850 °C, 875 °C, 900 °C . . . 72
5.3.2 Optical Profilometry . . . 74
5.4 Discussion . . . 78
5.4.1 Mechanical Testing . . . 78
5.4.1.1 AD730 vs. STAL15 ⟨001⟩ . . . 78
5.4.1.2 STAL15 ⟨001⟩ vs. STAL15 ⟨011⟩ . . . 79
5.4.1.3 Strain Rates of 10^{-3} s^{-1}, 10^{-2} s^{-1}, 10^{-1} s^{-1} . . . 80
5.4.1.4 Temperatures of 825 °C, 850 °C, 875 °C, 900 °C . . . 81
5.4.2 Optical Profilometry . . . 82
5.5 Conclusions . . . 84

6 Conclusions and Future Work **86**
6.1 Conclusions 86
6.2 Future Work 88
6.2.1 Exploration of the ⟨111⟩ Crystallographic Orientation 88
6.2.2 Interrupted Testing Around Yield Region 88
6.2.3 Optimizing Geometry for Anisotropy Analysis 89
6.2.4 Development of Accurate Models 89

Bibliography **91**

List of Figures

1.1 Yield stress variation of different single-crystal superalloys with respect to temperature [1]. 3
1.2 Deformation map for a polycrystalline superalloy illustrating the dependence on stress, temperature and strain rate [2]. 4

2.1 The atomic structure of the disordered γ phase (left) and the ordered γ' phase (right) [3]. 7
2.2 The two phase structure of a typical Ni-based single-crystal superalloy. The black filler part is γ and the lighter cuboidal parts are γ' [3]. . . 8
2.3 (Left) Section of the Ni-Cr-Al phase diagram. Points indicate compositions of the used alloys. (Right) The effect of temperature on yield stress, for various γ' compositions [4]. 10
2.4 Diagram illustrating the establishment of coherency strain in the presence of a lattice misfit between phases characterised by distinct lattice parameters (a and b) [5]. 11
2.5 The impact of temperature on the 0.2%, 1.0%, and 2.0% offset stresses of CTC-1 was established through compression tests conducted at a consistent strain rate of 10^{-4} s^{-1} [6]. 12
2.6 The alteration in yield stress as a function of temperature for the MarM200 alloy in single-crystal form (upper curve), and a monolithic Ni_3Al alloy which is made up of γ' particles with identical composition (lower curve). Testing orientation is $\langle 001 \rangle$ for both cases [7]. 13
2.7 Stress-strain curves obtained from compression tests for (a) single-phase γ and (b) single-phase γ' alloys [8]. 14
2.8 Selected alloy's tensile properties at various temperatures. (a) Yield strength and ultimate tensile strength. (b) Percentage elongation and percentage reduction of area after fracture. [9]. 14

2.9 Experimental alloy's microstructural evolution after tensile tests at various temperatures. (a) Room temperature, (b) 600 °C, (c) 760 °C, (d) 900 °C, (e) 1000 °C and (f) 1100 °C [9]. 16
2.10 Stress-strain curve of a single-crystal denoting different hardening stages [10]. 18
2.11 Tensile specimens with varying crystallographic orientations were subjected to different nominal strain rates: (a) 1.28×10^{-3}, (b) 1.28×10^{-2}, roughly (c) 10, and (d) 1000 s^{-1}. These specimens were colour-coded based on their initial crystallographic tensile axis, as shown in the Inverse Pole Figure (IPF) inset. The black dash-dotted line represents the average flow stress at 0.05 strain when the strain rate was 1.28×10^{-3} s^{-1}, facilitating a comparison of stress levels across the various scales [11]. 19
2.12 Tensile stress-strain curves are depicted with a logarithmic stress scale, covering a range of strain rates from 1.28×10^{-4} s^{-1} to roughly 1000 s^{-1}. The crystallographic orientations of the samples are situated close to the center of the IPF. Dotted lines represent repeated measurements for the same strain rate [11]. 20
2.13 Surface strain field predictions (ε_{xx} and ε_{xy}) and crystallographic rotations relative to initial orientations of three single-crystals after 50% elongation. Produced using CP-FE modelling [12]. 21
2.14 Cylindrical single-crystal samples impacted at high speeds [13]. 22
2.15 River patterns on a cleavage fracture surface [14]. 24
2.16 Ductile fracture of a tensile specimen. Notice the dimpled fracture surface [15]. 25
2.17 Fracture surface of cast titanium alloy after torsion (Magnification 1500x) [16]. 26
2.18 Fractured surfaces and longitudinal structures of tensile specimens at 1100 °C are shown for the following crystallographic orientations: (a, b) [100] specimen; (c, d) [120] specimen; (e, f) [110] specimen [17]. . . 27
2.19 The morphology of creep fractures in specimens oriented along [001], [011], and [111] directions is examined at various combinations of temperature and stress levels, specifically at: (b) 760 °C and 750 MPa, (c) 980 °C and 400 MPa, (d) 1100 °C and 200 MPa [18]. 28

3.1 The Instron TMF test bench with furnace and camera installed. . . . 31

3.2 3D model and drawing of the tensile test specimen. All dimensions are in mm. 32
3.3 Effect of temperature from room temperature to 300 °C. Sample orientation ⟨001⟩, strain rate 10^{-3} s^{-1}. 33
3.4 Effect of temperature from 600 °C to 725 °C. Sample orientation ⟨001⟩, strain rate 10^{-3} s^{-1}. 34
3.5 Effect of temperature from 725 °C to 800 °C. Sample orientation ⟨001⟩, strain rate 10^{-3} s^{-1}. 34
3.6 Effect of temperature from room temperature to 600 °C. Sample orientation ⟨011⟩, strain rate 10^{-3} s^{-1}. 35
3.7 Effect of temperature from 600 °C to 775 °C. Sample orientation ⟨011⟩, strain rate 10^{-3} s^{-1}. 36
3.8 Effect of temperature from 775 °C to 900 °C. Sample orientation ⟨011⟩, strain rate 10^{-3} s^{-1}. 36
3.9 Effect of strain rate from 10^{-3} s^{-1} to 10^{-1} s^{-1}. Sample orientation ⟨011⟩, temperature 825 °C. 37
3.10 Effect of strain rate from 10^{-3} s^{-1} to 10^{-1} s^{-1}. Sample orientation ⟨011⟩, temperature 850 °C. 38
3.11 Effect of strain rate from 10^{-3} s^{-1} to 10^{-1} s^{-1}. Sample orientation ⟨011⟩, temperature 875 °C. 38
3.12 Effect of strain rate from 10^{-3} s^{-1} to 10^{-1} s^{-1}. Sample orientation ⟨011⟩, temperature 900 °C. 39
3.13 0.2% offset yield comparison of ⟨001⟩ and ⟨011⟩ crystal orientations for different temperatures. 40
3.14 Elastic modulus comparison of ⟨001⟩ and ⟨011⟩ crystal orientations for different temperatures. 41
3.15 True stress-strain and hardening rate curves for STAL15 ⟨001⟩ at a strain rate of 10^{-3} s^{-1} and a temperature of 650 °C. The two vertical lines approximate where the linear hardening stage with a relatively high rate starts and ends, characteristic of stage II hardening [19]. . . 42
3.16 Stage II average hardening rates at a strain rate of 10^{-3} s^{-1} for temperatures from 600 °C to 800 °C. 43

4.1 Various stress-temperature curves showing different yield strength definitions for varying temperatures. Sample orientation ⟨001⟩, strain rate 10^{-3} s^{-1}. 48

4.2 Longitudinal structures (above) and fracture surfaces (below) of STAL15 ⟨001⟩ samples ruptured at different temperatures. 49
4.3 The effect of temperature on stress-strain graphs of STAL15 ⟨001⟩. Visual representations below show how the stress-strain curve transitions step by step. 50
4.4 Visual representations illustrating measurement of offset yield strengths of a material characterised by a flatter hardening curve versus a steeper one. It is noteworthy that while both materials undergo the transition from the elastic to plastic regions at the same points (proportional limit), employing higher offset yield definitions produces greater yield strength results. 51
4.5 Engineering stress vs engineering strain graphs of STAL15 ⟨001⟩ comparing the 0.2% and 0.01% offset yield strengths at various temperatures. 52
4.6 Fracture surface of STAL15 ⟨001⟩ at 650 °C. 53
4.7 Fracture surface of STAL15 ⟨001⟩ at 700 °C. 54
4.8 Fracture surface of STAL15 ⟨001⟩ at 725 °C. 55
4.9 Fracture surface of STAL15 ⟨001⟩ at 800 °C. 56

5.1 Diagram of the test bench and the orthogonal dual-camera configuration. 62
5.2 Digital extensometer setup and colour convention for the experiments. Arrows indicate the location and length of the extensometers. Notice the colours yellow and green are on the same location of the sample. This colour convention will be used to denote digital extensometer locations throughout the chapter. 63
5.3 True Stress vs. True Strain graph of AD730 at 675 °C. 65
5.4 True Stress vs. True Strain graph of STAL15 ⟨001⟩ at 675 °C. 66
5.5 True Stress vs. True Strain graph of STAL15 ⟨001⟩ at 825 °C. 68
5.6 True Stress vs. True Strain graph of STAL15 ⟨011⟩ at 825 °C. 68
5.7 True Stress vs. True Strain graph of STAL15 ⟨011⟩ at 10^{-2} s^{-1}. . . . 70
5.8 True Stress vs. True Strain graph of STAL15 ⟨011⟩ at 10^{-1} s^{-1}. . . . 71
5.9 True Stress vs. True Strain graph of STAL15 ⟨011⟩ at 850 °C. 72
5.10 True Stress vs. True Strain graph of STAL15 ⟨011⟩ at 875 °C. 73
5.11 True Stress vs. True Strain graph of STAL15 ⟨011⟩ at 900 °C. 73

5.12 3D fracture surfaces of STAL15 ⟨011⟩ samples, deformed in tension at various temperatures and strain rates. The images use a rainbow colour convention for height representation, as seen from the legend on the bottom-right corner of the figure. While the colour-coding scheme is uniform, the specific height range varies between images, with unique minimum and maximum values for each. Scale is the same for all images. 75
5.13 Aspect ratio vs. temperature (°C) graphs for varying strain rates. . . 76
5.14 Method of calculating the slope angles of the slip planes and how the angle is defined. Note that only the angles of the slip planes were calculated. The image on the left is an anaglyph stereogram and can be viewed in 3D using red-blue glasses. 77

List of Tables

3.1 Chemical composition of the STAL15 single-crystal superalloy. 30

5.1 Chemical composition of the AD730 polycrystalline superalloy [20]. . 61
5.2 Tensile test parameters. 64
5.3 Elastic moduli calculated from different regions of the AD730 and STAL15 ⟨001⟩ samples. Colour coding of camera numbers are as follows: 1= Red, 2= Orange, 3= Yellow, 4= Green, 5= Blue, 6= Purple. 66
5.4 Elastic moduli calculated from different regions of the STAL15 ⟨001⟩ and ⟨011⟩ samples. 69
5.5 Elastic moduli calculated from different regions of the STAL15 ⟨011⟩ samples at various strain rates. 71
5.6 Elastic moduli calculated from different regions of the STAL15 ⟨011⟩ samples at various temperatures. 74
5.7 Minimum and maximum slope angles of the fracture surface slip planes of STAL15 ⟨011⟩ samples at various temperatures and strain rates. . . 77

Chapter 1

Introduction

Working inside a gas stream having a temperature of approximately 1600 °C and being subjected to a force of approximately 18 tonnes per blade [21], high-pressure turbine blades are one of the most critical and technologically developed components in a gas turbine engine. The reason why high-pressure turbines are so critical for the gas turbine engine can be deducted from the thermal efficiency formula shown below:

$$\eta_{th} = \frac{W}{Q} = 1 - \frac{T_2}{T_1}$$

where W is the work output, Q is the heat input, and T_1 and T_2 are the entry and exit temperatures, respectively. This formula demonstrates that to increase the thermal efficiency, either the turbine entry temperature (TET or T_1) must be increased- or the exit temperature (T_2) be decreased. From an engineering perspective, the sensible option would be to increase the TET, as it is much simpler to accomplish than the latter [1]. The main disadvantage of increasing the TET is that as it is increased, finding suitable materials which can perform well at the resultant high temperature and stresses becomes very difficult.

This is where a very unique material, the Ni-based single-crystal superalloy, comes into play. With its ability to withstand high amounts of stresses at high temperatures,

Ni-based single crystal superalloys have been used in the aerospace sector for more than four decades, and has recently started being used in the energy generation sector. What makes this superalloy appealing for these applications is its ability to preserve its yield strength at very high temperatures -as a matter of fact not just preserve it, but increase it; as seen in Figure 1.1.

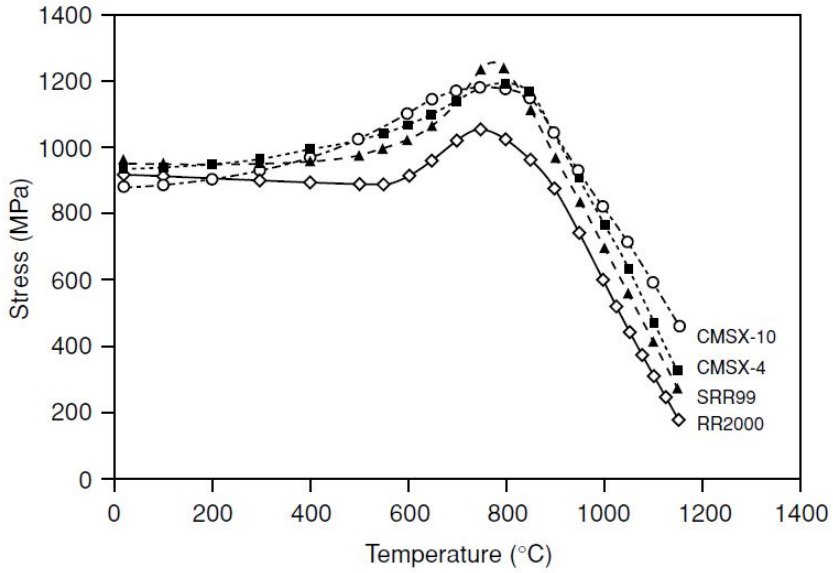

Figure 1.1: Yield stress variation of different single-crystal superalloys with respect to temperature [1].

The unusual way this material reacts to deformation at high temperatures is caused by what is defined as the yield strength anomaly (also called the anomalous yield), and it primarily comes from its unique two-phase ($\gamma + \gamma'$) microstructure [3]. With increasing temperature, different deformation mechanisms occur; as seen in Figure 1.2. From the figure we can see that at temperatures up to 400 °C, the γ' precipitates are sheared by paired dislocations creating an antiphase boundary (APB) defect; or else can bypass them using the Orowan looping mechanism [22, 23]. At temperatures above 800 °C, the controlling deformation mechanism is thermally activated dislocation climb [24, 25]. The 400-800 °C region is not as clearly defined as the aforementioned regions; depending on the strain rate, deformation mechanisms

such as microtwinning, continuous faults, or APB shearing might occur [26]. As a time-dependent mechanism, microtwinning in turbine discs used in aircraft engines have previously been reported as an important deformation mechanism [27, 28].

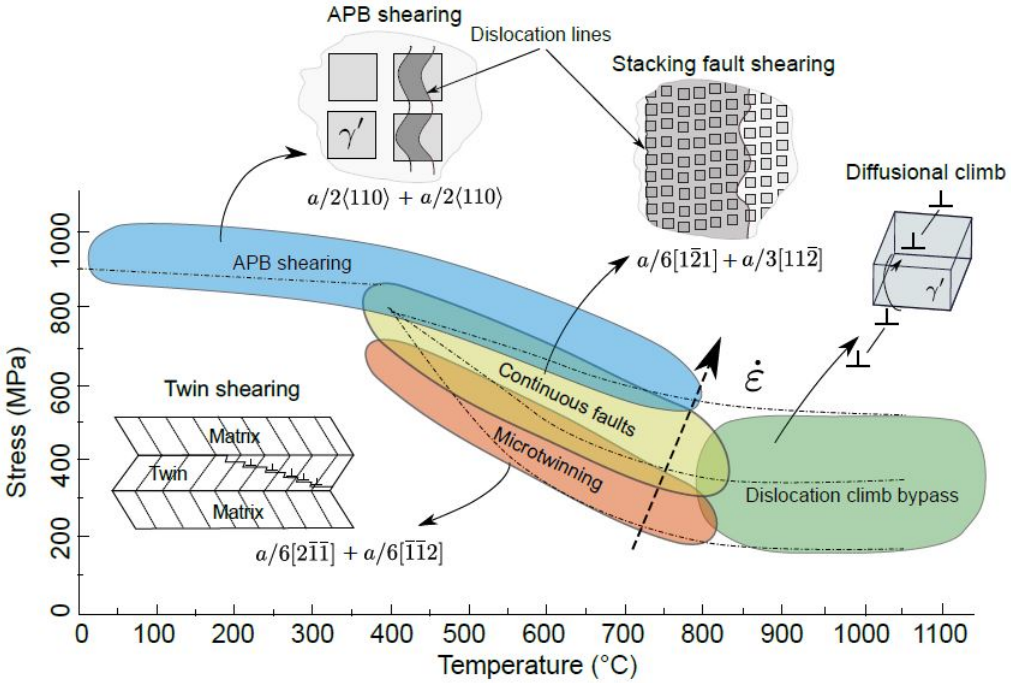

Figure 1.2: Deformation map for a polycrystalline superalloy illustrating the dependence on stress, temperature and strain rate [2].

The thesis has been arranged as follows:

- In Chapter 2, a literature review giving the necessary background information in order to understand the following chapters will be presented.

- Chapter 3 makes a comparative analysis of the mechanical properties of STAL15 $\langle 001\rangle$ and $\langle 011\rangle$ crystallographic orientations. Effect of temperature and strain rate on the $\langle 001\rangle$ and $\langle 011\rangle$ are investigated to get a better understanding of how these orientations differ in terms of mechanical properties.

- In Chapter 4 we go into detail on the anomalous yield phenomena, and see if anomalous yield is dependent on how yield strength is defined. The experiments

nearing the 0.2% anomalous yield peak point were done with a temperature difference of 25 °C, a sort of detail never done before. Fracture surfaces are analysed using SEM for further understanding.

- Chapter 5 provides a solution to measurement difficulties of anisotropic single-crystal materials. Instead of using a single digital video extensometer, we develop an orthogonal dual-camera, multi-extensometer configuration to compare mechanical results taken from the same sample. The results interestingly show how a single digital extensometer result produces unrepeatability, and multiple digital extensometers are a must in order to confidently understand the mechanical properties of anisotropic materials.

Chapter 2

Literature Review

2.1 Nickel-Based Superalloys

A superalloy can be defined as an alloy possessing the capability to function efficiently at temperatures close to its melting point [29]. Primarily composed of nickel as its base element, superalloys are amalgamations of various elements such as aluminum, titanium, chromium, cobalt, tungsten, molybdenum, and many more. Since their inception in the 1950s, they have found extensive use in technologically critical components that demand resistance to high temperatures, mechanical stress, and chemical degradation. These applications span from aerospace engines to gas turbines employed in power generation.

When compared to conventional alloys, superalloys demonstrate exceptional resistance to static, fatigue, and creep loading under elevated temperatures, particularly when operating above 800 °C [30]. This thermal stability and mechanical resilience make them indispensable in scenarios necessitating prolonged exposure to extreme conditions.

2.1.1 Physical Metallurgy of Superalloys

The distinctive properties exhibited by nickel-based superalloys primarily stem from their two-phase microstructure, composed of γ and γ' phases (see Figure 2.1). Depending on the specific categorisation of the superalloy—whether it is single crystal or polycrystalline—different phases such as borides, carbides or others may precipitate within the γ grain boundaries [1]. To provide a detailed overview, a summary of the various phases along with their respective compositions is presented below.

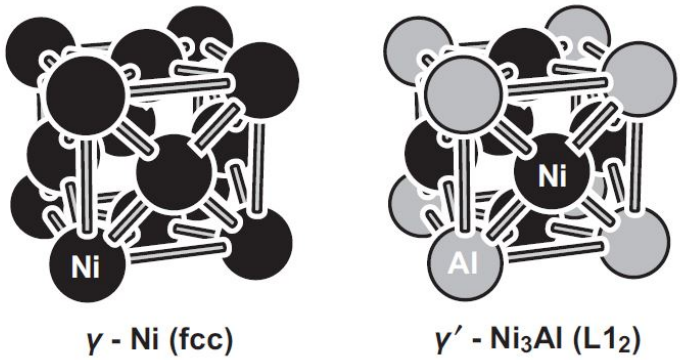

Figure 2.1: The atomic structure of the disordered γ phase (left) and the ordered γ' phase (right) [3].

2.1.1.1 The γ phase

The γ phase functions as a continuous matrix accommodating all other phases within it. Exhibiting a face-centered cubic (FCC) crystal structure, this phase contains substantial quantities of elements like Cr, Co, Mo, W, Ru, and Re, among others. These elements contribute to fortifying the γ matrix by impeding dislocation motion through solid solution strengthening [31, 32, 33]. Co also plays a role in diminishing the stacking-fault energy, being particularly influential in this aspect [34, 35]. Decreasing the stacking-fault energy results in augmented spacing between partial dislocations, consequently rendering dislocation movement more challenging and elevating the material's high-temperature performance [36], and also increases the strength and tensile ductility of the material [35].

2.1.1.2 The γ' phase

The γ' phase serves as a strengthening component, residing within the γ matrix. It exhibits an ordered $L1_2$ crystal structure, with Al atoms at the cube corners and Ni atoms at face centers, as seen previously in Figure 2.1. The predominant variant of γ' is the Ni_3Al precipitate; however, the addition of elements such as Ti, Ta, and Nb can lead to the formation of distinct phases such as Ni_3Ti, Ni_3Ta and Ni_3Nb, contingent upon the specific alloy composition [37]. A micrograph illustrating the dispersion of γ' particles within the γ matrix is provided in Figure 2.2.

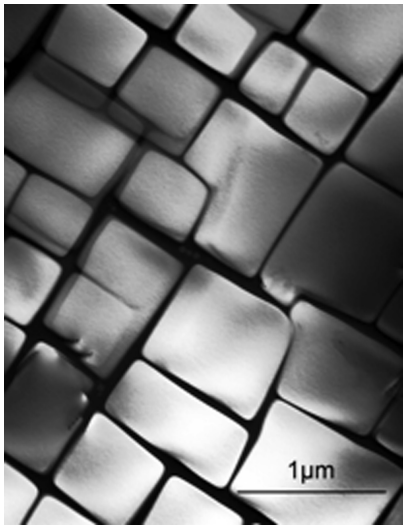

Figure 2.2: The two phase structure of a typical Ni-based single-crystal superalloy. The black filler part is γ and the lighter cuboidal parts are γ' [3].

2.1.1.3 Carbides and Borides

Incorporating concentrations of up to 0.2 wt%, carbon engages with metallic elements like Ti, Ta, or Hf to give rise to MC carbides. Over extended service durations, these compounds can degrade into distinct species such as $M_{23}C_6$ and M_6C, with a tendency to accumulate along the boundaries of the γ grains. Additionally, boron forms compounds by bonding with elements such as Cr or Mo, resulting in the creation of borides that occupy the γ grain boundaries [3].

2.1.1.4 Other Phases

Certain superalloys, especially those that have undergone prolonged service, may exhibit the presence of several additional phases. Among these, topologically close-packed (TCP) phases like Laves, μ, and σ are noteworthy examples [38]. Elevated concentrations of elements such as Cr, Mo, W, and Re encourage the formation of these TCP phases [39].

2.2 Strengthening Mechanisms in Ni-Based Single-Crystal Superalloys

The immense high temperature yield strength of the Ni-based single-crystal superalloy exists mainly because of the γ' phase, which by multiple mechanisms increases the yield strength by a factor of 5, when compared with the precipitate free γ phase [40]. While coherent precipitation significantly contributes to achieving this high strength by increasing internal stress within the matrix [41], it's worth noting that solid solution strengthening of the γ matrix also plays a vital role [5]. Each strengthening mechanism emerges from interactions of different, more fundamental physical effects-which makes it difficult to give a general description.

The γ' precipitate size, composition and morphology all affect the resulting alloy strength. In addition to this, as illustrated by Beardmore in Figure 2.3, the $\gamma'/(\gamma+\gamma')$ fraction also influences the yield strength of the Ni-based single-crystal material [4].

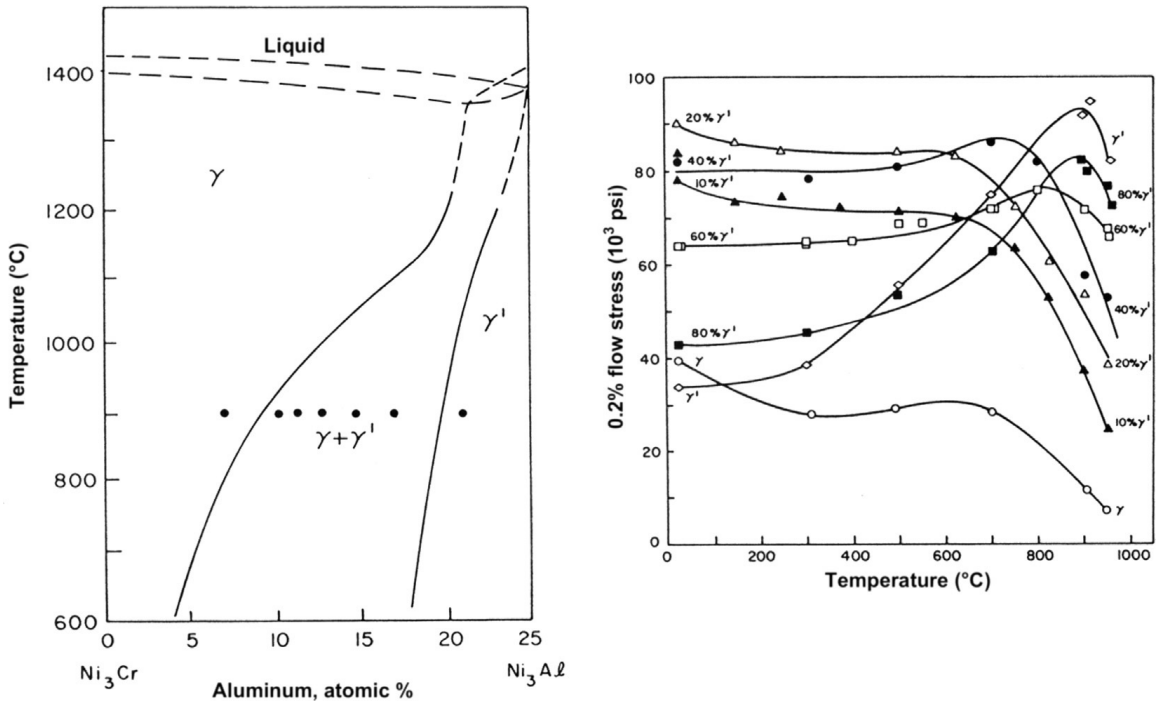

Figure 2.3: (Left) Section of the Ni-Cr-Al phase diagram. Points indicate compositions of the used alloys. (Right) The effect of temperature on yield stress, for various γ' compositions [4].

According to Ardell [42], the strengthening of superalloys through precipitation originates from the following mechanisms; stacking fault strengthening, modulus strengthening, chemical strengthening, order strengthening and coherency strengthening.

Stacking fault strengthening and modulus strengthening result from variations in stacking fault energies and elastic moduli between the matrix and precipitate phases, respectively [5]. In the former case, distinct stacking fault energies in the matrix and precipitate phases lead to varying distances between partial dislocations, impeding dislocation movement. In the latter case, the differing elastic moduli across phases induce changes in dislocation energy, hence impacting dislocation motion [42].

Chemical strengthening results from dislocations shearing the precipitate, forming a new interface with higher surface energy. Order strengthening arises when dislocations traverse precipitates with ordered crystal structures, creating an anti-phase

boundary (APB) during the process. Coherency strengthening occurs when the matrix and precipitate phase possess different lattice parameters, generating a strain field between them, as seen in Figure 2.4 [5].

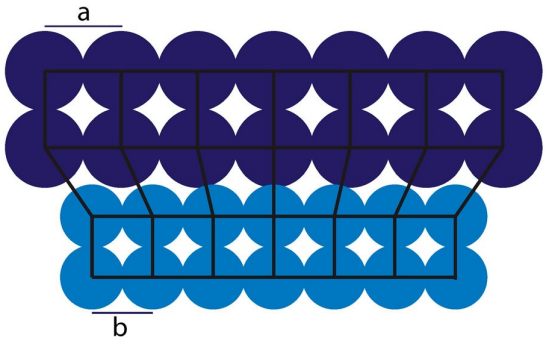

Figure 2.4: Diagram illustrating the establishment of coherency strain in the presence of a lattice misfit between phases characterised by distinct lattice parameters (a and b) [5].

While these mechanisms can simultaneously operate, their relative significance depends on the specific alloy system, leading to differences of opinion in the literature. For instance, Ardell [42] emphasises order strengthening, while Ahmadi [43] highlights coherency strain and APBs as primary yield-strength mechanisms. Kozar [44] argues that APB's and the tertiary γ' volume fraction are key for understanding the yield strength increase. Some research offers middle-ground perspectives on these differing opinions [45, 46, 47, 48].

There's also divergence in viewpoints regarding coherency strengthening. While researchers such as Gerold and Haberkorn [49], Decker and Mihalisin [50], and Miller and Ansell [51] argue that this is a major strengthening mechanism, Raynor and Silcock [52] describe it as insignificant.

2.3 The Yield Strength Anomaly

In contrast to the majority of other alloys, Ni-based single-crystal superalloys possess a distinctive characteristic; as the temperature is raised from room temperature to around 800 °C, an increase in their yield stress takes place (see Figure 2.5) [1, 6, 53]. However, after a certain point the yield stress rapidly decreases, as shown previously in Figure 1.1). This is not the case for pure Ni- nor any other constituent of these superalloys when they are pure; hence we can say the main reason for this effect has to do with the mechanical properties of the ordered $L1_2$, or, the γ' phase.

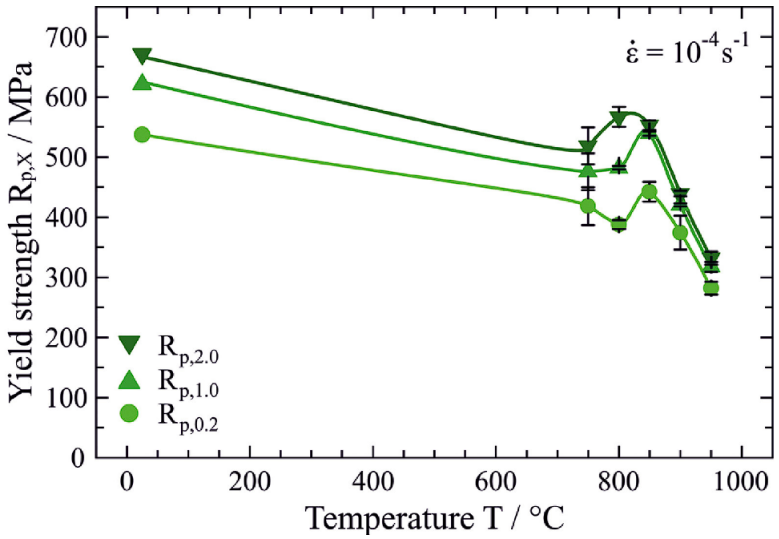

Figure 2.5: The impact of temperature on the 0.2%, 1.0%, and 2.0% offset stresses of CTC-1 was established through compression tests conducted at a consistent strain rate of 10^{-4} s^{-1} [6].

To provide evidence for this phenomenon, Piearcey et al. [7] conducted an experiment involving tensile tests on both the ⟨001⟩ oriented MarM200 single-crystal superalloy and another alloy sharing the same γ' phase composition (see Figure 2.6). Upon comparing the stress-strain curves of these two materials, it becomes evident that the γ' phase conveys a higher proportion of strength as temperature increases. Furthermore, observations indicate that beyond 800 °C, there is minimal disparity between the flow stress curves of the two-phase (γ+γ') and the single-phase (γ') alloys.

This suggests that at elevated temperatures, the mechanical properties are primarily governed by the (γ') phase.

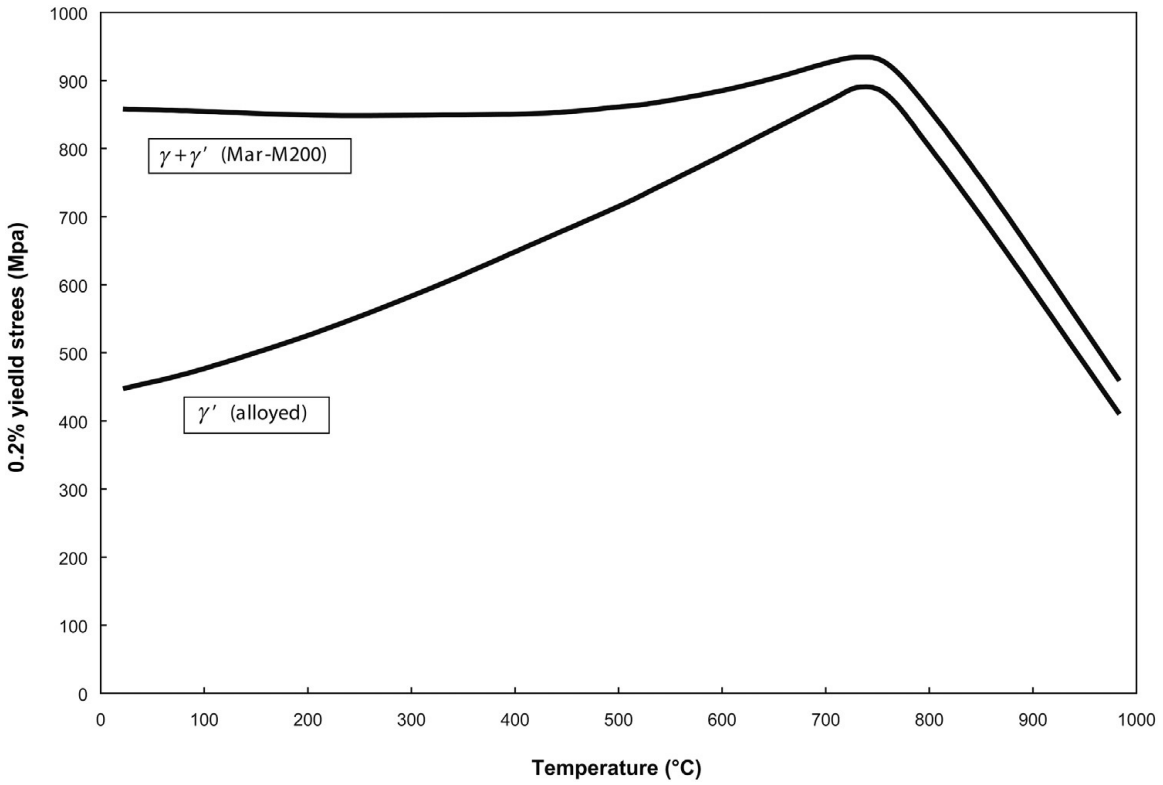

Figure 2.6: The alteration in yield stress as a function of temperature for the MarM200 alloy in single-crystal form (upper curve), and a monolithic Ni_3Al alloy which is made up of γ' particles with identical composition (lower curve). Testing orientation is $\langle 001 \rangle$ for both cases [7].

The study conducted by Wu et al. [8] on single-phase γ and γ' alloys is also of significance. As depicted in Figure 2.7, stress-strain curves for single-phase γ and γ' alloys are presented across an extensive temperature spectrum. Notably, the yield strength of the single-phase γ alloy exhibited a decline as temperature rose, as shown in Figure 2.7a. In contrast, for the single-phase γ' alloy, the flow strength demonstrated an increase, followed by a sharp decrease, as illustrated in Figure 2.7b. Within the temperature range of 650 °C to 760 °C, the single-phase γ' alloy demonstrates strength that is tenfold higher in comparison to the former alloy composition. These findings underscore the complex interplay between temperature, alloy composition,

and mechanical behaviour in single-phase γ and γ' alloys, emphasising the need for comprehensive investigations into their performance characteristics.

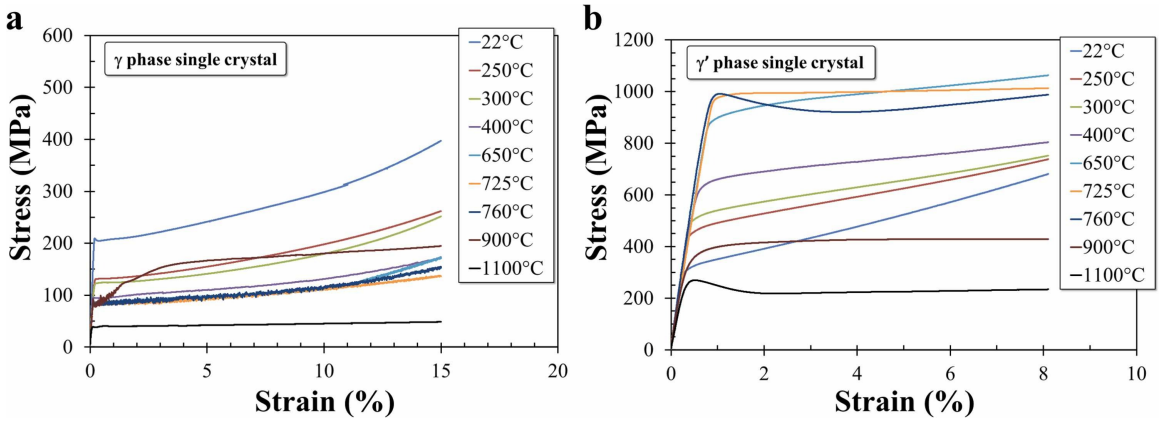

Figure 2.7: Stress-strain curves obtained from compression tests for (a) single-phase γ and (b) single-phase γ' alloys [8].

Wang et al. [9] employed transmission electron microscopy to analyse the microstructural changes in an experimental single-crystal superalloy subjected to tensile testing at different temperatures. The graphs depicting yield strength and ultimate tensile strength (Figure 2.8a) as well as percentage elongation and percentage reduction of area (Figure 2.8b) for these temperatures have been provided below.

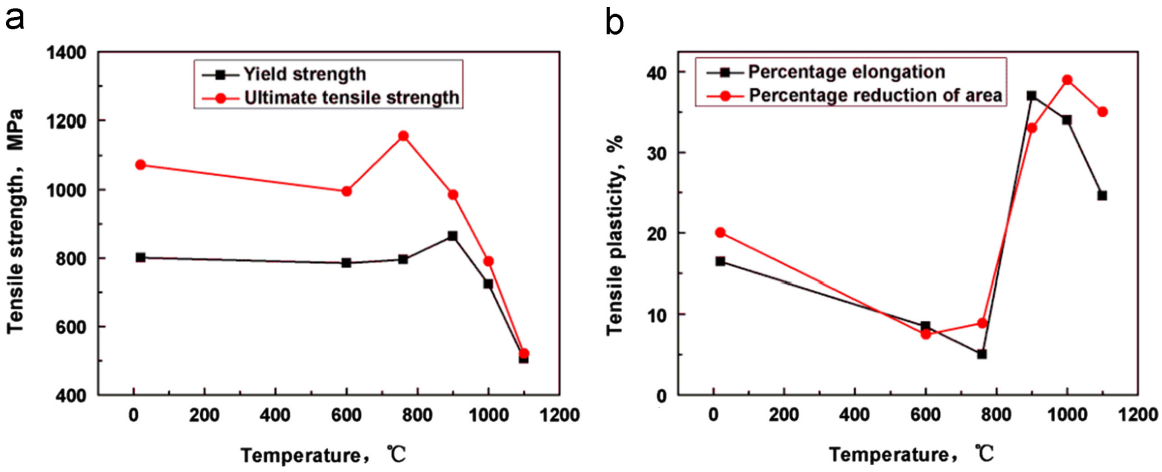

Figure 2.8: Selected alloy's tensile properties at various temperatures. (a) Yield strength and ultimate tensile strength. (b) Percentage elongation and percentage reduction of area after fracture. [9].

Investigation into deformation mechanisms under mentioned temperatures have revealed the following insights (see Figure 2.9): during tensile testing at room temperature, 600 °C, and 760 °C, the presence of stacking faults within the γ matrix has been detected. These stacking faults induce step-like stress jumps in the stress-strain curves. Working in conjunction with $a/6$ $\langle 112 \rangle$ Shockley dislocations, they display notable resistance to dislocation slipping. Consequently, they play a substantial role in work hardening. Secondly, at elevated temperatures of 1000 °C and 1100 °C, an examination of interfacial dislocation networks indicates decreased resistance to slip dislocations. This phenomenon is attributed to the higher temperature and associated flow stress. Lastly, the dislocation behaviour within γ' precipitates shows temperature-dependent variation. Below 900 °C, $a/3$ $\langle 121 \rangle$ type dislocations are involved in shearing. Beyond 900 °C, the behaviour shifts to APB-coupled $a/2$ $\langle 110 \rangle$ type dislocations, which intersect in diverse shapes [9].

In the context of creep tests, we see that at low temperatures pairs of dislocations can shear the γ' precipitates, creating an antiphase boundary (APB), or else bypass them by the Orowan looping mechanism if the γ' fraction is low enough [22, 23]. At high temperatures, climb-assisted glide around γ' precipitates is found to be the main deformation mechanism [25, 24]. The mid-temperature range is not as clear as the aforementioned regions- where, depending on the strain rate, deformation mechanisms such as microtwinning, continuous faults, or APB shearing can occur [26].

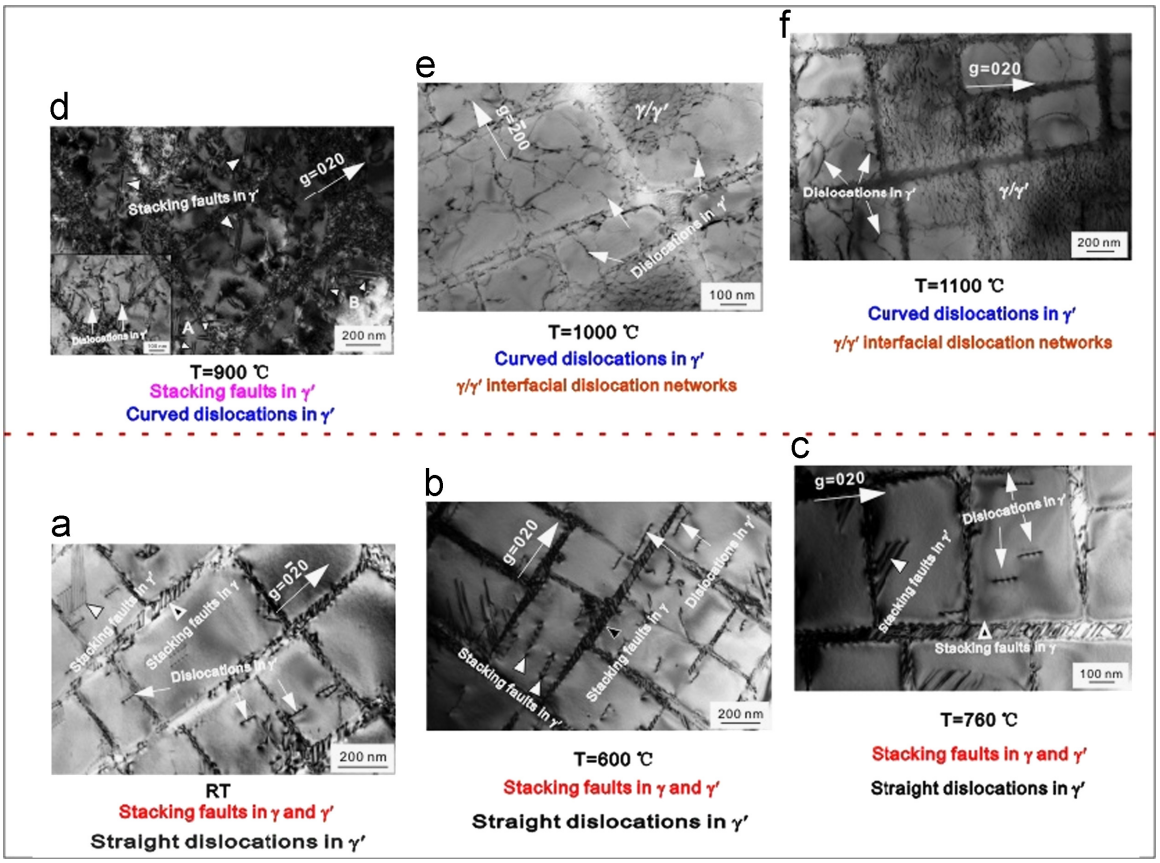

Figure 2.9: Experimental alloy's microstructural evolution after tensile tests at various temperatures. (a) Room temperature, (b) 600 °C, (c) 760 °C, (d) 900 °C, (e) 1000 °C and (f) 1100 °C [9].

The following can also be said about the principle features of yield anomaly in Ni-based single-crystal superalloys:

Orientation-Dependent Yield Maxima: The highest yield point strongly relies on the orientation of the sample. Furthermore, the rate of hardening mechanisms is remarkably swift and reaches its peak at temperatures coinciding with the occurrence of the anomalous yield phenomenon [54, 55, 56, 57].

Alloy Variability: It cannot be said that all single-crystal superalloys experience anomalous yield [58, 53].

Temperature-Dependent Slip Systems: At temperatures that are below the peak of the yield strength maxima (area where yield strength starts increasing with temperature), the main slip system is $\langle 001 \rangle \{111\}$. Beyond the peak, it predominantly

becomes $\langle 001 \rangle \{010\}$ [59].

Temperature-Dependent Yield Stress: In most cases, the yield stress begins increasing starting from room temperature. Of course there are exceptions to this with materials such as Ni_3Ge [60] and Ni_3(Si, Ti) [61], where the yield stress begins increasing starting from temperatures as low as 77 K.

2.4 Tensile Testing of Ni-based Single-Crystal Superalloys

When analysing the stress-strain behaviours of Ni-based single-crystal superalloys, we generally see three distinct hardening stages [62]. In the initial stage I, referred to as "easy glide", the strain hardening rate remains low, and a primary slip system dominates the deformation. The subsequent stage II marks the increasing activation of secondary slip systems, leading to the interaction between primary and secondary dislocations, which results in a higher and relatively constant hardening rate. Lastly, stage III encompasses a declining hardening rate and a plateauing flow stress due to the dynamic annihilation of dislocations through cross-slip. Figure 2.10 shows these hardening stages in detail.

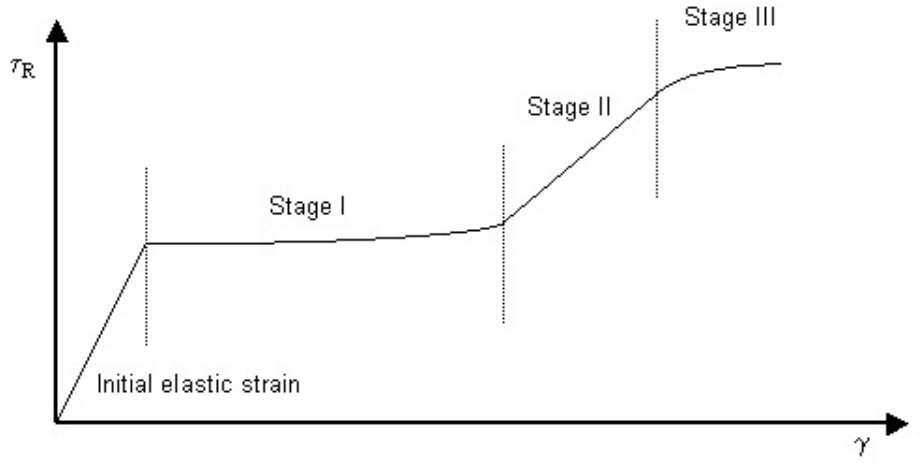

Figure 2.10: Stress-strain curve of a single-crystal denoting different hardening stages [10].

Croteau et al. [11] conducted tensile experiments on single-crystal niobium samples, each possessing different crystallographic orientations. The specimens deformed at the lowest strain rate of 1.28×10^{-3} s^{-1}, consistently exhibit the three hardening stages (see Figure 2.11a). At a slightly higher strain rate of 1.28×10^{-2} s^{-1} (see Figure 2.11b), most tensile orientations display a qualitatively similar three-stage hardening behaviour observed at the lower rate. These results are aligned with findings by Gnäupel-Herold et al. [63], who observed analogous three-stage behaviour in their tensile tests conducted at strain rates of 10^{-4} s^{-1} or lower. At higher strain rates such as 10^{-1} s^{-1} and 10 s^{-1}, the distinct manifestations of both stage I and stage II hardening fade away (see Figure 2.11c). This phenomenon can also be seen from the tests done at various strain rates, for the same orientation (see Figure 2.12). Mitchell et al. [64] have also noted the disappearance of stage I in their research.

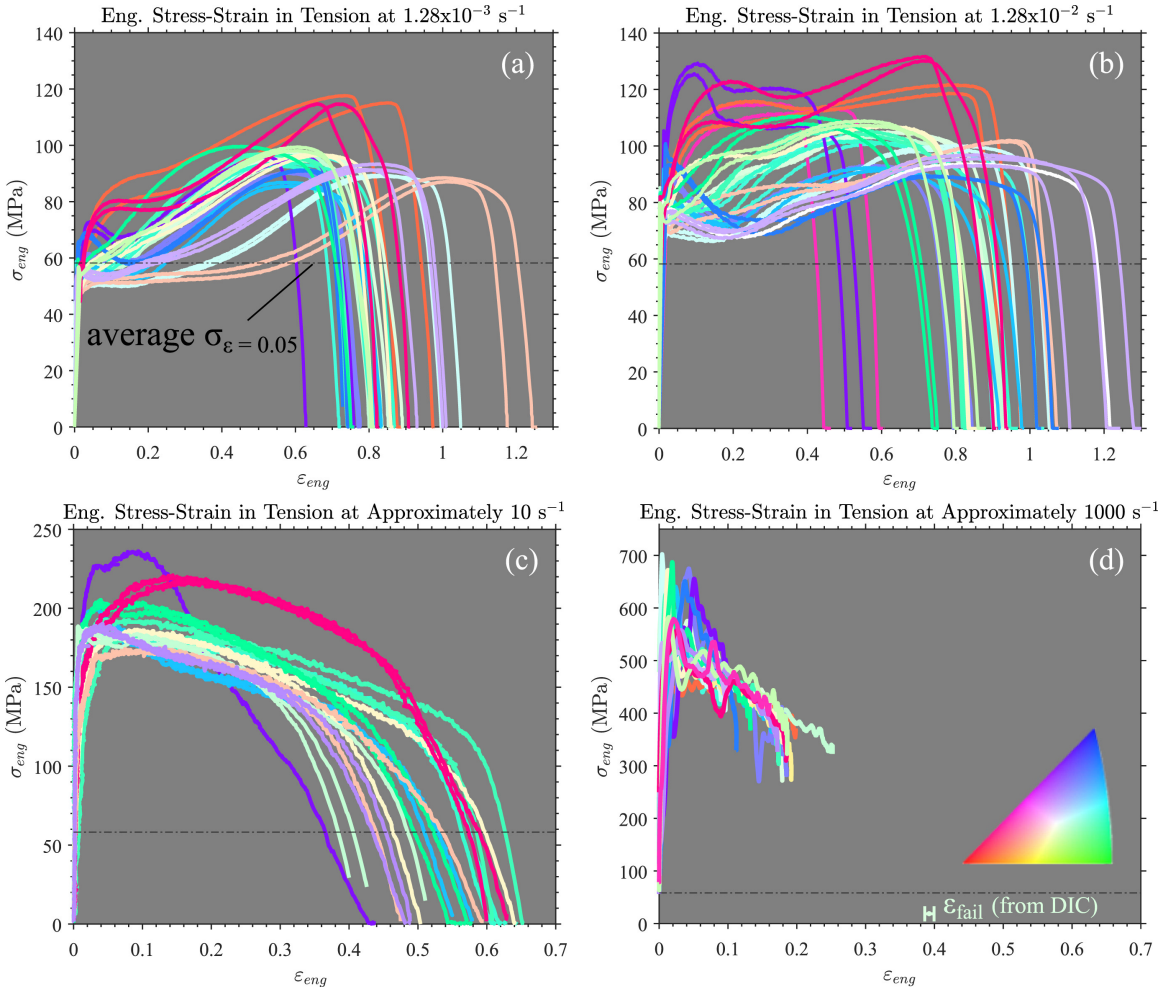

Figure 2.11: Tensile specimens with varying crystallographic orientations were subjected to different nominal strain rates: (a) 1.28×10^{-3}, (b) 1.28×10^{-2}, roughly (c) 10, and (d) 1000 s^{-1}. These specimens were colour-coded based on their initial crystallographic tensile axis, as shown in the Inverse Pole Figure (IPF) inset. The black dash-dotted line represents the average flow stress at 0.05 strain when the strain rate was 1.28×10^{-3} s^{-1}, facilitating a comparison of stress levels across the various scales [11].

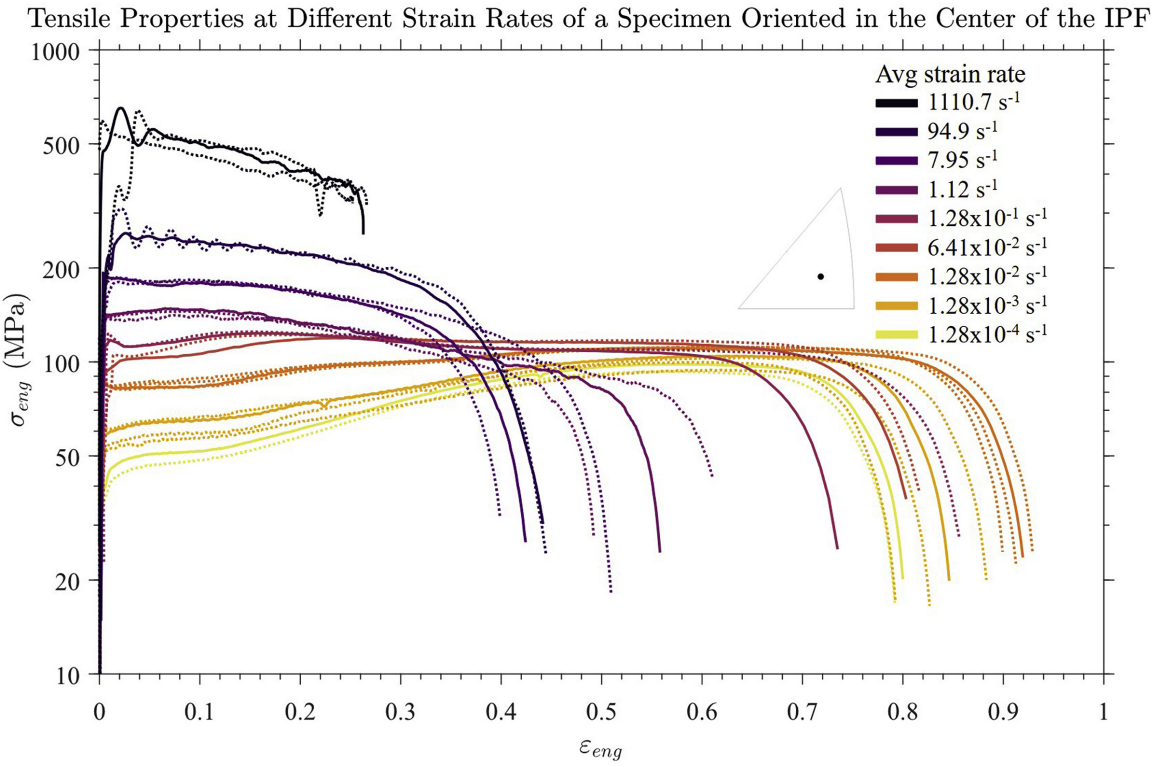

Figure 2.12: Tensile stress-strain curves are depicted with a logarithmic stress scale, covering a range of strain rates from 1.28×10^{-4} s^{-1} to roughly 1000 s^{-1}. The crystallographic orientations of the samples are situated close to the center of the IPF. Dotted lines represent repeated measurements for the same strain rate [11].

Tensile tests conducted by Yeh et al. [65] at temperatures of 900 °C and 1100 °C clarify the substantial solid solution strengthening achieved through additions of both Re and Ru. Intriguingly, despite a lower atomic percentage content, Re additives show a superior strengthening effect compared to Ru additives. Furthermore, the incorporation of Re and Ru into the experimental alloys leads to a discernible reduction in the volume fraction of γ' precipitates. Notably, flow stresses attributed to the γ' phase exhibit a remarkable three to fivefold elevation relative to the γ phase at both 900 °C and 1100 °C. Ru additions demonstrate a dual strengthening effect, influencing both the γ and γ' phases. This is evident in the significant augmentation of flow stresses in the single-phase γ alloy accompanied by a modest yet discernible increase in the flow stress of the single-phase γ' alloy [65].

2.5 Strain Localisation in Anisotropic Materials

Strain localisation, a phenomenon where plastic deformation concentrates in localised regions of a material, plays a pivotal role in shaping the mechanical behaviour of materials. Lim et al. [12] investigated crystallographic orientation-dependent strain localisation in body-centered cubic (BCC) tantalum single crystals with tensile axes oriented close to [100], [110], and [111] directions. Under quasi-static, uniaxial tension, distinct deformation behaviours were observed: strong strain localisation and shear banding in [100] specimens, limited rotation and pronounced necking in [110] specimens, and significant crystal rotations associated with shear-dominated behaviour in [111] single crystals. Crystal plasticity (CP) simulations were also done for these orientations, as seen in Figure 2.13. Void presence was noted in fracture surfaces of [100] and [111] specimens, while the [110] specimen exhibited void-free behaviour, highlighting the role of dislocation boundaries in void nucleation [12].

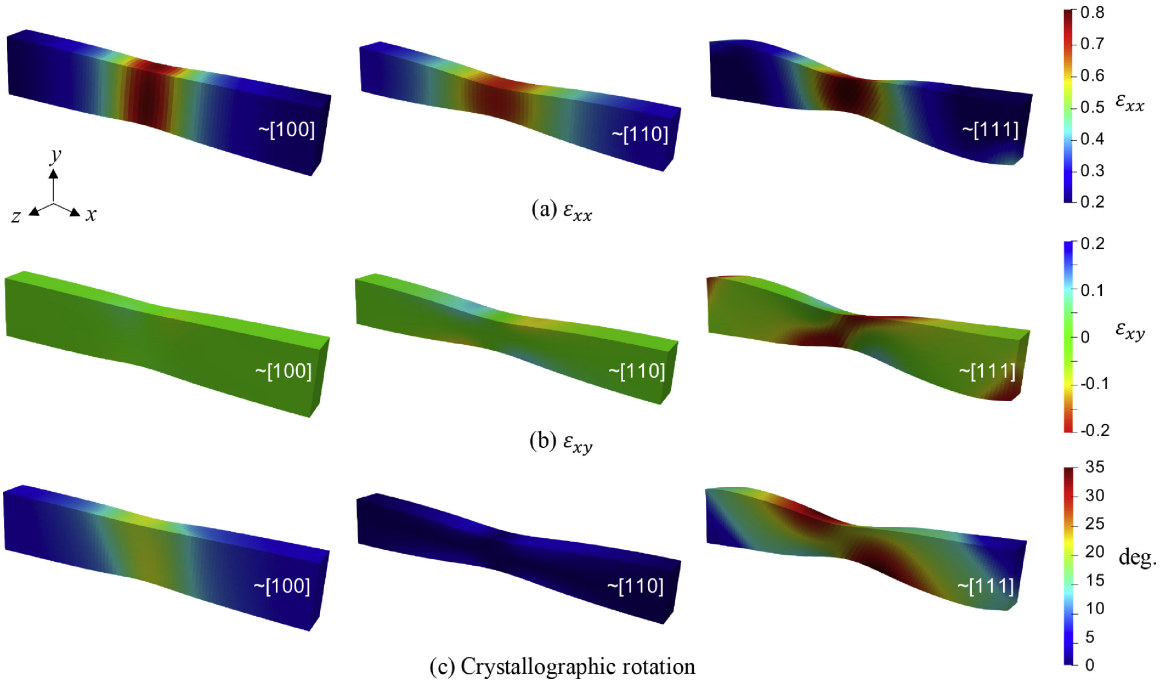

Figure 2.13: Surface strain field predictions (ε_{xx} and ε_{xy}) and crystallographic rotations relative to initial orientations of three single-crystals after 50% elongation. Produced using CP-FE modelling [12].

In a complementary study by Carroll et al. [13], the focus shifted to the investigation of high-rate deformation in Ta single-crystals. Examining primary crystal orientations of ⟨001⟩, ⟨011⟩, and ⟨111⟩, the researchers observed a notable and symmetrical localisation phenomenon, as illustrated in Figure 2.14. Distinct behaviour emerged across orientations, characterised by differing counts of symmetry planes: ⟨001⟩ displayed four symmetry planes, ⟨011⟩ displayed two, and ⟨111⟩ displayed three. These findings clarify the complex interplay between crystal orientation and strain localisation, shedding light on the mechanics governing the high-rate deformation of BCC Ta single-crystals.

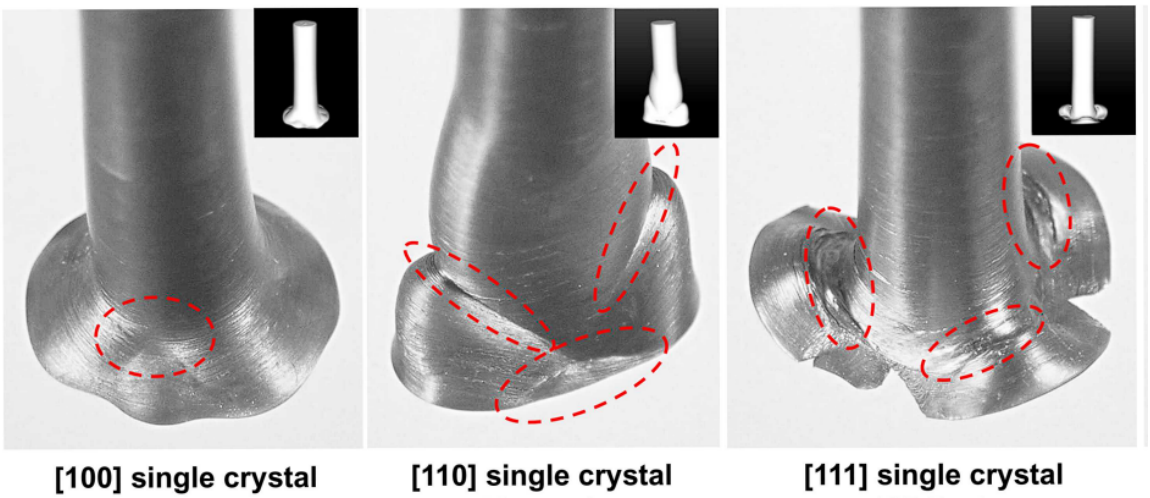

Figure 2.14: Cylindrical single-crystal samples impacted at high speeds [13].

2.6 Fractography Analysis of Ni-based Superalloys

The advancement of techniques like scanning electron microscopy (SEM) and transmission electron microscopy (TEM) has significantly enhanced our comprehension of fracture mechanisms, which has proven to be of immense value in failure analysis and the development of improved materials [66]. The significance of fractography arises from its capacity to shed light on the root causes and mechanics of fractures [67]. In addition to the conventional qualitative approach, the utilisation of quantitative

fractography aims to quantitatively assess topographic attributes of fracture surfaces. This reveals essential characteristics such as true surface areas, distances, sizes, quantities, morphologies, orientations and positions, as well as statistical distributions of these parameters [68].

Identifying a fracture mode involves a morphological investigation process that retraces the fracture's history to reveal its initiation, development, and culmination. Fractographic analysis, utilising both optical and scanning electron microscopy, emerges as a methodology that contributes to unraveling the complexities of fracture analysis and problem-solving [67].

2.6.1 Fracture Mechanisms

Within the realm of various damage mechanisms, our focus narrows to those associated with brittle and ductile fractures in metallic alloys. Brittle fractures are characterised by cleavage planes, while ductile fractures involve dimpled surfaces. Cleavage fracture exhibits a preference for dense atomic planes. In maintaining equilibrium along the crack front, adjacent steps convene to create a single elevated step, leading to the formation of distinctive "rivers", as depicted in Figure 2.15 [69]. These river patterns align with the local propagation direction of cleavage cracks. Macroscopically, the surfaces of cleavage facets tend to align with the maximum principal stress direction, characteristic of mode I fracture. The formation mechanism of river patterns is rooted in the transition from mode I to an increasingly prevalent mode III fracture component [70]. Under electron microscopy, fracture surfaces rarely manifest exclusively as dimpled rupture or cleavage. The prevalence of these modes is contingent upon the specific metal and its attributes, with areas of both fracture types often coexisting, even if one predominates [71]. The term "quasi-cleavage" denotes a fracture pattern that combines the qualities of both cleavage fractures and dimpled ruptures or tear ridges. This term characterises a small-scale fractured surface

that typically emerges from conditions such as (a) abrupt or impactful loads, (b) colder temperatures, (c) elevated degrees of restriction at ambient temperatures, or (d) within extensively cold-worked components at ambient temperature. The more favoured expression is "cleavage with ductile tear ridges" [71].

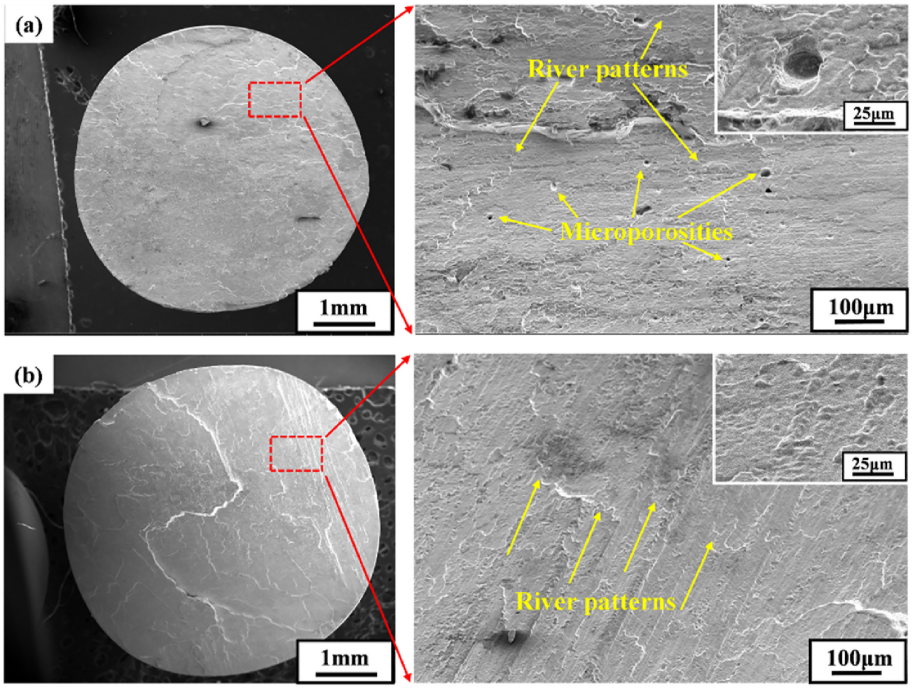

Figure 2.15: River patterns on a cleavage fracture surface [14].

The process of microvoid coalescence aids the development of larger cracks, exhibiting minute cup-shaped features known as "dimples". In ductile metals, the actual fracture surface comprises an assembly of these dimples or halfvoids, a feature discernible primarily through electron microscopy. This distinct surface is termed a dimpled-rupture fracture surface, exemplified in Figure 2.16. Analysing these dimples proves valuable in the study of fractures, as they bear a high sensitivity to the directional influence of the stresses that create them [71].

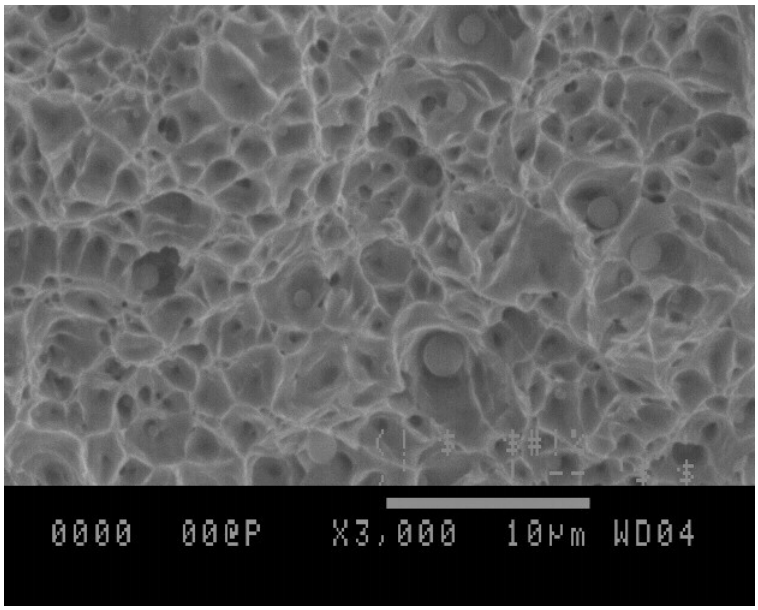

Figure 2.16: Ductile fracture of a tensile specimen. Notice the dimpled fracture surface [15].

Tensile loads that are evenly distributed across the transverse section will result in the formation of equiaxial dimples, while lateral or tangential loads produce dimples with a parabolic shape [72]. Consequently, in cases of shear failure induced by tensile or thermal shear bands, the fracture surface displays characteristic parabolic dimples (see Figure 2.17).

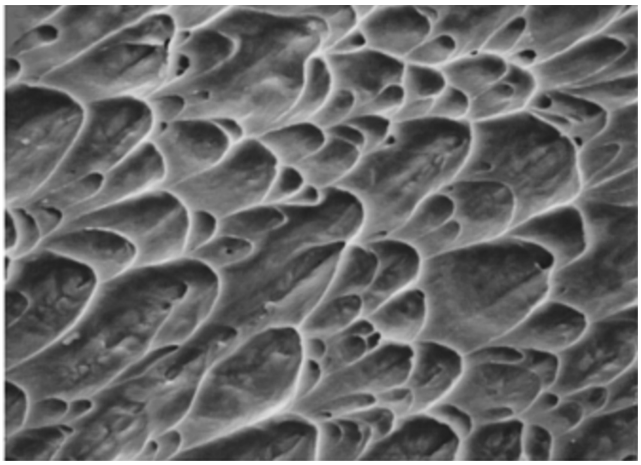

Figure 2.17: Fracture surface of cast titanium alloy after torsion (Magnification 1500x) [16].

2.6.2 Effect of Temperature and Crystallographic Orientation on Fracture Characteristics

The mechanical behaviour of Ni-based single-crystal superalloys is notably influenced by crystallographic orientation and temperature. Yang et al. [17] emphasise that tensile testing of single-crystal specimens oriented along the [100], [120], and [110] directions yields distinct fracture surface characteristics. At 760 °C, [100], [120], and [110] specimens exhibit quasi-cleavage features on their fracture surfaces. Shifting to 980 °C, all orientations showcase a combination of quasi-cleavage and dimple characteristics on their fracture surfaces. At the elevated temperature of 1100 °C, [100] and [120] specimens reveal dimple features, while [110] specimens present a fusion of quasi-cleavage and dimple attributes [17]. SEM images of the fracture surface and longitudinal structure of the 1100 °C sample are shown in Figure 2.18.

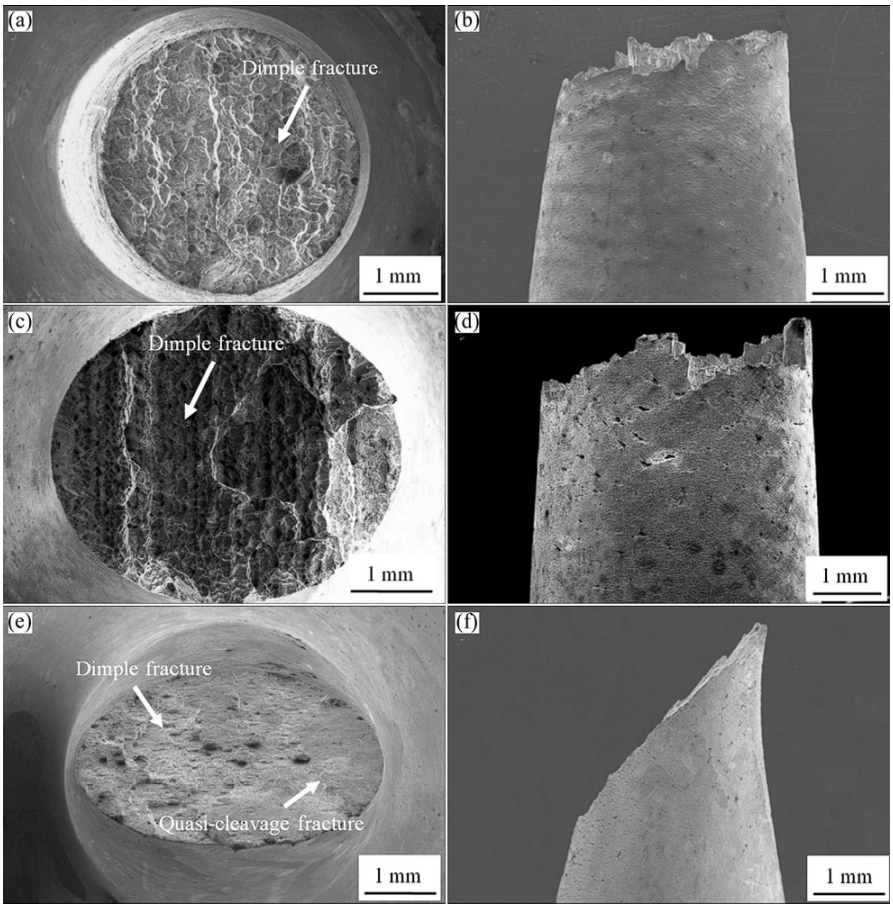

Figure 2.18: Fractured surfaces and longitudinal structures of tensile specimens at 1100 °C are shown for the following crystallographic orientations: (a, b) [100] specimen; (c, d) [120] specimen; (e, f) [110] specimen [17].

Wang et al.'s research [18], which was focused on crept samples, lends further support to these findings. Their study unveils distinct fracture modes experienced by different crystallographic orientations. At lower temperatures, diverse fracture types emerge: for example, [001] orientation manifests a fusion of cleavage and quasi-cleavage fractures, while [011] orientation engages in shear fracture propelled by a specific slipping mechanism. Concurrently, the [111] orientation experiences shear fracture via an alternative mechanism involving multiple slip systems. As temperatures rise, the common fracture mechanism across orientations involves void growth and coalescence. Notably, the topology of cleavage —defined by the structure of fracture surfaces— is profoundly influenced by the material's orientation. Unique sym-

metrical patterns emerge on cleavage surfaces for different orientations (see Figure 2.19). However, the percentage of the cleavage plane area is subject to the influence of temperature and stress magnitude. The underlying reason for the observed cleavage morphology is rooted in the nucleation and growth of voids at central positions, culminating in the creation of microcracks around these voids. The interaction of these microcracks along specific slip planes contributes to the formation of smooth cleavage planes [18].

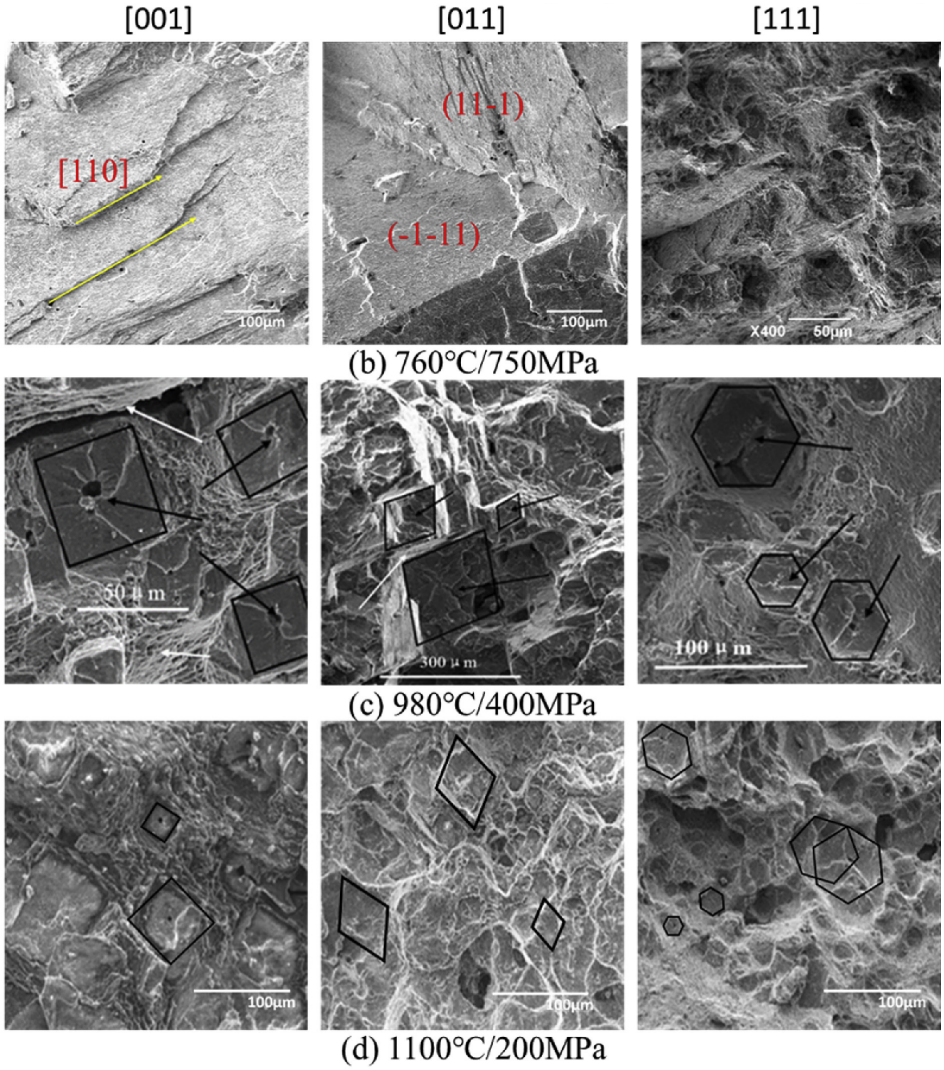

Figure 2.19: The morphology of creep fractures in specimens oriented along [001], [011], and [111] directions is examined at various combinations of temperature and stress levels, specifically at: (b) 760 °C and 750 MPa, (c) 980 °C and 400 MPa, (d) 1100 °C and 200 MPa [18].

Chapter 3

Comparison of Mechanical Properties in $\langle 001 \rangle$ and $\langle 011 \rangle$ Crystal Orientations of STAL15 Ni-Based Single-Crystal Superalloy

3.1 Introduction

STAL15's composition, consisting primarily of nickel, along with additions of chromium, cobalt, tungsten, aluminium and tantalum, gives it superior high-temperature strength, oxidation resistance, and creep deformation resistance. Its single-crystal architecture gives it anisotropic mechanical properties, meaning that its behaviour varies significantly between specific crystallographic orientations. Understanding these variations holds the key to unlocking the full potential of STAL15 in engineering applications.

This chapter aims to make a systematic comparison of the mechanical properties of STAL15 in two critical crystal orientations, namely $\langle 001 \rangle$ and $\langle 011 \rangle$. While the $\langle 001 \rangle$ crystallographic orientation is commonly employed in single-crystal superalloys due to its exceptional creep resistance and mechanical strength, the $\langle 011 \rangle$ orientation offers unique properties, such as higher ductility and higher anisotropy compared to

⟨001⟩, which may be advantageous for certain engineering applications.

A comprehensive analysis of engineering stress-strain graphs, yield strengths at critical temperatures, and hardening rates will be carried out to explore how STAL15 responds to mechanical loading under varying conditions.

3.2 Experimental Procedures

3.2.1 Materials

The primary application of STAL15 lies in the first stage turbines of land-based gas turbine engines [73]. Two types of single crystal bars were provided by Siemens Energy Sweden, with crystallographic orientations within 5°, from ⟨001⟩ and ⟨011⟩. The bars underwent a specific heat treatment process, involving solution heat treatment at 1280 °C for 1 hour and 1300 °C for 5 hours, followed by air cooling. Subsequently, the material underwent primary ageing treatment at 1100 °C for 8 hours and secondary heat treatment at 850 °C for 20 hours, both followed by air cooling [74]. The chemical composition of the material is detailed in Table 3.1 below.

Table 3.1: Chemical composition of the STAL15 single-crystal superalloy.

Element	Co	Cr	Al	Mo	W	Ta	Hf	Cu	Si	C	Ni
wt.%	5.2	15.1	4.4	0.97	3.8	8.2	0.095	0.042	0.18	0.035	Bal.

3.2.2 Methods

Tensile tests were conducted using an Instron 8862 ±100 kN servoelectric mechanical testing machine. Materials were heated using a three-region (top, middle, bottom) resistive heating furnace, capable of reaching temperatures up to 1200 °C. The furnace is equipped with three dedicated thermocouples (top, middle and bottom), which

are integrated within the system to provide accurate temperature monitoring and regulation throughout the experimental tests. To ensure measurement reliability, two additional thermocouples were strategically positioned on the top and bottom gauge sections of the tested samples.

Once the required temperature readings were attained for all thermocouples, a soaking time of 20 minutes was employed to achieve a thorough and uniform temperature distribution both internally and externally.

Video extensometry was utilised to obtain strain measurements from the tested samples. The Imetrum Video Gauge software was employed to extract the resultant strain data from the images captured by the video camera. An image representing the test bench with the furnace and camera installed is shown in Figure 3.1 below.

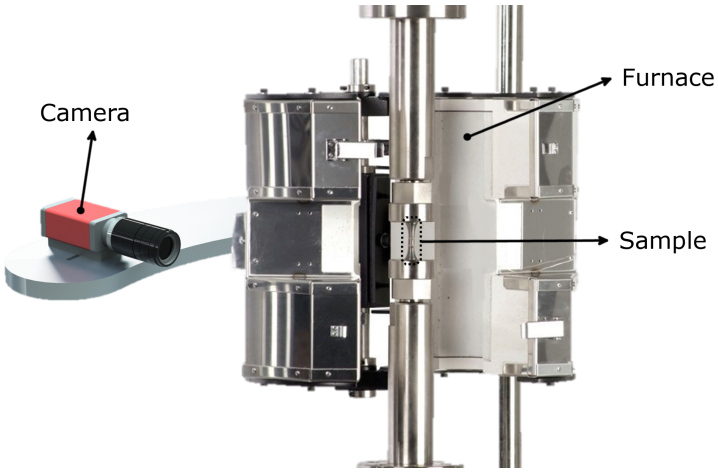

Figure 3.1: The Instron TMF test bench with furnace and camera installed.

To enable surface tracking for video extensometry and DIC, a speckle pattern was created on the sample surfaces. This pattern was achieved by using aerosol cans to spray a white primer and black paint with high-temperature properties on the samples, facilitating the tracking of changes on the deforming surfaces. Both the 1D digital strain gauge and the 2D digital strain map relied on this speckle pattern for accurate tracking during the tests. It's worth noting that due to the utilisation of aerosol cans in the creation of speckle patterns, variations in parameters such as

speckle size and distance were inevitable across different samples.

The digital extensometer length used was 6 mm, equivalent to the gauge length of the sample, allowing precise strain measurements during the tests. The sample geometry used for the tensile tests can be observed in Figure 3.2.

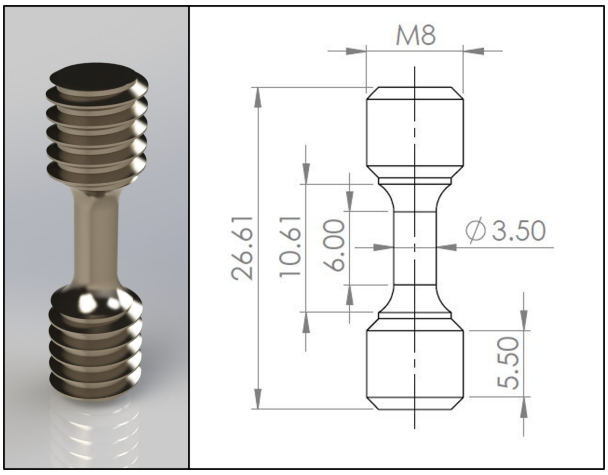

Figure 3.2: 3D model and drawing of the tensile test specimen. All dimensions are in mm.

3.3 Results and Discussion

3.3.1 Mechanical Testing

Mechanical tests on STAL15 for a range of temperatures, strain rates and orientations were made. Tensile test results were plotted onto engineering stress (MPa) vs. engineering strain (%) graphs and analysed for a deeper understanding of the material's reaction to changes related to the mentioned parameters. These types of graphs are used because crucial points including the yield point, ultimate tensile strength, and failure points can be identified more accurately, in comparison to true stress-strain graphs. As we are mainly interested in the section of the graph after the elastic region, graphs were plotted starting from an engineering stress of 400 MPa.

3.3.1.1 Effect of Temperature on ⟨001⟩

The initial tensile experiments were done on STAL15 ⟨001⟩ samples at a strain rate 10^{-3} s^{-1}, and temperatures of 24 °C and 300 °C. Figure 3.3 below shows the visible drop in the yield strength of the material with increasing temperature. The hardening rates for both temperatures are also similar and visibly constant. At a higher temperature of 600 °C (see Figure 3.4), it can be seen that the stage II hardening curve is slowly forming from the stage I curve, starting from a strain of around 2.5%. This transition from a single-hardening regime to a multiple one ends at 725 °C. Beyond this point, the initial hardening stage following the elastic region is no longer categorised as stage I but as stage II. After this temperature, there is a steady decrease in the 0.2% yield and ultimate tensile strengths with further increase in temperature, as seen from Figure 3.5.

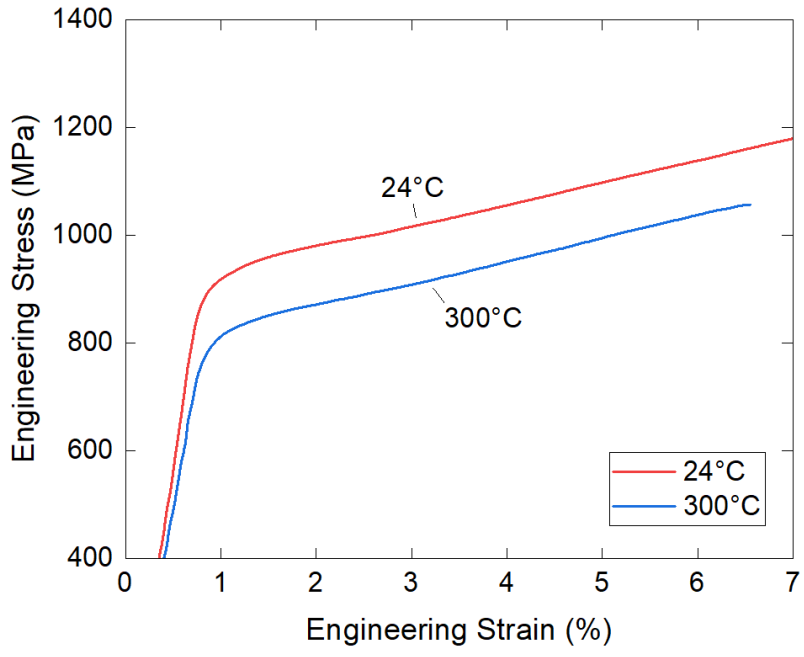

Figure 3.3: Effect of temperature from room temperature to 300 °C. Sample orientation ⟨001⟩, strain rate 10^{-3} s^{-1}.

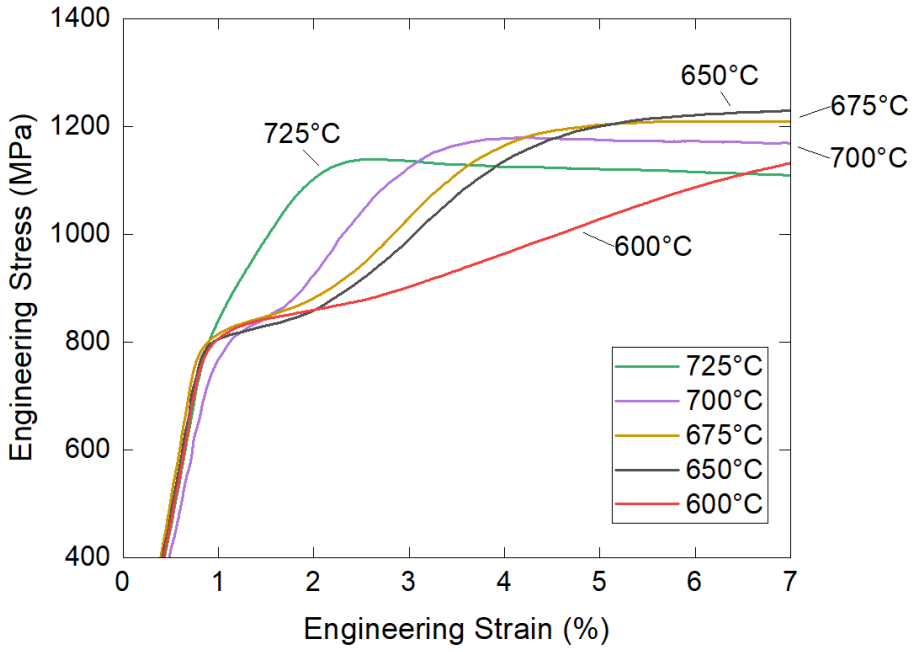

Figure 3.4: Effect of temperature from 600 °C to 725 °C. Sample orientation ⟨001⟩, strain rate 10^{-3} s^{-1}.

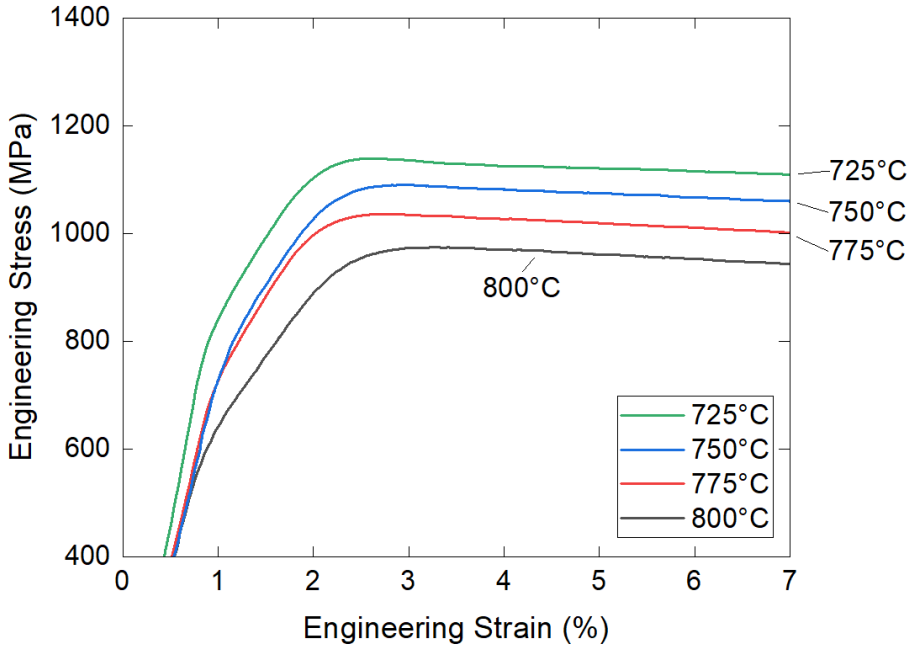

Figure 3.5: Effect of temperature from 725 °C to 800 °C. Sample orientation ⟨001⟩, strain rate 10^{-3} s^{-1}.

3.3.1.2 Effect of Temperature on ⟨011⟩

STAL15 ⟨011⟩ samples were also tested at a strain rate of 10^{-3} s^{-1} for the same temperatures. The resulting stress-strain curves were significantly different than the ones for the ⟨001⟩ crystal orientation. As seen in Figure 3.6, there is a clear decrease in yield strength from room temperature up to 600 °C. However, after 600 °C, the material seems to gain back the yield strength it had initially lost as the temperature is increased, up to 775 °C (see Figure 3.8). A transitioning stage (stage I to stage II) in terms of an increase in hardening rate seems to occur starting from 725 °C and ends at 775 °C. After this temperature, both the 0.2% offset yield and the ultimate tensile strength of the material drops with increasing temperatures (see Figure 3.8), an effect similar to the one seen in Figure 3.5 for ⟨001⟩. One other difference from the ⟨001⟩ crystal orientation is that from 300 °C to 700 °C, the samples rupture very rapidly, with strains less than 7%.

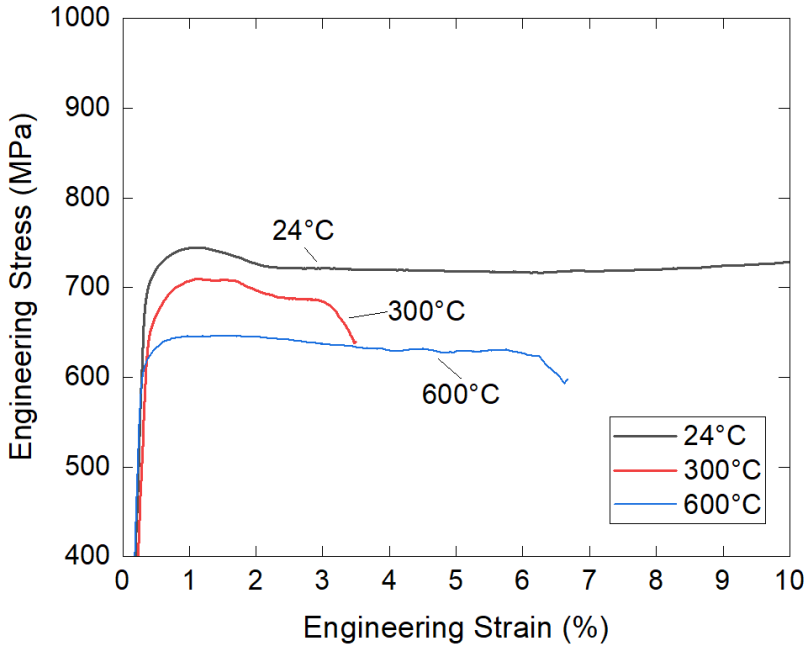

Figure 3.6: Effect of temperature from room temperature to 600 °C. Sample orientation ⟨011⟩, strain rate 10^{-3} s^{-1}.

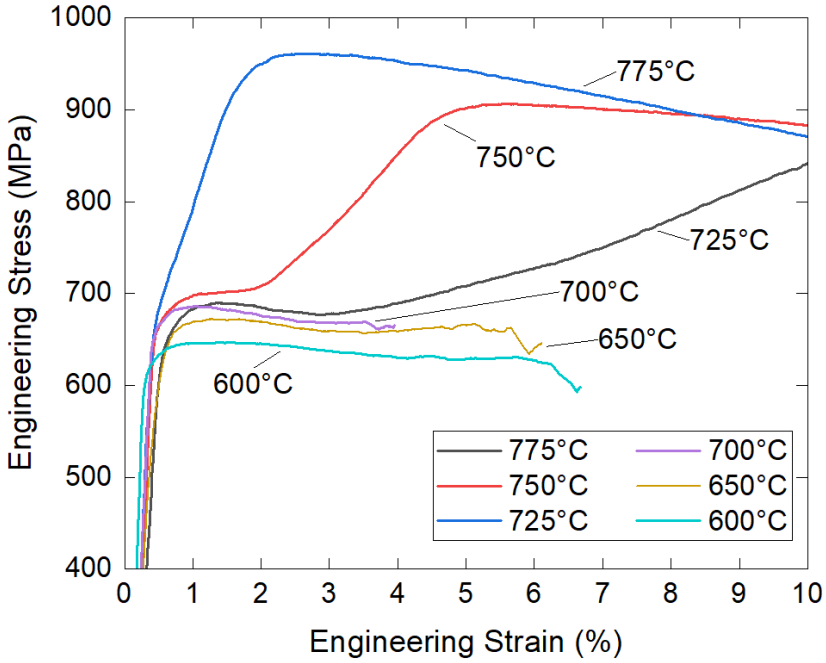

Figure 3.7: Effect of temperature from 600 °C to 775 °C. Sample orientation ⟨011⟩, strain rate 10^{-3} s^{-1}.

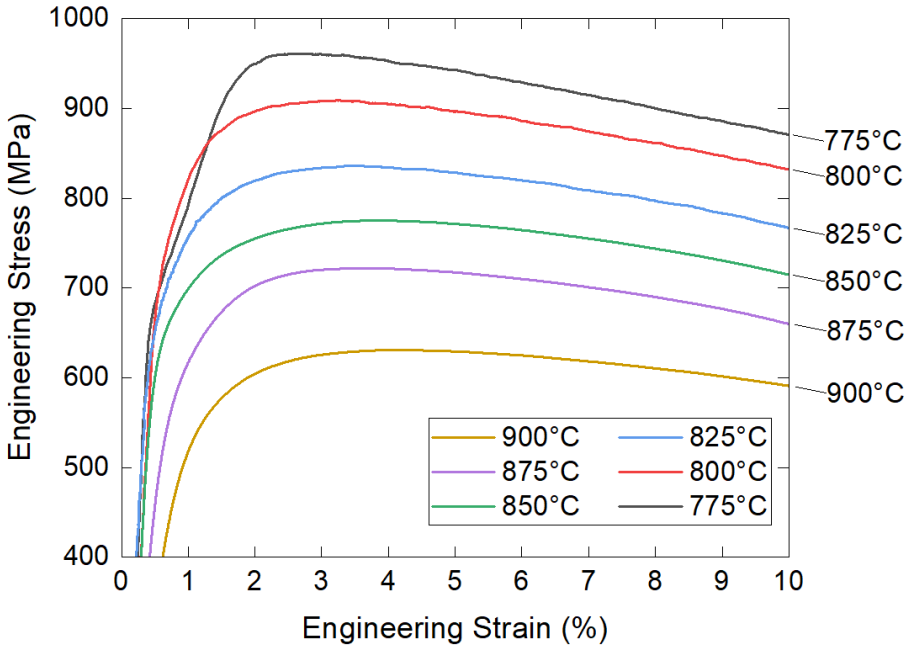

Figure 3.8: Effect of temperature from 775 °C to 900 °C. Sample orientation ⟨011⟩, strain rate 10^{-3} s^{-1}.

3.3.1.3 Effect of Strain Rate on ⟨011⟩

The strain rate sensitivity of STAL15 for the ⟨011⟩ crystal orientation was also studied. Results given below for temperatures of 825 °C (Figure 3.9), 850 °C (Figure 3.10), 875 °C (Figure 3.11) and 900 °C (Figure 3.12) show us the similarities between changes in strain rate and temperature. It can be seen that the stress-strain curves react similarly to a decrease in strain rate as they do to an increase in temperature. The transition of stage I hardening to stage II with increasing temperatures (at the end of elastic region) also happens the same way for decreasing strain rates, as seen from the graphs below. The main difference between the low vs. high strain rate deformation seems to be the premature fracture which happens at higher strain rates, approximately after the initiation of the stage II hardening. The transition from stage I hardening to stage II also seems to be more gradual for the higher strain rate; as the radius of the curve between stage I and stage II lines is visibly larger.

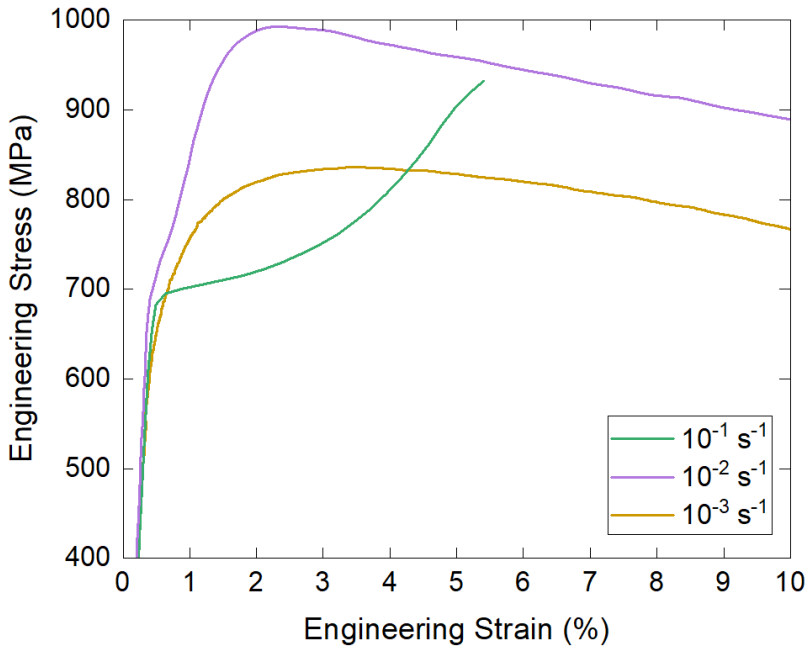

Figure 3.9: Effect of strain rate from 10^{-3} s^{-1} to 10^{-1} s^{-1}. Sample orientation ⟨011⟩, temperature 825 °C.

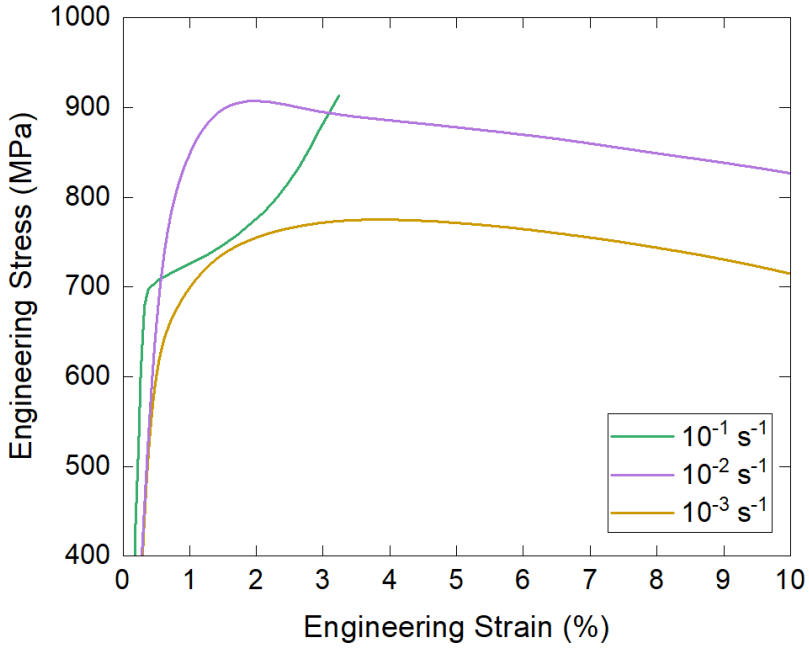

Figure 3.10: Effect of strain rate from 10^{-3} s^{-1} to 10^{-1} s^{-1}. Sample orientation $\langle 011 \rangle$, temperature 850 °C.

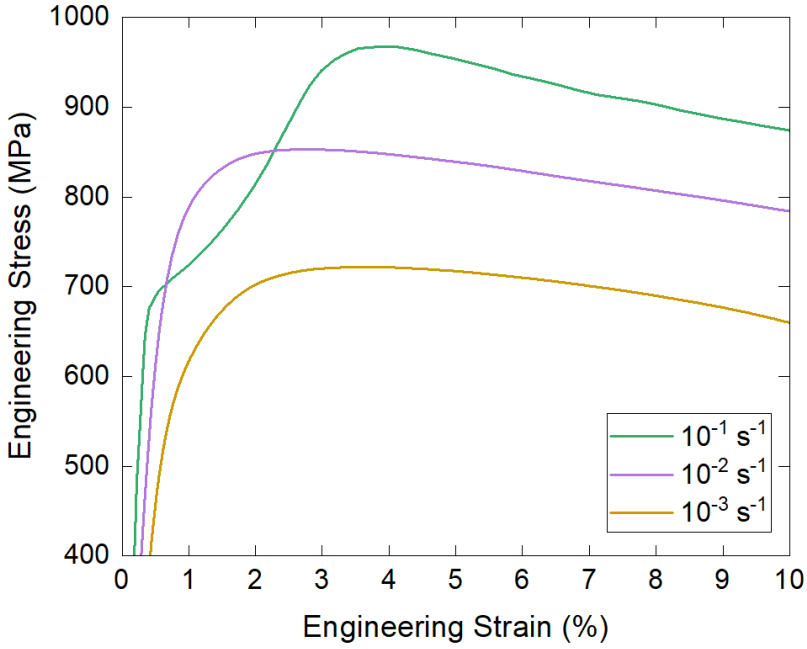

Figure 3.11: Effect of strain rate from 10^{-3} s^{-1} to 10^{-1} s^{-1}. Sample orientation $\langle 011 \rangle$, temperature 875 °C.

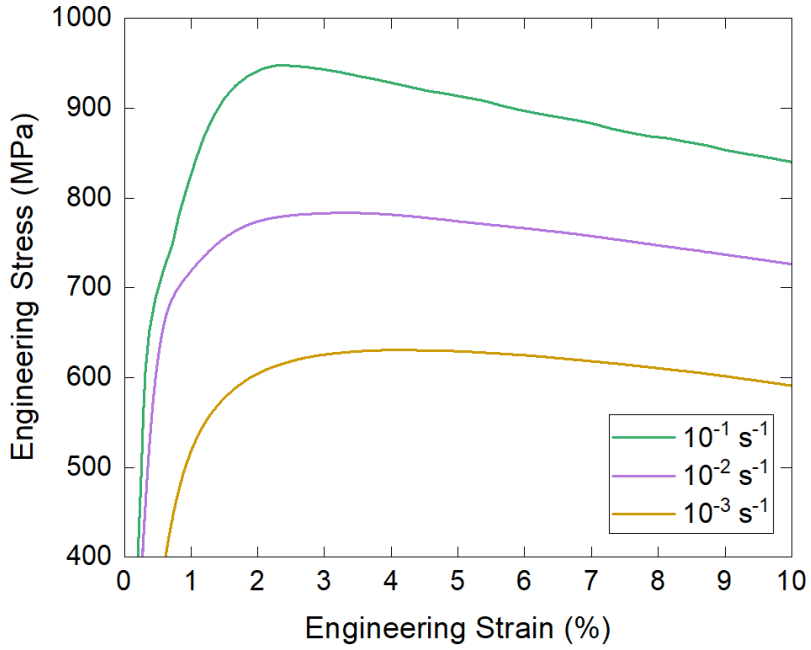

Figure 3.12: Effect of strain rate from 10^{-3} s^{-1} to 10^{-1} s^{-1}. Sample orientation $\langle 011 \rangle$, temperature 900 °C.

3.3.1.4 Comparison of Mechanical Properties

As seen in Figure 3.13 below, the 0.2% offset yield strengths of two crystal orientations, namely the $\langle 001 \rangle$ and $\langle 011 \rangle$ were compared at a strain rate of 10^{-3} s^{-1}. It can be seen that the anomalous yield phenomena terminates at different values and temperatures for the two different crystallographic orientations. Up to 800 °C, $\langle 001 \rangle$ is the stronger orientation; but for higher temperatures, $\langle 011 \rangle$ takes the lead. The high-temperature peak yield strength of $\langle 001 \rangle$ happens to be ≈910 MPa at 725 °C, while for $\langle 011 \rangle$ it is ≈770 MPa at 800 °C. This is in line with results from Ru et al. [53], as they have also found the peak yield strength of $\langle 001 \rangle$ to be higher, and the peak yield strength of $\langle 011 \rangle$ lower and occurring at higher temperatures.

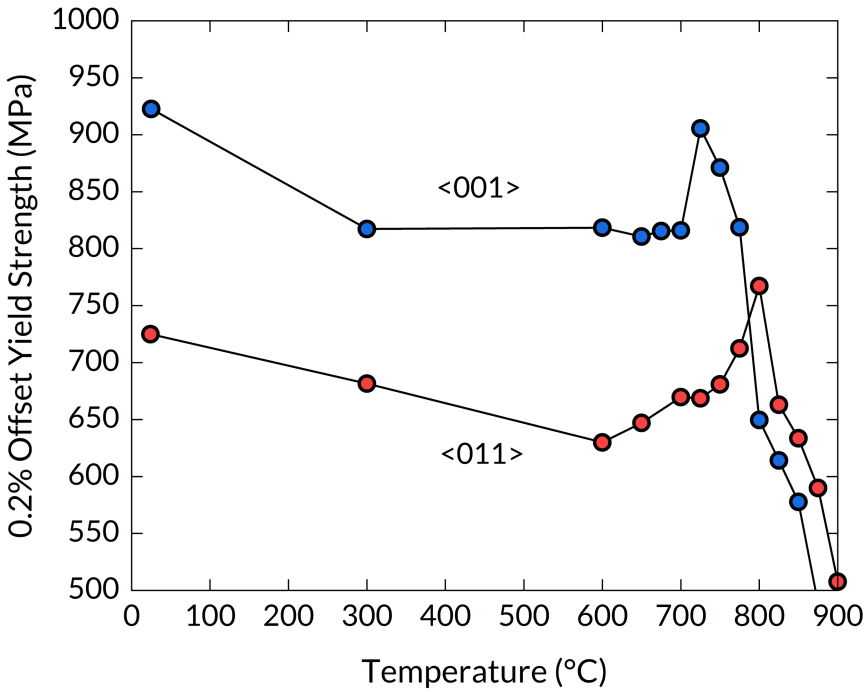

Figure 3.13: 0.2% offset yield comparison of $\langle 001 \rangle$ and $\langle 011 \rangle$ crystal orientations for different temperatures.

Figure 3.14 below shows the comparison of the measured elastic modulus values between the ⟨001⟩ and ⟨011⟩ crystallographic orientations. It can be seen that the elastic modulus values of ⟨011⟩ are higher than that of ⟨001⟩ for all temperatures, similar to previous literature [75, 76]. Another observation to note is that the elastic modulus of ⟨011⟩ is generally almost double that of ⟨001⟩, which is also in line with the work of Leidermark et al. [76]. Although the elastic modulus values for ⟨011⟩ seem to follow a general downtrend, the correlation is not as strong as it is for ⟨001⟩. The reason for this could be the high elastic anisotropy of the ⟨011⟩ crystallographic orientation, which would in turn affect the elastic modulus result depending on the digital extensometer location. Getting digital extensometer readings from around the sample could potentially help us to have a better understanding of the mechanical properties of such anisotropic materials.

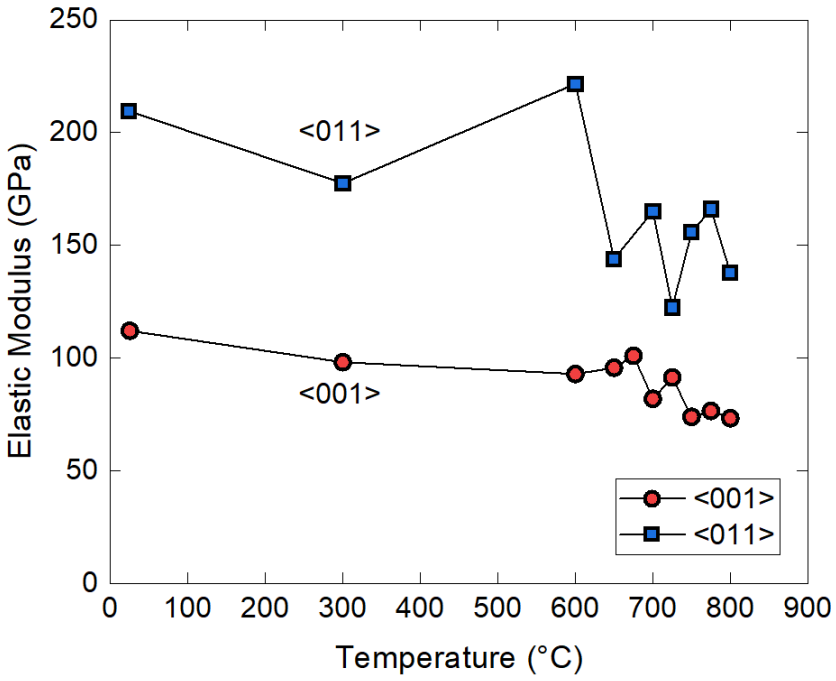

Figure 3.14: Elastic modulus comparison of ⟨001⟩ and ⟨011⟩ crystal orientations for different temperatures.

The stage II strain hardening behaviour for the ⟨001⟩ and ⟨011⟩ crystal orientations at a strain rate of 10^{-3} s^{-1} were also compared for temperatures up to 800 °C. To achieve this, true stress-strain curves and resulting hardening rates were plotted for each temperature, and the stage II hardening regions were determined in a qualitative manner, as seen in Figure 3.15 below. As the stage II hardening curves had not developed prior to 600 °C for the ⟨001⟩, and prior to 725 °C for the ⟨011⟩, they were not included in the comparative figure (see Figure 3.16). Average hardening rate (MPa) is calculated using the mean value of the stage II hardening curve slope. The hardening rate values are in line with previous single-crystal test results, such as Bezold et al. [77].

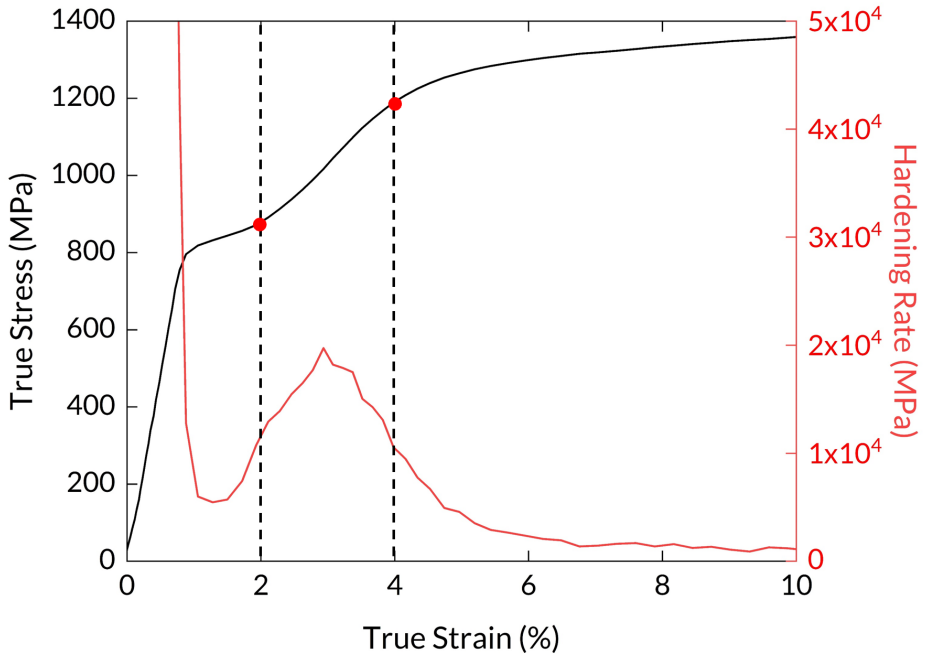

Figure 3.15: True stress-strain and hardening rate curves for STAL15 ⟨001⟩ at a strain rate of 10^{-3} s^{-1} and a temperature of 650 °C. The two vertical lines approximate where the linear hardening stage with a relatively high rate starts and ends, characteristic of stage II hardening [19].

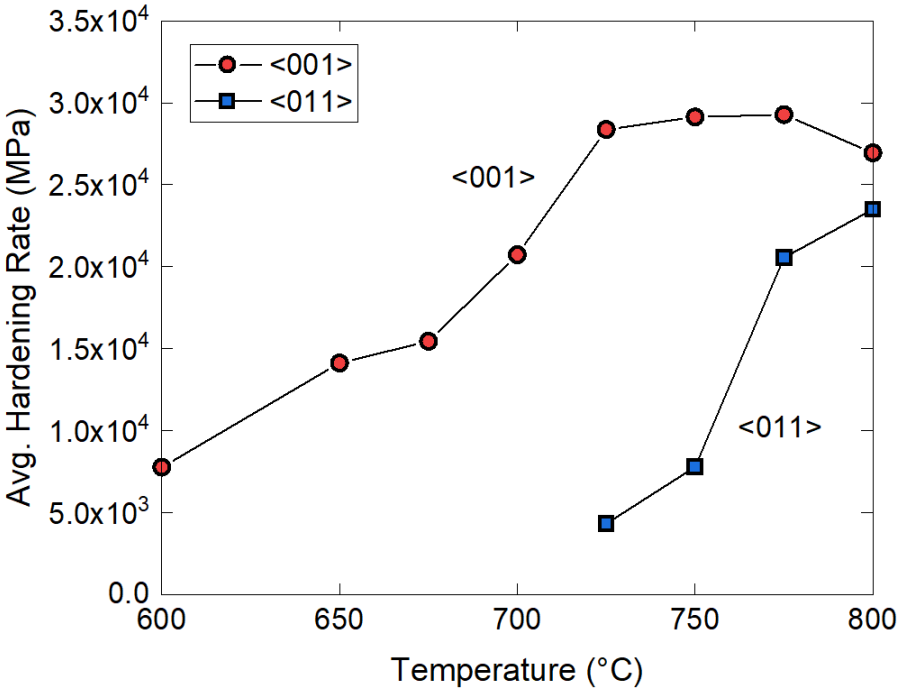

Figure 3.16: Stage II average hardening rates at a strain rate of 10^{-3} s^{-1} for temperatures from 600 °C to 800 °C.

3.4 Conclusions

Analysis of engineering stress-strain curves and comparison of mechanical properties were made for the ⟨001⟩ and ⟨011⟩ crystal orientations of STAL15 at different temperatures and strain rates. We can obtain the following findings:

- At lower temperatures, the ⟨001⟩ crystal orientation exhibits stage I hardening, while ⟨011⟩ softens.
- Both the ⟨001⟩ and ⟨011⟩ crystal orientations initially lose yield strength (0.2% offset) as temperatures increase. This is followed by an increase in yield strength, up to temperatures of 725 °C (for ⟨001⟩) and 800 °C (for ⟨011⟩), after which the material exhibits a sudden decrease in yield.

- The yield strength of $\langle 011 \rangle$ surpasses that of $\langle 001 \rangle$ after reaching a temperature of 800 °C.

- Compared to $\langle 001 \rangle$, determination of the elastic modulus of $\langle 011 \rangle$ crystal orientation is slightly more challenging due to its higher elastic anisotropy. Nonetheless, it is still evident that the $\langle 011 \rangle$ crystal orientation has a higher elastic modulus than $\langle 001 \rangle$.

- In terms of strain, it takes longer for the material to transition from stage I to stage II hardening at higher strain rates.

- The effect of temperature increase and strain rate decrease have similar effects on the engineering stress-strain curves. For both cases the stage I hardening curve eventually diminishes, leaving its place to stage II.

- For both orientations, the stage II hardening curve becomes steeper with increasing temperature and decreasing strain rate.

Chapter 4

Defining Anomalous Yield: Is There Really an Increase in Yield Strength?

4.1 Introduction

The definition of yield strength serves as the basis for establishing the concept of anomalous yield behaviour in Ni-based single-crystal superalloys. Theoretically, yield strength can be defined as the point at which the material transitions from the elastic state to the plastic state [78]. Practically, as it is quite difficult to locate this point, various offset yield strengths such as the 0.2%, 0.1%, 0.01% and the proportional limit have all been employed in the literature to help define yield strength thus far [79, 80, 81].

Yield anomaly is a unique phenomenon wherein the relationship between yield strength and temperature deviates from the typical trend. Unlike the anticipated weakening of yield strength at elevated temperatures, yield anomaly manifests itself as an increase in yield strength, followed by a sudden drop [82, 83, 84, 85, 86].

The main objective of this chapter is to challenge the conventional definition of the anomalous yield phenomenon by comparing different yield strength definitions, and to investigate whether there really is "an increase in yield strength with increasing

temperature". A multitude of tests for different temperatures in the 0.2% offset peak yield region will be made, to accurately locate at what temperature the peak exactly occurs; and SEM fracture surfaces will be analysed with the engineering stress-strain curves to try and understand the connection between the two. An appropriate offset yield strength combining theory and practicality for Ni-based single-crystal superalloys will also be proposed. Finding an apt definition of yield strength for STAL15 could also have implications for other Ni-based single-crystal superalloys.

4.2 Experimental Procedures

4.2.1 Materials

As previously described in Chapter 3, the material under investigation is STAL15 $\langle 001 \rangle$, a Re-free Ni-based single-crystal superalloy made and provided by Siemens. This material and orientation were selected to ensure the data obtained is relevant for industrial applications, as $\langle 001 \rangle$ is the crystal orientation used when producing gas turbine blades [87].

4.2.2 Methods

The methodology employed in this study involves a comprehensive investigation of the mechanical properties of STAL15 $\langle 001 \rangle$ through a series of tensile tests. The most appropriate yield strength definition for STAL15 $\langle 001 \rangle$ and by extension, for Ni-based single-crystal superalloys will be determined. To achieve this, a systematic approach was undertaken, involving the following steps:

Tensile tests were conducted over a wide temperature range, encompassing room temperature and elevated temperatures associated with the onset and conclusion of the yield anomaly phenomena. Compared to previous literature, a smaller temperature interval between the mechanical tests was used in order to achieve a better

understanding of the initiation and termination processes of the peak yield strength region.

Throughout the tensile tests, engineering stress-strain curves were generated for STAL15 ⟨001⟩. These curves provide crucial insights into the material's behaviour under varying conditions. A single camera and single digital extensometer DIC configuration were employed for strain data collection. The collected data was then subjected to analysis to compare different yield anomaly definitions and observe variations in engineering stress-strain curves across different temperatures.

In order to gain a deeper understanding of the microstructural influences on crack initiation and propagation mechanisms, fractography analysis was conducted using Scanning Electron Microscopy (SEM). Fractured surfaces of tensile samples were examined to identify key characteristics and potential causes of fracture. SEM images were captured from distinctive fracture surfaces of samples tested at 650 °C, 700 °C, 725 °C, and 800 °C.

Zeiss Merlin and JEOL JSM-6500F SEM instruments were employed for high-resolution imaging of the fracture surfaces. The analyses were conducted in secondary electron mode, utilising voltage settings ranging between 10-15 kV to ensure optimal imaging quality and resolution.

4.3 Results

4.3.1 Mechanical Testing

Tensile tests at a strain rate of $\langle 001 \rangle$ were conducted on STAL15, starting at room temperature up to 800 °C. The selected strain rate for all tests was 10^{-3} s^{-1} to ensure consistency in the measurements.

Offset yield strength measurements were made by obtaining the elastic modulus values at different temperatures, and then creating and offsetting a straight line to locate where it touches the engineering stress-strain graph. For the proportional limit case, the point where the linear line and stress-strain curve started to diverge was selected as the yield point. The resultant yield strength values for STAL15 $\langle 001 \rangle$ are plotted in Figure 4.1 below.

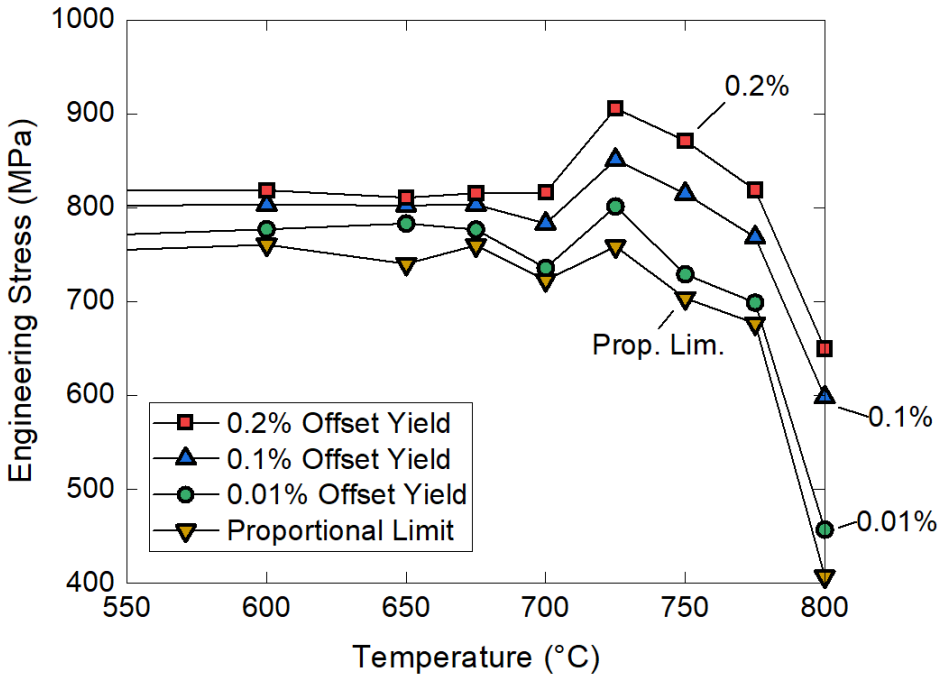

Figure 4.1: Various stress-temperature curves showing different yield strength definitions for varying temperatures. Sample orientation $\langle 001 \rangle$, strain rate 10^{-3} s^{-1}.

4.3.2 Scanning Electron Microscopy

To rationalise the transition occurring in engineering stress-strain graphs and yield strength with respect to temperature, fracture surfaces of STAL15 ⟨001⟩ samples were also investigated, as seen in Figure 4.2. Just like the transition occurring in the engineering stress-strain graphs shown previously in Chapter 3, the fracture surfaces also show a clear transition, from a brittle cleavage surface to a ductile dimpled one. Cleavage planes increase in number with increasing temperature, and after reaching maximum number of planes, the dimpled surface takes over, showing a change in fracture mechanisms.

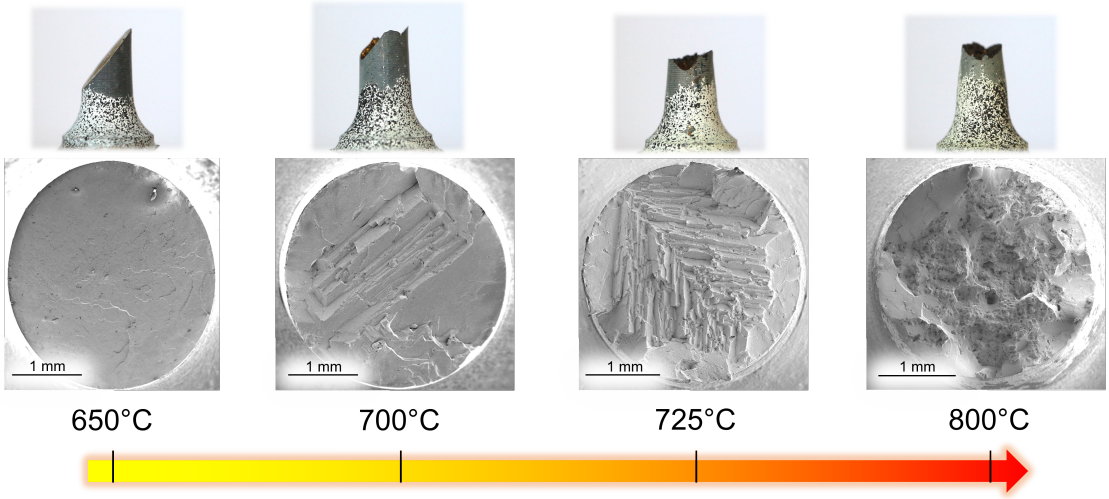

Figure 4.2: Longitudinal structures (above) and fracture surfaces (below) of STAL15 ⟨001⟩ samples ruptured at different temperatures.

4.4 Discussion

The analysis of yield strength vs. temperature curves across offset strains of 0.2%, 0.1%, 0.01%, and the proportional yield has revealed valuable insights. As anticipated, the higher offset yield strength definitions (0.2% and 0.1%) have led to results suggesting the presence of a yield anomaly; an increase in yield strength coinciding with an increase in temperature. However, with the utilisation of yield strength defi-

nitions which are closer to the elastic deformation line (0.01% and proportional limit), the assertion of a yield anomaly becomes less conclusive. Notably, while an increase in yield strength may not be apparent, there is still evidence of an anomaly in terms of yield strength retention, extending up to elevated temperatures. This divergence in results across different yield strength definitions can be attributed primarily to how the plastic region of the stress-strain curves develops with increasing temperatures. Visual representations of this change are given in Figure 4.3 below.

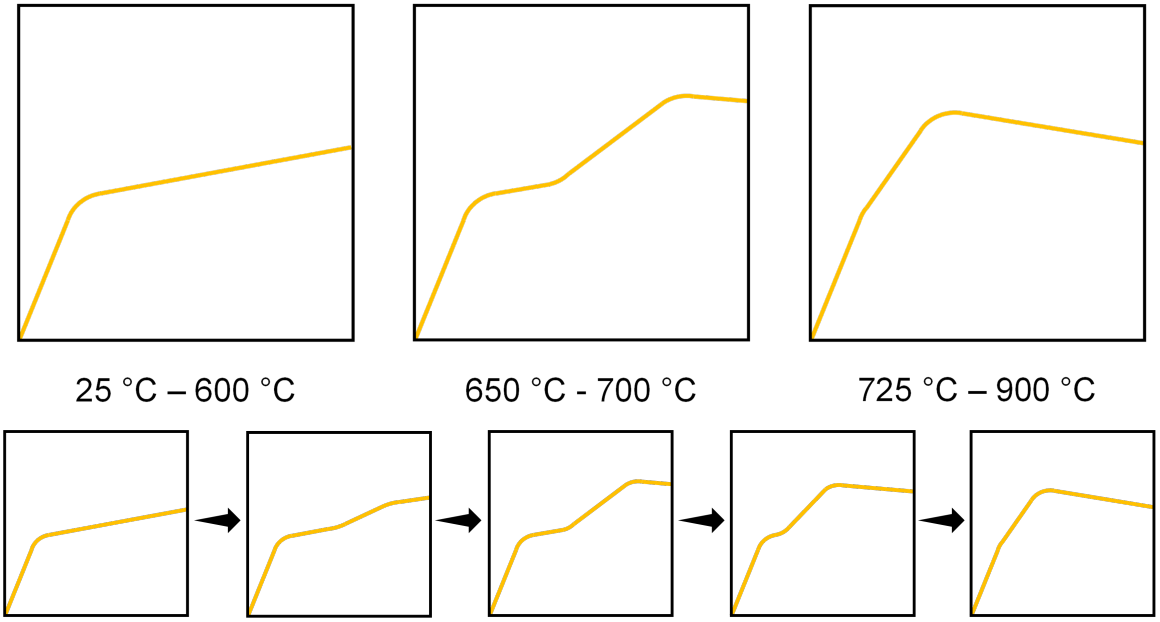

Figure 4.3: The effect of temperature on stress-strain graphs of STAL15 ⟨001⟩. Visual representations below show how the stress-strain curve transitions step by step.

Observing Figure 4.3, which depicts the initial to final states of STAL15 ⟨001⟩'s stress-strain behaviour, it becomes evident that the plastic region of these curves undergoes a significant shift; transitioning from a state characterised by a low hardening rate to one marked by a high hardening rate in response to increasing temperatures. Initially, the stress-strain curves exhibit a consistent pattern from room temperature to 600 °C, characterised by a more linear hardening region that persists until rupture

occurs. However, beyond the 600 °C threshold, a distinctive transformation takes place within the linear hardening region, resulting in the emergence of an additional hardening curve that progressively approaches the point where the elastic region concludes, correspondingly with the rise in temperature. This transition region ends at approximately 725 °C. Hence, when comparing the first stress-strain curve to the last one, we can see that there is a significant increase in the hardening rate that occurs right after the elastic line ends. As a result of this, a widening gap in stress emerges between the higher and the lower offset yields. This phenomenon is illustrated in Figure 4.4 below.

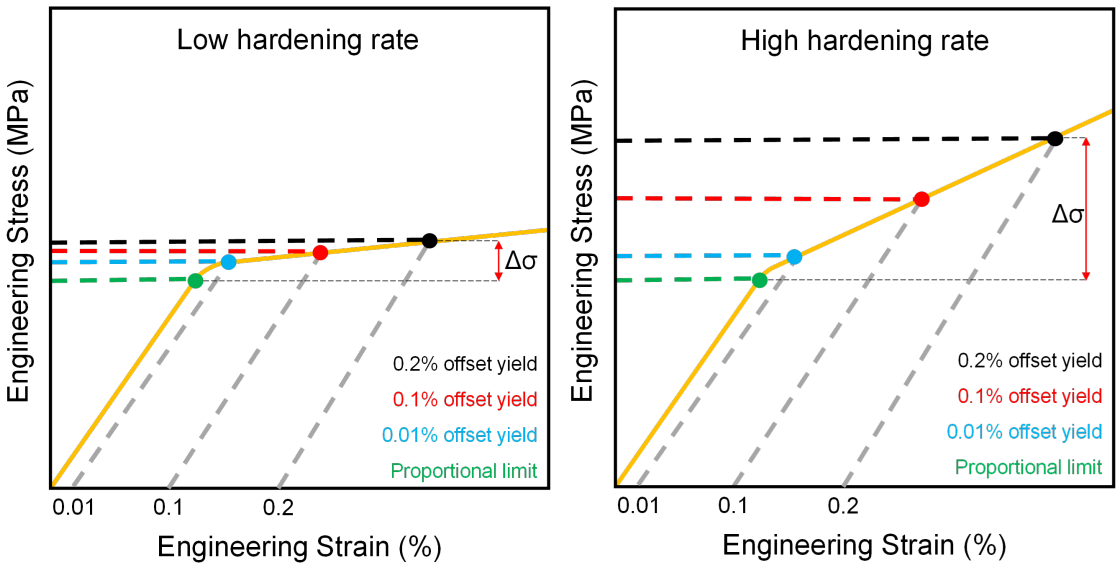

Figure 4.4: Visual representations illustrating measurement of offset yield strengths of a material characterised by a flatter hardening curve versus a steeper one. It is noteworthy that while both materials undergo the transition from the elastic to plastic regions at the same points (proportional limit), employing higher offset yield definitions produces greater yield strength results.

The observation that yield strength increases, or is significantly influenced, due to an escalation in the hardening rate, despite no alteration in the elastic portion, prompts consideration that higher yield strength definitions are susceptible to heightened inaccuracies. Consequently, it is advisable to refrain from employing these higher

definitions to attain a more accurate comprehension of material behaviour. This precaution is particularly crucial in the context of Ni-based single-crystal superalloys, as their stress-strain curves change significantly with respect to temperature. Comparison of the 0.2% and 0.01% offset yields of STAL15 ⟨001⟩ at various temperatures can be seen in Figure 4.5 below. Notice how the gap between 0.2% and 0.01% offset yield strengths increase significantly when the transition ends at 725 °C.

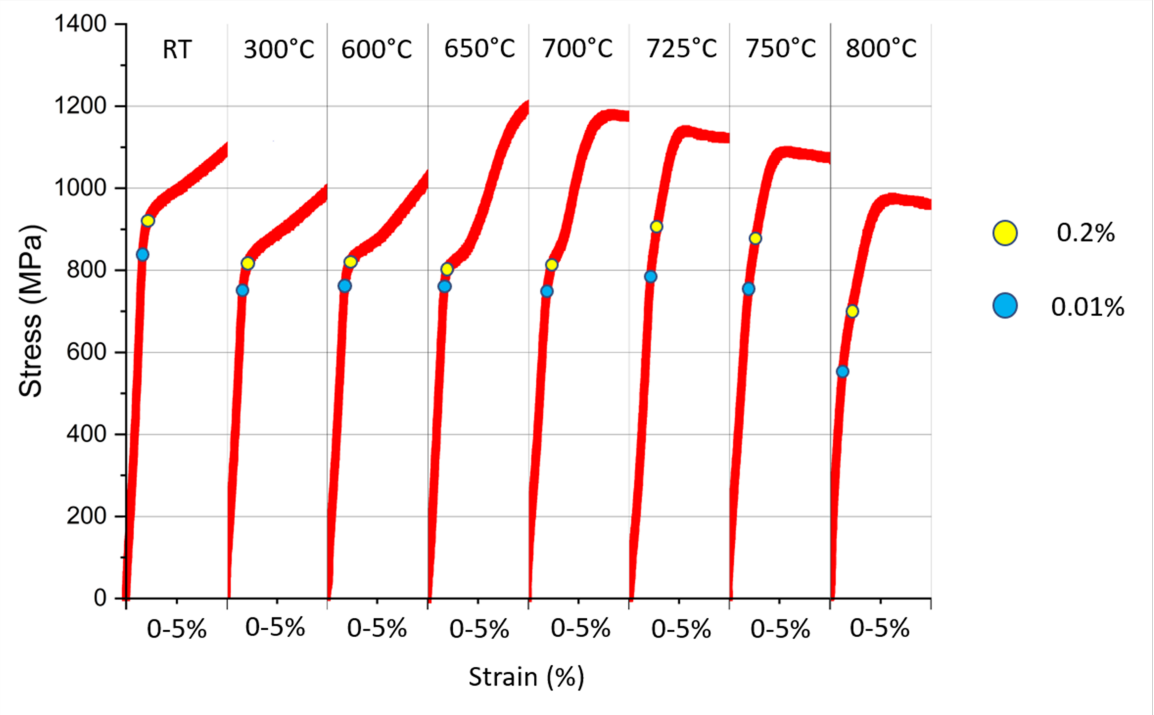

Figure 4.5: Engineering stress vs engineering strain graphs of STAL15 ⟨001⟩ comparing the 0.2% and 0.01% offset yield strengths at various temperatures.

The reason that the 0.2% offset yield was compared with the 0.01% offset yield rather than the proportional yield is because of the difficulties associated with locating where the proportional yield point resides. This uncertainty in locating the proportional yield point introduces ambiguity in the results. The proximity of the offset line to the elastic line complicates the task of identifying their intersection, owing to factors such as data noise and the potential non-linear characteristics of the

elastic line, particularly influenced by the material's anisotropic nature.

The results obtained from the SEM reveal a distinct transition that corresponds to changes in temperature. As depicted in Figure 4.6, at 650 °C (marking the initiation of the transition), the material exhibited a single-plane cleavage fracture. This is thought to occur due to the brittle nature of the material at lower temperatures, as brittle materials lack ductility and are more prone to immediate fracture once a crack is initiated. Cleavage fractures are highly directional and depend on the crystallographic orientation of the material. Materials with anisotropic properties, where mechanical behaviour varies with crystal orientation, are more prone to these types of fractures along specific crystallographic planes. The image on the right focuses on the cleavage river patterns on the surface of the ruptured sample. These patterns are important when locating crack initiation sites and crack propagation directions in fractographic studies [70]. Also, multiple cleavage planes are stacked very closely to one another as can be seen.

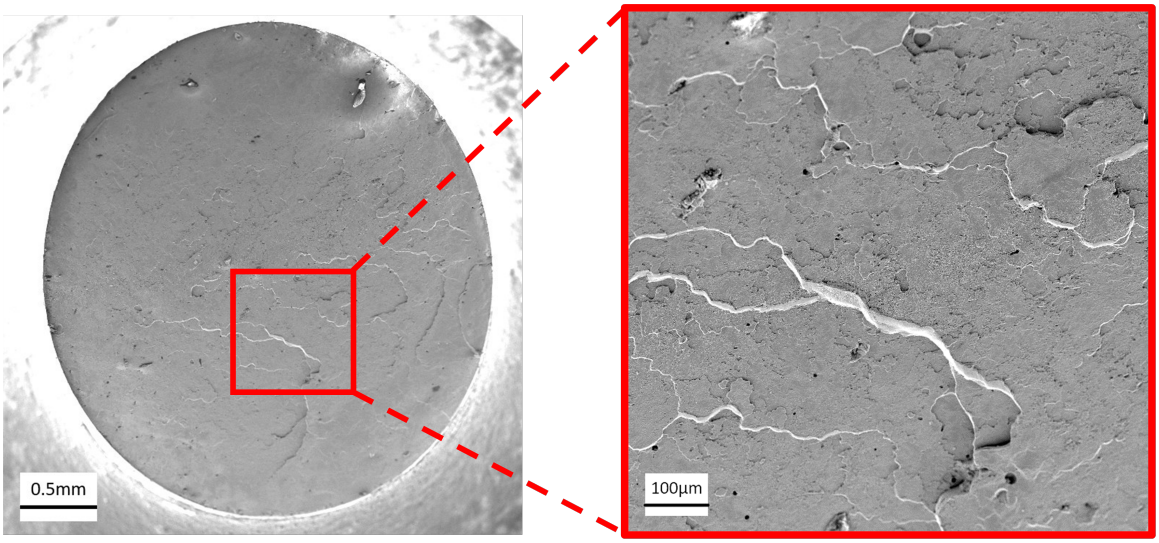

Figure 4.6: Fracture surface of STAL15 ⟨001⟩ at 650 °C.

With rising temperatures, the number of cleavage planes increases, as shown for 700 °C in Figure 4.7 below. This leads to a more stratified surface, specifically in the central part of the sample. The intersecting cleavage planes give rise to a surface

characterised by varying distances between these planes. Also notice the close-up image on the right, which shows a thicker river pattern.

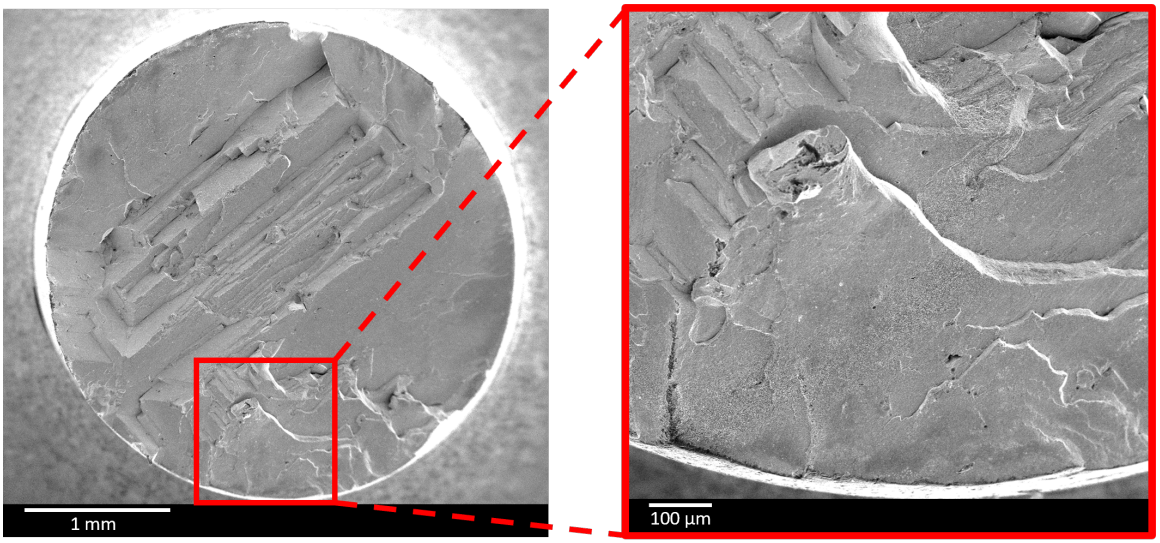

Figure 4.7: Fracture surface of STAL15 ⟨001⟩ at 700 °C.

At the conclusion of the stress-strain curve transition around 725 °C (as seen in Figure 4.8), this stratified slip plane pattern becomes highly pronounced across the entire surface, with the greatest concentration of cleavage planes. Dimples are also starting to form throughout the surface, indicating that the fracture is becoming more ductile. This combination of fracture mechanisms can be seen more clearly from the image on the right.

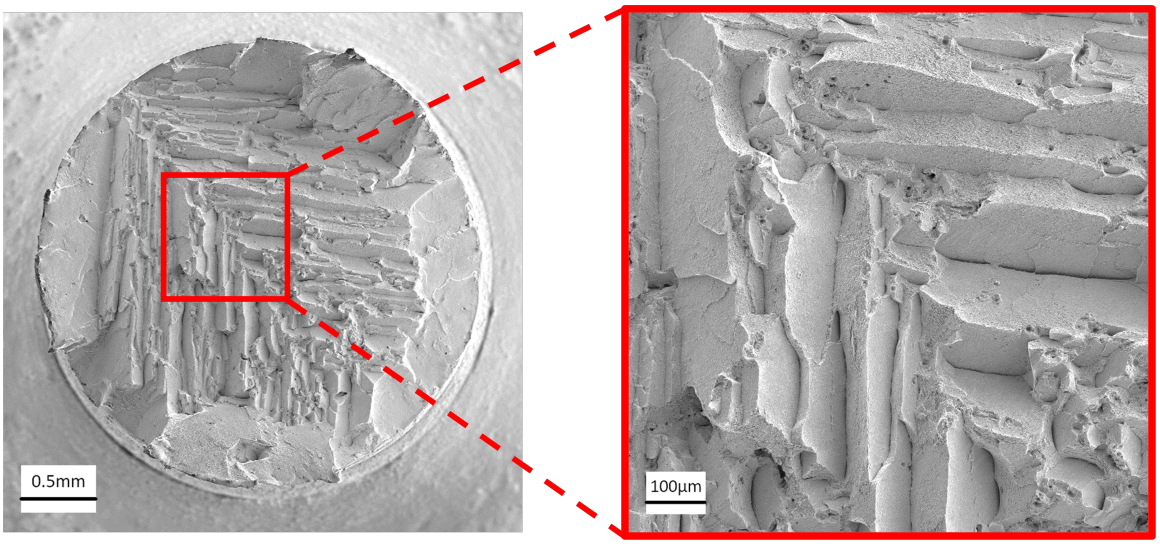

Figure 4.8: Fracture surface of STAL15 ⟨001⟩ at 725 °C.

Beyond this juncture, as temperatures continue to rise, the prevalence of cleavage planes gradually diminishes, leading to a transition towards a more dimpled fracture pattern. This change is particularly evident at 800 °C, as illustrated in Figure 4.9 below. The shift from a predominantly cleavage fracture to a dimpled fracture can reflect changes in the material's microstructure, such as the activation of different slip systems, or variations in dislocation behaviour. Cleavage fracture involves cracks propagating along specific crystallographic planes, often seen in brittle materials under low ductility conditions. In contrast, dimpled fractures reflect a more ductile behaviour, with energy absorption through plastic deformation and void growth, leading to dimple-covered surfaces.

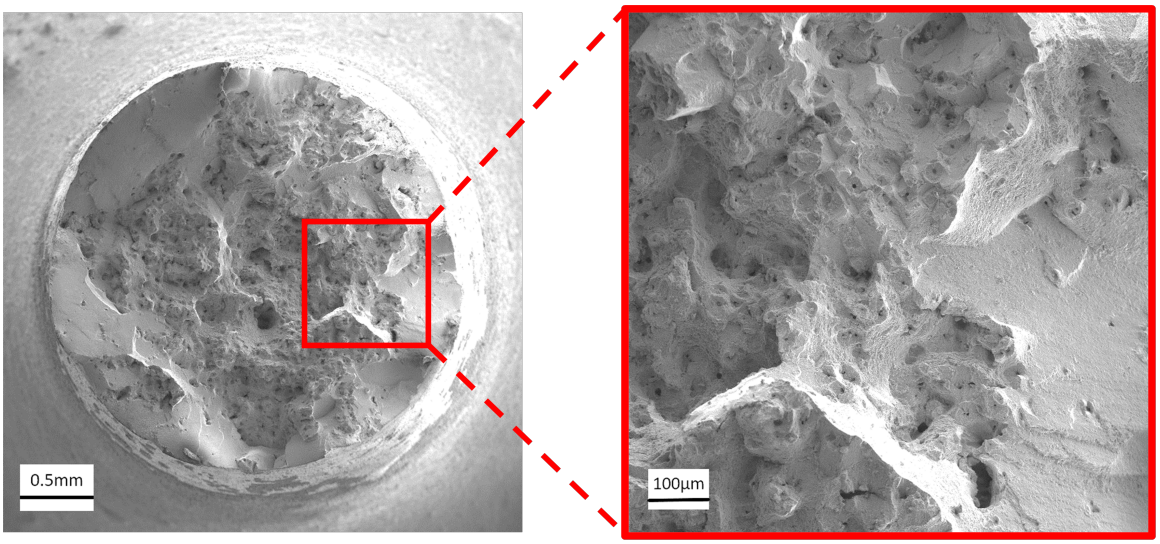

Figure 4.9: Fracture surface of STAL15 ⟨001⟩ at 800 °C.

Given the pronounced anisotropic nature of our material, employing a multi-camera configuration could have provided a more comprehensive understanding of stress-strain curves, capturing diverse responses from various regions of the sample, particularly in the elastic region. Additionally, extending this methodology to investigate other Ni-based single-crystal superalloys would contribute to drawing more conclusive insights from our findings and further enriching this discussion.

While this research primarily centered on the macroscopic characterisation of the material, enhancing its depth through a microlevel investigation involving SEM and TEM analyses would provide a more comprehensive understanding of the microscale dynamics and the underlying microstructural mechanisms contributing to the observed transition. This approach would offer a direct link between macroscopic observations and microstructural changes, potentially elucidating the driving forces behind the observed behaviour. Coupling the macroscopic trends with these detailed microstructural investigations would not only provide a well-rounded comprehension of the cleavage-to-dimpled fracture transition but also contribute to an enriched understanding of the material's mechanical behaviour as a whole.

By conducting tests that are deliberately interrupted around the 0.2% offset yield

point and subsequently investigating/quantifying the microstructural changes that occur, valuable insights could be gained to determine conclusively whether the anomalous yield phenomenon (increase in yield strength with rising temperature) is indeed present. If it can be shown that the elastic limit of the material does indeed increase with rising temperature, it can be said without doubt that there is an anomalous yield in terms of an increase in yield strength. Otherwise, the anomaly has to be defined as a retention of yield strength or in terms of anomalous work hardening, as Suzuki et al. [88] and Bezold et al. [6, 77] have previously done.

4.5 Conclusions

This study aims to determine the appropriate methodology for defining yield strength in Ni-based single-crystal superalloys through a comparative analysis of different yield strength definitions. Mechanical tests were conducted at varying temperatures, and engineering stress-strain curves were constructed to reveal the relationship between curve behaviour and yield strength. The primary outcomes of this chapter are as follows:

- Higher offset yield strength definitions (0.2% and 0.1%) suggest the presence of a yield anomaly, demonstrating an increase in yield strength as temperature rises, while definitions closer to the elastic deformation line (0.01% and proportional limit) yield results that do not. Using this methodology, we cannot say that there is a yield anomaly effect in Ni-based single-crystal superalloys, as it is dependent on the method used to identify yield strength. The anomaly in yield is not due to the material strengthening with rising temperatures, but due to it retaining its strength with it.

- The variations in higher offset yield strengths are primarily attributed to the development of the plastic region in stress-strain curves as temperature increases.

The gap in mentioned yield strength values becomes very high the moment transition of the stress-strain curve is completed, leading us to think that higher yield stress definitions are strongly affected by the changes in the plastic region- as the transition happens not on the elastic but the plastic portion of the stress-strain curve.

- Determining the most appropriate offset yield strength definition for Ni-based single-crystal superalloys involves a delicate balance between the accurate representation of material behaviour and practical considerations. The choice of a 0.01% offset yield strength appears to strike this balance effectively. This decision is based on careful consideration of two key factors: the challenges associated with measurement, as seen in the case of proportional yield, and the potential influence of the plastic region, as observed with the 0.2% and 0.1% offsets.

Chapter 5

Measurement Difficulties in Tensile Testing of Ni-Based Single-Crystal Superalloys

5.1 Introduction

Tensile testing is a fundamental and widely used technique in materials science and engineering to assess the mechanical properties of materials under tensile loading [89]. The information obtained from these tests is invaluable for designing materials for various applications and ensuring structural integrity in engineering components. However, despite its significance, the accuracy and reliability of tensile test results can be influenced by various sources of measurement errors, ranging from specimen preparation to instrumentation and data analysis.

When it comes to tensile testing of anisotropic materials, the challenges and considerations are further heightened due to their directional dependence in mechanical behaviour. These materials possess different mechanical properties along different crystallographic orientations, leading to complex deformation behaviours. While traditional extensometers have been widely used for strain measurement of isotropic ma-

terials, they have limitations in capturing the full complexity of the anisotropic material behaviour, primarily due to their single-point measurement capability and lack of sensitivity to strain variations along different crystallographic orientations. Contact extensometers may also be susceptible to errors arising from specimen preparation, misalignment, and surface roughness effects. Additionally, contact-based measurements can sometimes influence the behaviour of the material being tested, especially at high temperatures. Video extensometry using Digital Image Correlation (DIC) eliminates these potential sources of errors since it is a non-contact technique, capturing strain data through optical analysis. It effectively minimises the impact of surface roughness, misalignment, and preparation errors on the measured strains, ensuring more accurate and reliable data; which is critical for understanding the mechanical response to external loads and characterisation of anisotropic properties.

As will be shown in this chapter, with dual-camera video extensometry, this capability can be further enhanced. Two cameras are positioned at orthogonal angles, capturing the strain in two perpendicular directions simultaneously. This comprehensive strain data enables us to gain a deeper understanding of the anisotropic material's response to applied loads and the spatial variation of strain across the specimen, as strains are recorded from different locations; including both normal strains and shear strains. Dual-camera DIC also provides a means of validation by comparing strain measurements obtained from different camera views, reducing the potential for experimental errors or artifacts. Consistency among the measurements from the dual-camera setup enhances confidence in the reliability of our experimental data.

5.2 Experimental Procedures

5.2.1 Materials

For a comprehensive investigation of the results, tensile tests were performed on two distinct materials: STAL15 (single-crystal, anisotropic) and AD730 (polycrystal, isotropic). The contrasting behaviours exhibited by these materials due to their anisotropic and isotropic nature make the comparison of their stress-strain responses intriguing.

The anisotropic material selected for this study, STAL15, is a Re-free Ni-based single-crystal superalloy (introduced in Chapter 3; see Table 3.1). The isotropic material, AD730, is a nickel-based polycrystalline superalloy. Unlike STAL15, AD730 did not undergo any heat treatment prior to the tensile tests. This material finds applications in a variety of fields, including aero engine components, land-based turbines, and fasteners used in high-temperature applications [20]. The chemical composition of the material is given in Table 5.1 below.

Table 5.1: Chemical composition of the AD730 polycrystalline superalloy [20].

Element	Co	Cr	Al	Mo	W	Ti	Fe	Nb	Zr	B	C	Ni
wt.%	10	17	2.5	3.5	3	3.9	5	1.4	0.05	0.02	0.02	Bal.

5.2.2 Methods

The methods used are the same as the ones used in Chapter 3. The only difference is in terms of the number of cameras and digital extensometers used.

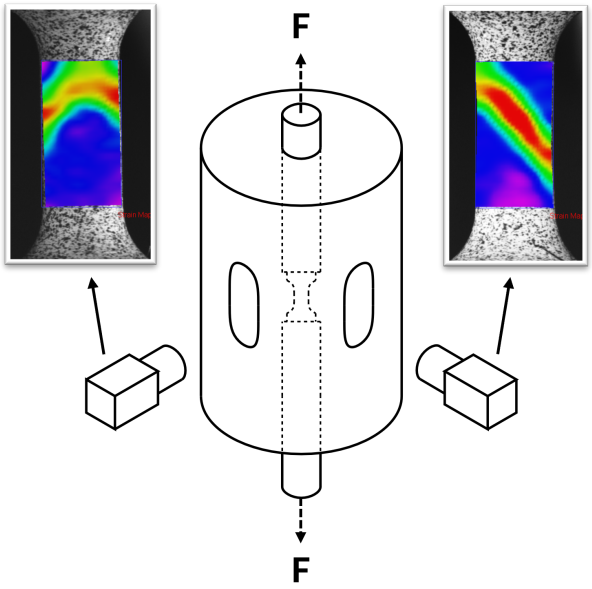

Figure 5.1: Diagram of the test bench and the orthogonal dual-camera configuration.

For accurate video extensometry and Digital Image Correlation (DIC) measurements, an orthogonal dual-camera configuration was utilised, as depicted in Figure 5.1.

Three digital extensometers were used on each video recorded by the cameras. These digital extensometers captured strain data from different locations on the specimen's surface (middle, left and right). The extensometer alignment was carefully adjusted, with each camera using a uniquely coloured extensometer —yellow for Camera 1 and green for Camera 2— to record strains from the same location on the specimen (see Figure 5.2). This arrangement ensured accurate validation of the strain measurements.

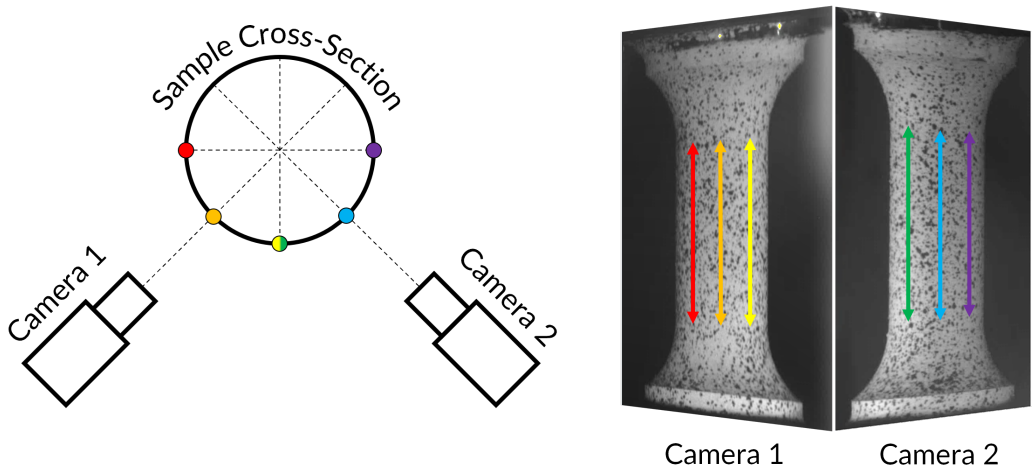

Figure 5.2: Digital extensometer setup and colour convention for the experiments. Arrows indicate the location and length of the extensometers. Notice the colours yellow and green are on the same location of the sample. This colour convention will be used to denote digital extensometer locations throughout the chapter.

The loading direction was aligned with the longitudinal axis of the specimen. The universal testing machine applied a uniaxial tensile force until fracture occurred, while the cameras continuously recorded the deformation of the specimen's surface.

The recorded videos from the dual-camera DIC setup were processed using specialised software to obtain the strain data. True stress vs. true strain curves were generated for each strain rate and temperature condition. Strain data from the three digital extensometers on each camera were compared and analysed to ensure consistency and repeatability.

Tensile tests were conducted over a range of temperatures and strain rates, as outlined in Table 5.2 below. The samples were tested under varying conditions until failure to obtain comprehensive data on their mechanical behaviour.

Table 5.2: Tensile test parameters.

Experiment #	1	2	3	4
Material	AD730 & STAL15 ⟨001⟩	STAL15 ⟨001⟩ & ⟨011⟩	STAL15 ⟨011⟩	STAL15 ⟨011⟩
Temperature	675 °C	825 °C	825 °C	825 °C, 850 °C, 875 °C, 900 °C
Strain Rate	10^{-3} s^{-1}	10^{-3} s^{-1}	10^{-3} s^{-1}, 10^{-2} s^{-1}, 10^{-1} s^{-1}	10^{-1} s^{-1}

After conducting the tensile tests until failure, the fractured specimens were carefully collected for further analysis. The fractured surfaces of the samples were then examined using a 3D optical profilometer to gain valuable insights into their morphological characteristics. This analysis provided essential information on the anisotropy of the samples including aspect ratio and other topographical features.

The optical profilometer allowed for a detailed and precise examination of the fractured surfaces, providing a comprehensive understanding of the fracture patterns and mechanisms. The aspect ratio, which represents the ratio of the shortest to the longest diameter of the deformed surface, offered valuable clues about the nature of the anisotropic deformation.

5.3 Results

5.3.1 Mechanical Testing

5.3.1.1 AD730 vs. STAL15 ⟨001⟩

To understand the effect of crystal structure, tensile tests were conducted on AD730 and STAL15 ⟨001⟩ at an elevated temperature of 675 °C and a strain rate of 10^{-3} s^{-1}. Six digital extensometer readings were obtained for each material.

The true stress vs. strain results for AD730 demonstrated consistency in the elastic region, indicating its isotropic behaviour (see Figure 5.3). Conversely, the true stress

vs. strain readings obtained from the elastic region of STAL15 ⟨001⟩ demonstrated non-linear responses, characterised by curved lines, deviating from the anticipated linear behaviour typically observed in conventional elastic materials; revealing the strong anisotropic nature of the material at this temperature (see Figure 5.4).

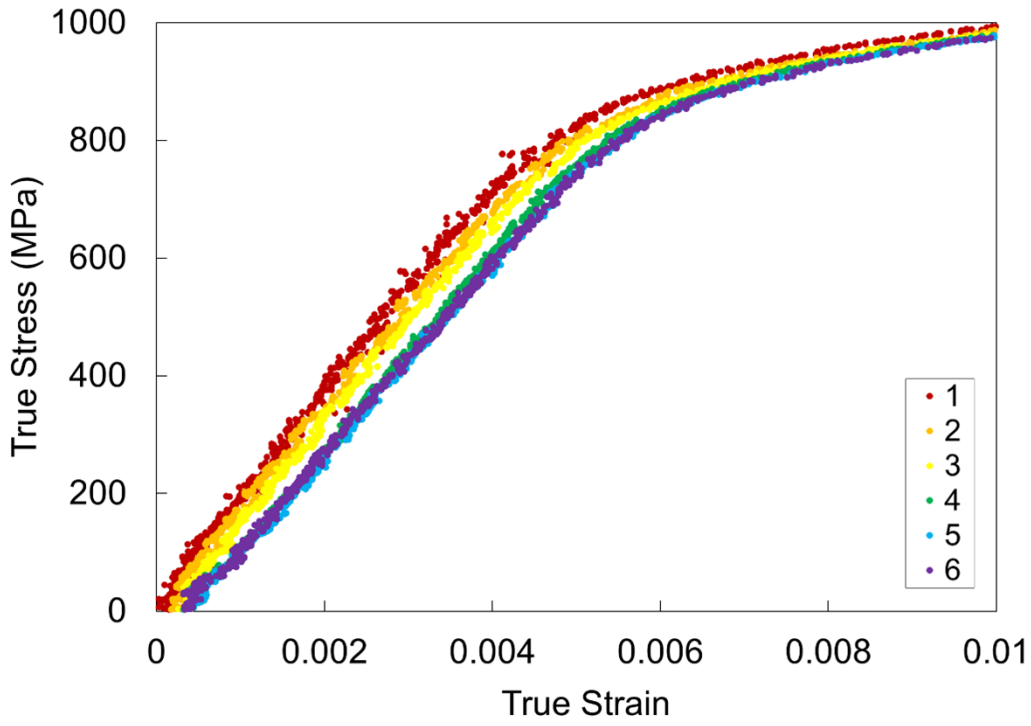

Figure 5.3: True Stress vs. True Strain graph of AD730 at 675 °C.

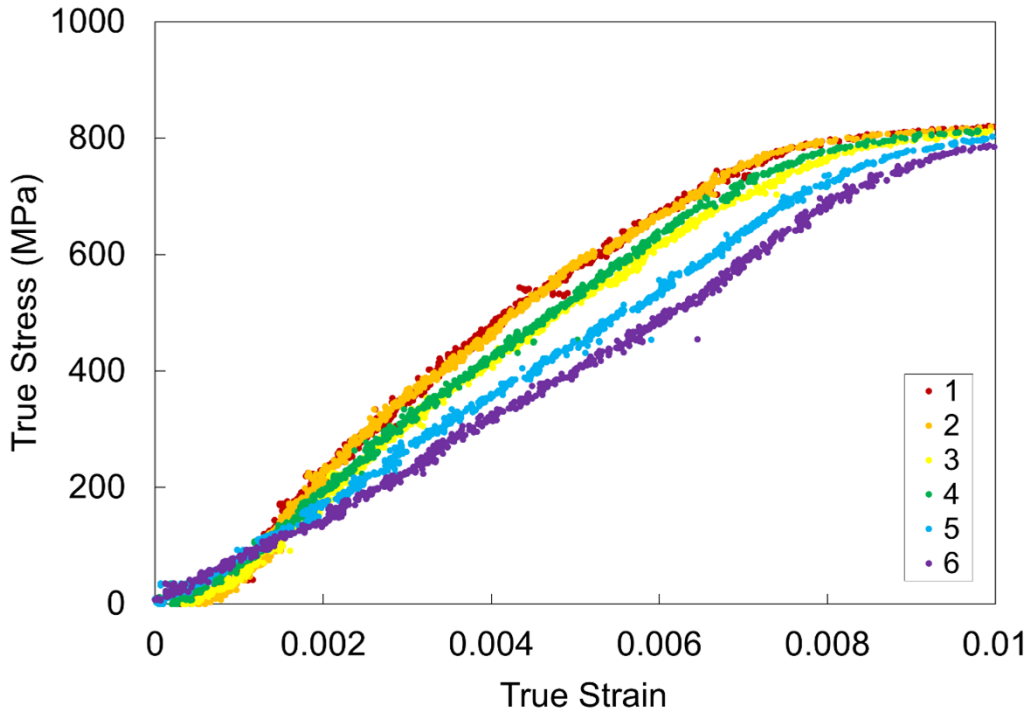

Figure 5.4: True Stress vs. True Strain graph of STAL15 ⟨001⟩ at 675 °C.

The elastic modulus was determined by employing linear regression analysis, fitting straight lines to the true stress vs. true strain curves' elastic regions. For both cases, the straight lines were created using data points between 200 to 600 MPa. The elastic modulus calculated for both materials and all curves using this method have been given in Table 5.3 below:

Table 5.3: Elastic moduli calculated from different regions of the AD730 and STAL15 ⟨001⟩ samples. Colour coding of camera numbers are as follows: 1= Red, 2= Orange, 3= Yellow, 4= Green, 5= Blue, 6= Purple.

Camera #	1	2	3	4	5	6	Mean
E (GPa) AD730	179.3	169.7	169.8	169.8	160	164.4	167.2
E (GPa) STAL15	117.9	118	105.6	108.7	91.1	86.8	104.7

The analysis of the elastic modulus values obtained from the six cameras revealed variations in the mechanical response of the samples. For AD730, the maximum elastic modulus recorded was found to be approximately 179.3 GPa, while the minimum elastic modulus was measured at approximately 160 GPa. To quantify the difference between the maximum and minimum results in terms of percentage, the percentage difference (PD) was calculated using the following formula:

$$PD = \frac{Max.Value - Min.Value}{(Max.Value + Min.Value)/2} * 100$$

This percentage difference also correllates to the degree of anisotropy of the sample. For AD730, the percentage difference between maximum and minimum values yielded an approximate value of 11.38%. For the anisotropic STAL15 $\langle 001 \rangle$, the percentage difference was found to be almost 3 times higher, at 30.47%, indicating a significantly greater degree of anisotropy.

5.3.1.2 STAL15 $\langle 001 \rangle$ vs. STAL15 $\langle 011 \rangle$

In an effort to understand the effect of crystal orientation and temperature, further investigations were carried out on different orientations of STAL15 at an elevated temperature of 825 °C, maintaining the same strain rate of 10^{-3} s^{-1}. These experiments involved testing the material in two different crystallographic orientations, namely $\langle 001 \rangle$ and $\langle 011 \rangle$ (see Figure 5.5 and 5.6).

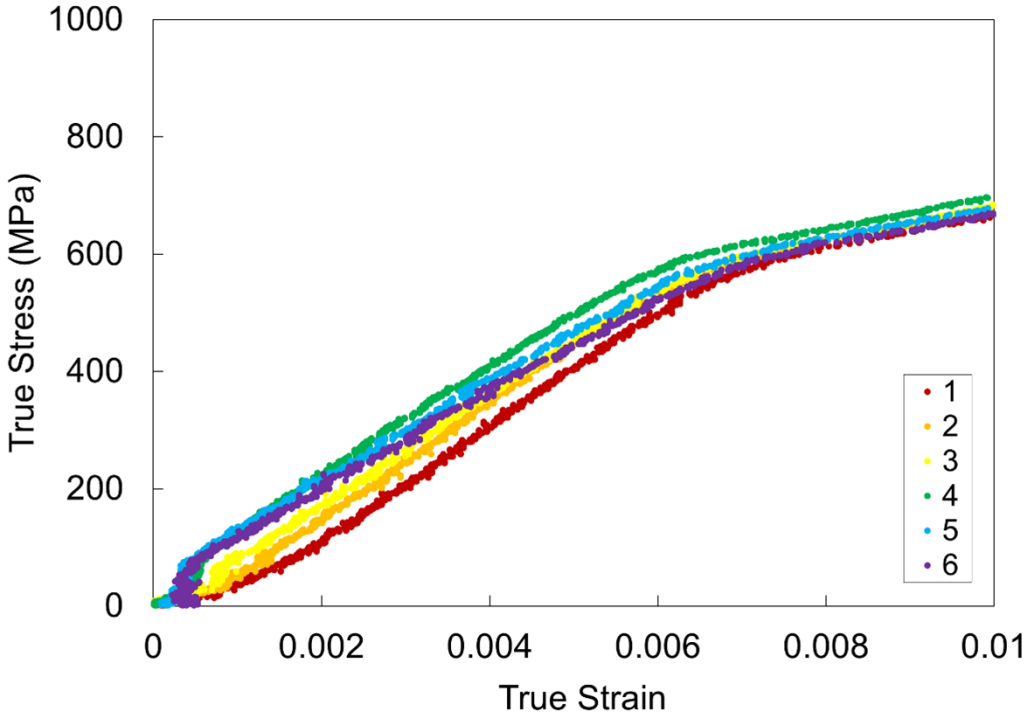

Figure 5.5: True Stress vs. True Strain graph of STAL15 ⟨001⟩ at 825 °C.

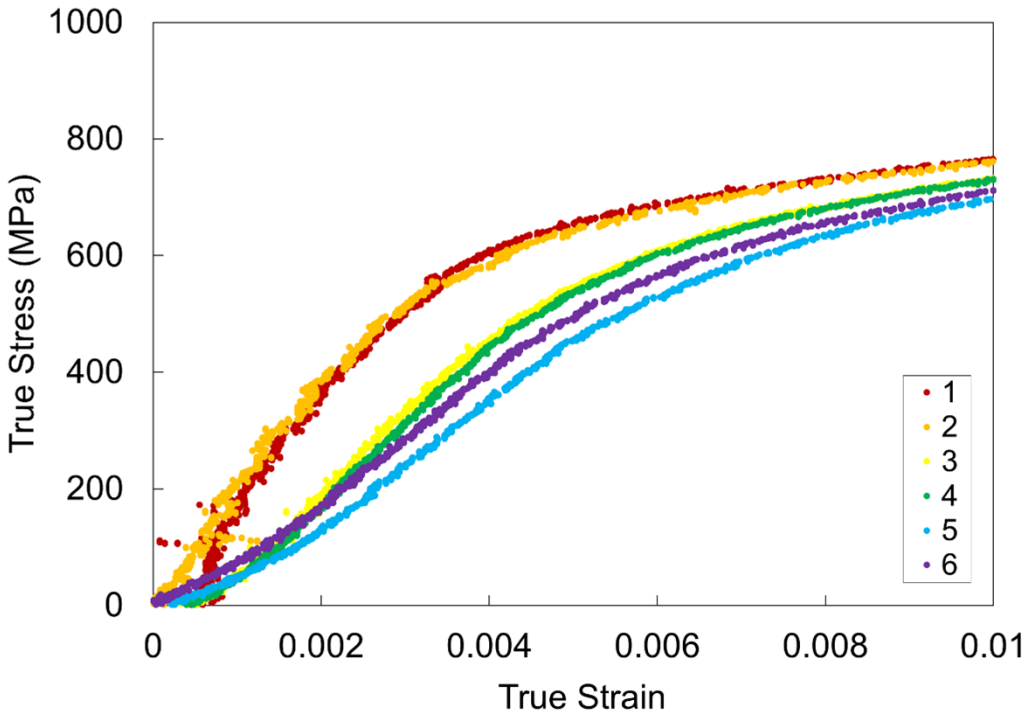

Figure 5.6: True Stress vs. True Strain graph of STAL15 ⟨011⟩ at 825 °C.

The elastic modulus obtained from the true stress vs. true strain curves of STAL15 at 825 °C for the ⟨001⟩ and ⟨011⟩ orientations exhibited notable variations compared to the results obtained at 675 °C (see Figure 5.4). The change in elastic modulus at the higher temperature highlighted the material's sensitivity to temperature and crystallographic orientation. In order to determine the elastic modulus value, linear regression analysis was performed using data points within the stress range of 100 to 500 MPa. Table 5.4 below shows the values.

Table 5.4: Elastic moduli calculated from different regions of the STAL15 ⟨001⟩ and ⟨011⟩ samples.

Camera #	1	2	3	4	5	6	Mean
E (GPa) ⟨001⟩	98.3	98.5	93.1	93.4	84.5	81.5	91.6
E (GPa) ⟨011⟩	172.5	172.6	135.9	133.9	107.7	111.4	139

Upon analysing the experimental data, the following percentage differences were determined: For STAL15 ⟨001⟩, the percentage difference was found to be 18.89%, while for the much more anisotropic STAL15 ⟨011⟩, the percentage difference was found to be 46.33%. These results reveal distinct variations in the mechanical behaviour of the material along different crystallographic orientations and temperatures, and provide valuable insights into its anisotropic response.

5.3.1.3 Strain Rates of 10^{-3} s^{-1}, 10^{-2} s^{-1}, 10^{-1} s^{-1}

The effect of strain rate on the mechanical behaviour of STAL15 ⟨011⟩ was also examined at 825 °C by conducting tensile tests at different strain rates. Three distinct strain rates, namely 10^{-3} s^{-1}, 10^{-2} s^{-1} and 10^{-1} s^{-1}, were selected for the experiments. The tests were performed using the same experimental setup and temperature conditions to ensure consistency.

The stress-strain curves obtained at each strain rate allowed for the determination

of the elastic modulus for STAL15 ⟨011⟩. The elastic modulus values were subsequently compared to investigate how the material's response to applied loads varied with changing strain rates. By systematically varying the strain rates of STAL15 ⟨011⟩, we aimed to gain insights into the strain rate sensitivity of the material's elastic properties. True stress vs. true strain graphs of the mentioned conditions are given in Figure 5.7 and Figure 5.8 below.

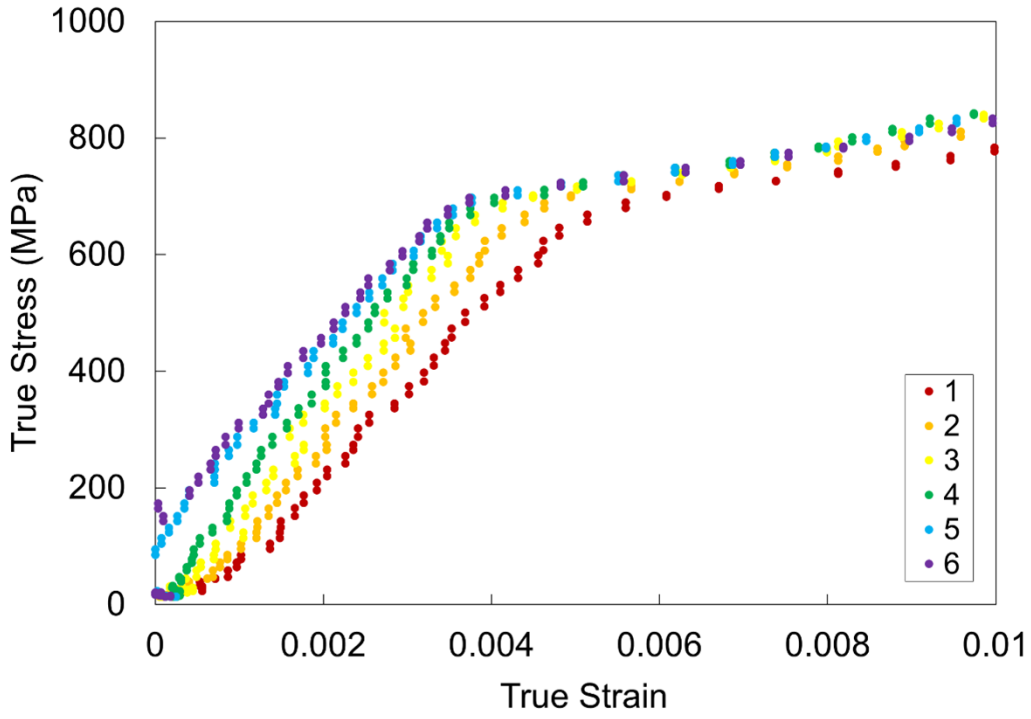

Figure 5.7: True Stress vs. True Strain graph of STAL15 ⟨011⟩ at 10^{-2} s^{-1}.

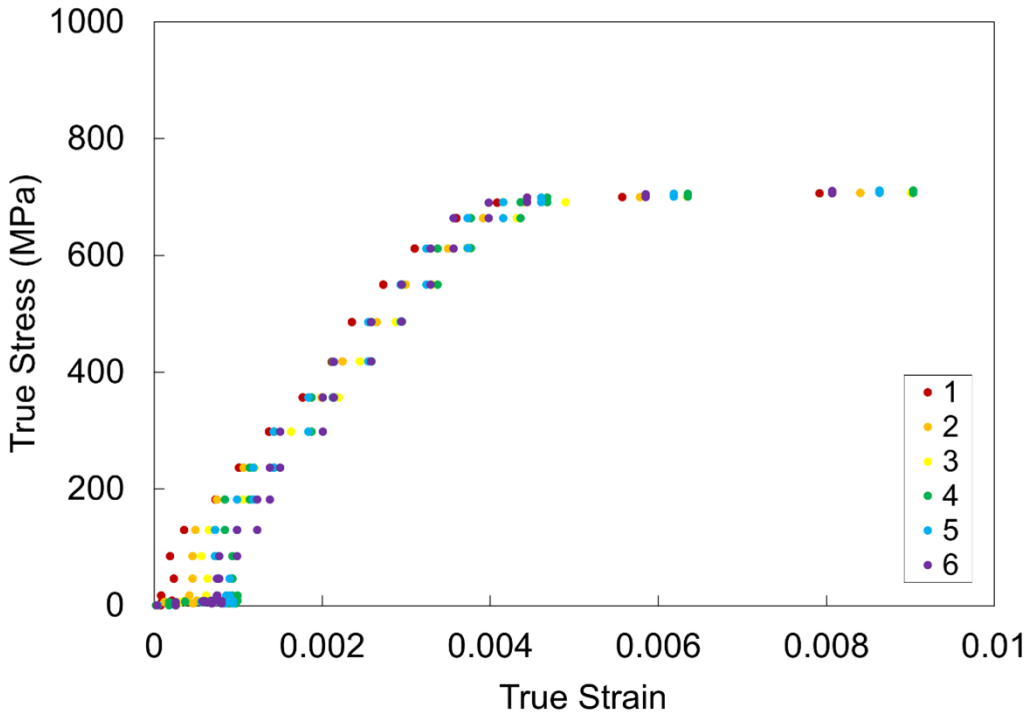

Figure 5.8: True Stress vs. True Strain graph of STAL15 ⟨011⟩ at 10^{-1} s^{-1}.

As was previously stated, the percentage difference in the elastic modulus of STAL15 ⟨011⟩ at 825 °C and at a strain rate of 10^{-3} s^{-1} is 46.33%. At a higher strain rate of 10^{-2} s^{-1}, the percentage difference in the elastic modulus was found to be 17.28%. At the highest strain rate of 10^{-1} s^{-1}, the percentage difference in the elastic modulus was measured to be 24.79%. The linear regression analysis which was used to get the results above was performed using data points within the stress range of 100 to 500 MPa. See Table 5.5 below.

Table 5.5: Elastic moduli calculated from different regions of the STAL15 ⟨011⟩ samples at various strain rates.

Camera #	1	2	3	4	5	6	Mean
E (GPa) 10^{-3} s^{-1}	172.5	172.6	135.9	133.9	107.7	111.4	139
E (GPa) 10^{-2} s^{-1}	159.2	176.4	181.7	189.3	166.2	160.5	172.2
E (GPa) 10^{-1} s^{-1}	176.3	161.0	157.3	171.2	179.9	201.7	174.6

5.3.1.4 Temperatures of 825 °C, 850 °C, 875 °C, 900 °C

The effect of temperature was also examined at a strain rate of 10^{-1} s^{-1}, on the mechanical behaviour of STAL15 ⟨011⟩. Four different temperatures, namely 825 °C, 850 °C, 875 °C and 900 °C were tested and true stress vs. true strain results are presented in Figures 5.9, 5.10 and 5.11 below. These experimental tests were conducted to discern the material's response to varying thermal conditions, providing valuable insights into its temperature-dependent mechanical properties.

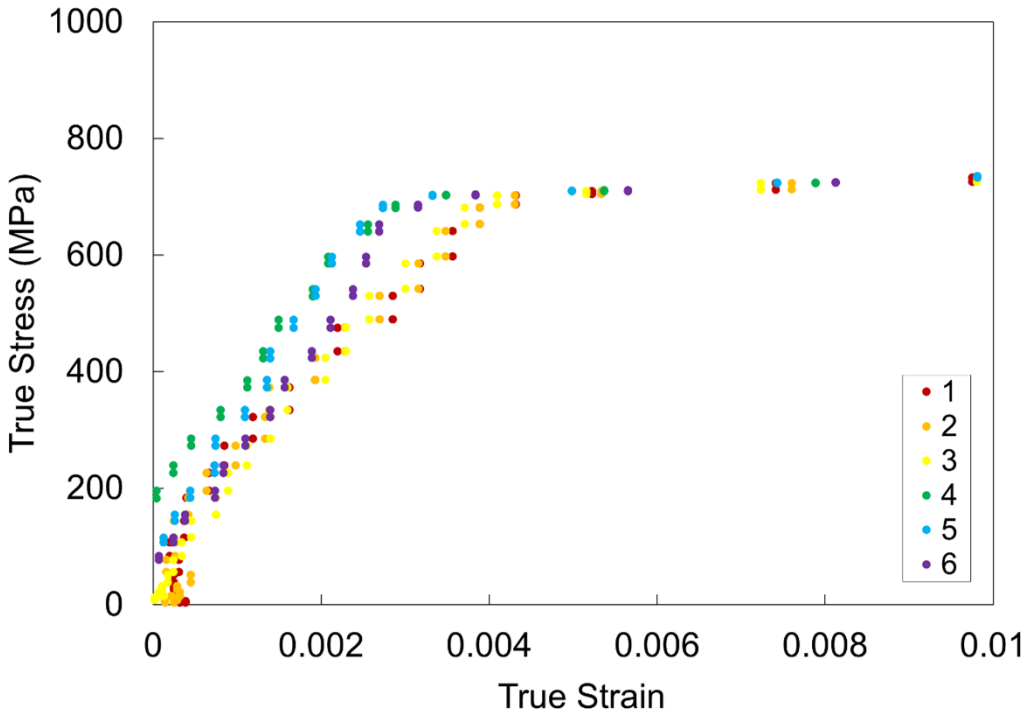

Figure 5.9: True Stress vs. True Strain graph of STAL15 ⟨011⟩ at 850 °C.

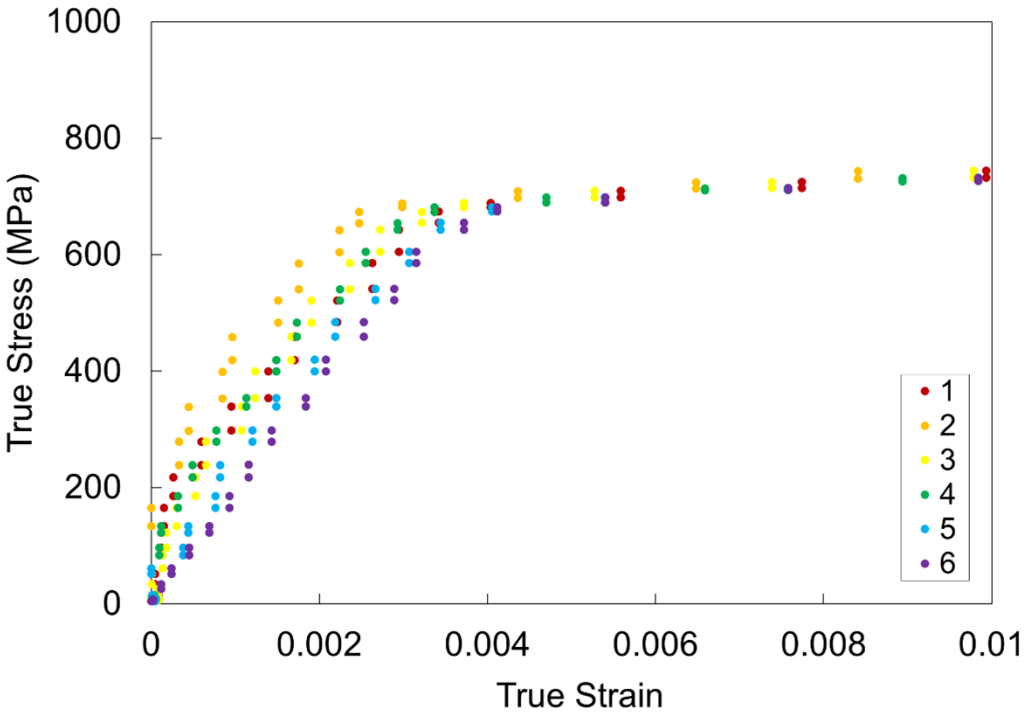

Figure 5.10: True Stress vs. True Strain graph of STAL15 ⟨011⟩ at 875 °C.

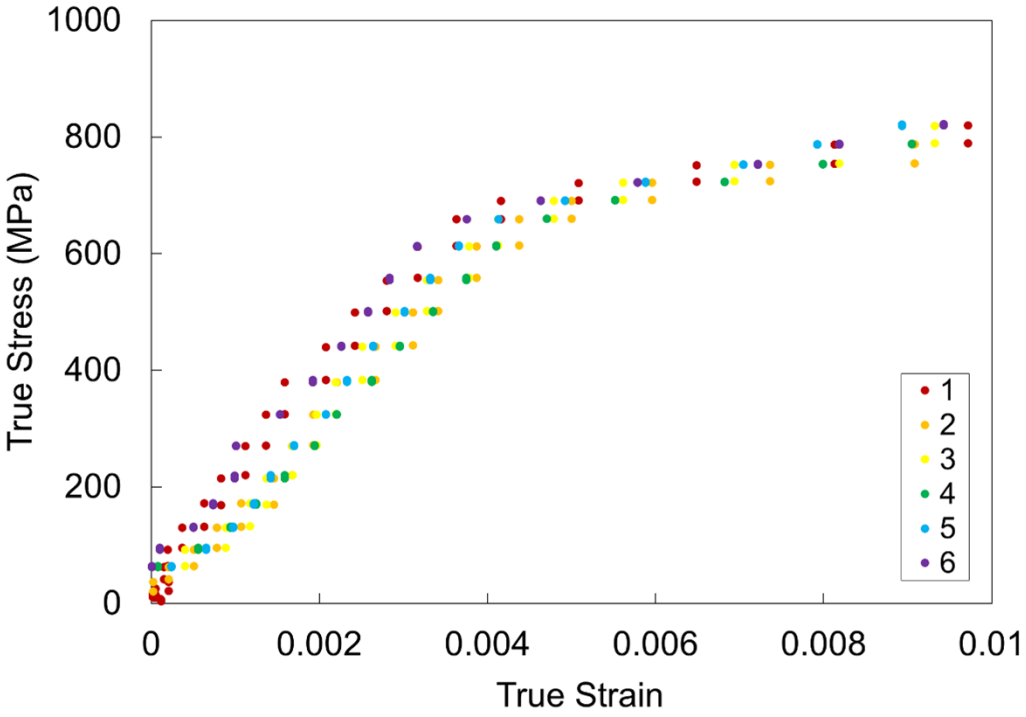

Figure 5.11: True Stress vs. True Strain graph of STAL15 ⟨011⟩ at 900 °C.

As previously stated, the percentage difference in the elastic modulus of STAL15 ⟨011⟩ at a strain rate of 10^{-1} s^{-1} at 825 °C is 24.79%. Additionally, at a higher temperature of 850 °C, the percentage difference in the elastic modulus was found to be 42.01%. At 875 °C, the percentage difference in the elastic modulus was measured to be 23.18%, and at the highest temperature of 900 °C, the percentage difference in the elastic modulus was measured to be 17.94%. The linear regression analysis, which was employed to derive these results, was performed using data points within the stress range of 100 to 500 MPa. Elastic modulus test results are shown in Table 5.6 below.

Table 5.6: Elastic moduli calculated from different regions of the STAL15 ⟨011⟩ samples at various temperatures.

Camera #	1	2	3	4	5	6	Mean
E (GPa) 825 °C	176.3	161.0	157.3	171.2	179.9	201.7	174.6
E (GPa) 850 °C	152.1	156.8	178.9	197.2	232.9	195.9	185.6
E (GPa) 875 °C	176.5	222.8	215.7	210.3	195.9	188.2	201.7
E (GPa) 900 °C	173.7	160.5	181.7	151.8	179.6	170.6	169.7

5.3.2 Optical Profilometry

Optical 3D profilometry was performed on the tested STAL15 ⟨011⟩ samples using an Alicona Infinite Focus 3D Profilometer to analyse the fractured surfaces of the specimens after completing the tensile tests. This advanced instrument utilises non-contact optical techniques to precisely create the 3D image and capture the topographical features of the fractured surfaces.

During the optical profilometry process, high-resolution optical sensors and advanced imaging algorithms were employed to scan the surfaces and collect detailed height information. The vertical and lateral resolutions of the profilometer were both

adjusted to be 6 μm; as this resolution optimised sufficient image quality with feasible scanning speed, enabling surface differences to be distinguished.

Fracture surface analysis was done on a total of 12 STAL15 ⟨011⟩ samples, ruptured at temperatures of 825 °C, 850 °C, 875 °C and 900 °C. At each temperature, tests at strain rates of 10^{-3} s^{-1}, 10^{-2} s^{-1} and 10^{-1} s^{-1} were made (see Figure 5.12 below).

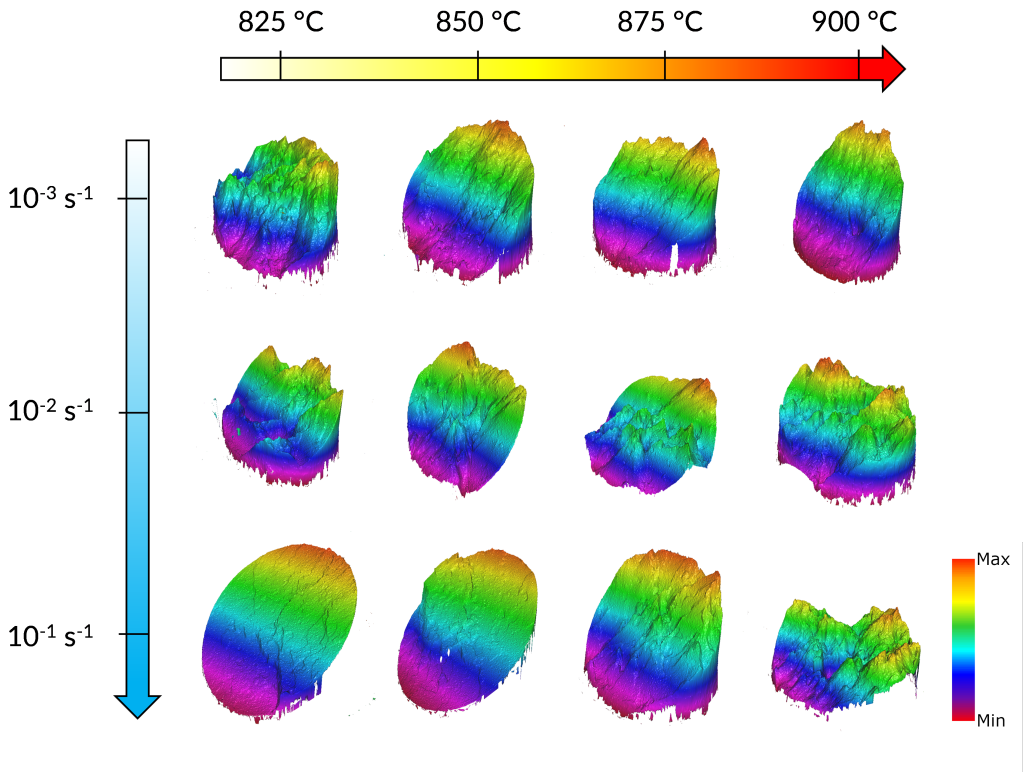

Figure 5.12: 3D fracture surfaces of STAL15 ⟨011⟩ samples, deformed in tension at various temperatures and strain rates. The images use a rainbow colour convention for height representation, as seen from the legend on the bottom-right corner of the figure. While the colour-coding scheme is uniform, the specific height range varies between images, with unique minimum and maximum values for each. Scale is the same for all images.

To gain a deeper insight into the effect of anisotropy on the material's behaviour and to better understand the extent of deformation anisotropy and its influence on the fracture characteristics, aspect ratios of the fracture surfaces were also calculated (see Figure 5.13). As mentioned in the Methods section, the aspect ratio is calculated

by dividing the shortest diameter by the longest diameter, as seen from the top view of the ruptured sample. Notice how the aspect ratio of the 10^{-1} s^{-1} sample drops instantly as the temperature is increased from 850 °C to 875 °C.

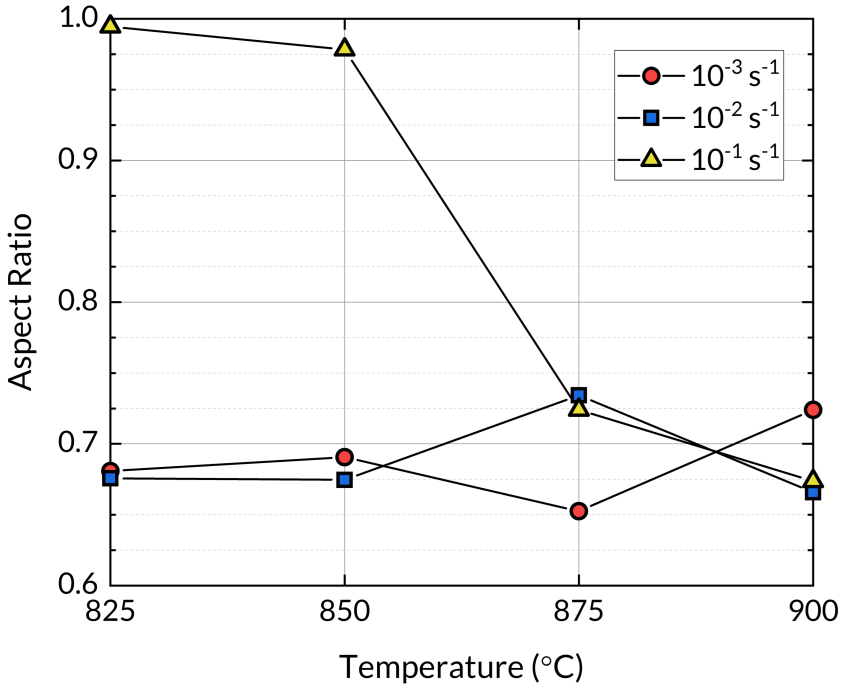

Figure 5.13: Aspect ratio vs. temperature (°C) graphs for varying strain rates.

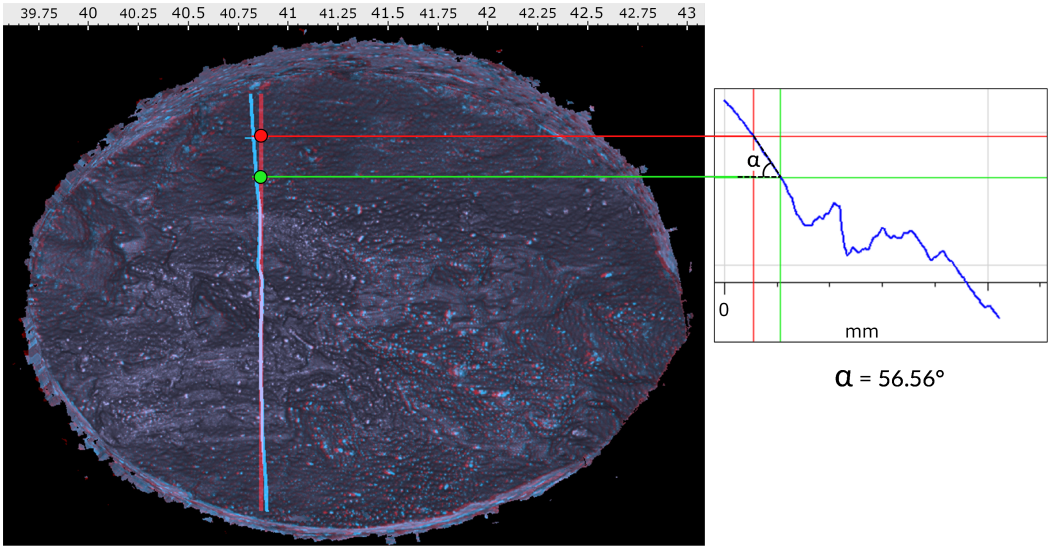

Figure 5.14: Method of calculating the slope angles of the slip planes and how the angle is defined. Note that only the angles of the slip planes were calculated. The image on the left is an anaglyph stereogram and can be viewed in 3D using red-blue glasses.

The maximum and minimum slope angles of the fracture surface slip planes were also calculated, using the method shown in Figure 5.14. The slip planes seem to break/divide and reduce in size as the temperature is increased, suggesting a change in deformation mechanisms. After a temperature of 825 °C and a strain rate of 10^{-3} s^{-1}, the slip planes almost seemed to dissappear altogether hence they were not calculated. The slope angles of the resultant slip planes are given in Table 5.7 below.

Table 5.7: Minimum and maximum slope angles of the fracture surface slip planes of STAL15 ⟨011⟩ samples at various temperatures and strain rates.

Temperature (°C)	825	850	875	900
10^{-3} s^{-1}	63-66°	-	-	-
10^{-2} s^{-1}	43-57°	55-59°	51-63°	49-64°
10^{-1} s^{-1}	35-37°	34-36°	48-60°	61-70°

5.4 Discussion

5.4.1 Mechanical Testing

5.4.1.1 AD730 vs. STAL15 ⟨001⟩

The tensile tests conducted on AD730 and STAL15 ⟨001⟩ at a temperature of 675 °C and a strain rate of 10^{-3} s^{-1} provided valuable insights into the effect of crystal structure on the materials' mechanical behaviour. The consistent behaviour observed in the true stress vs. true strain curves of AD730 aligns with its isotropic nature, where the mechanical properties remain almost unaffected by the digital extensometer location, as the percentage difference (which can be interpreted as the degree of anisotropy) between the maximum and minimum recorded elastic modulus values were calculated to be approximately 11.38%.

In contrast to this, the percentage difference between the maximum and minimum recorded elastic modulus values for STAL15 ⟨001⟩ was calculated to be approximately 30.47%, almost 3 times higher than that of AD730. This substantial variation in the percentage difference was initially attributed to the strong anisotropic nature of single crystals. However, anisotropy in this case is not entirely expected, as the principal orientation remains the same. The observed anisotropy may be influenced by the secondary orientation of the surface normal, as measurements were taken at different positions. The true stress vs. true strain readings obtained from the elastic region of STAL15 ⟨001⟩ also displayed intriguing non-linear responses with curved lines. The notable deviation from the expected linear behaviour seen in conventional elastic materials highlights the sensitivity of anisotropic materials to the direction of loading, making the use of multiple digital extensometer locations a critical factor in determining its mechanical properties.

Another important aspect to consider is the measurement consistency of the digital extensometers, when comparing data between different cameras. Specifically, digital

extensometers 3 (yellow) and 4 (green) were strategically positioned to measure data from the same location on the sample, albeit using different cameras. The results from these extensometers exhibited close agreement for both experiments, highlighting the consistency and reliability of our measurement techniques.

Additionally, the true stress vs. true strain curves of AD730 indicate minor misalignment issues in the load train, potentially affecting the early parts of the measurements and leading to observable spacing between curves generated by different digital extensometers. Although misalignments tend to stabilise under the influence of high tensile forces as the test progresses, they introduce initial discrepancies that complicate the interpretation of data.

In terms of the tensile tests done on the single-crystal STAL15 $\langle 001 \rangle$, the discrepancies between the red and the purple curves cannot be attributed to elastic anisotropy, as the crystallographic orientations are the same for both curves. It is more likely that these differences are due to bending, given that the curves correspond to measurements on opposite sides of the specimen. The non-linear behavior observed prior to yield is most likely due to plasticity occurring within the gamma phase before the macroscopic yield, when dislocations begin to penetrate the gamma prime phase. The strain rate and temperature dependence of the anisotropy measurements strongly suggest that plasticity, rather than elastic effects, plays the dominant role in causing these variations.

5.4.1.2 STAL15 $\langle 001 \rangle$ vs. STAL15 $\langle 011 \rangle$

The investigation into the effect of crystal orientation on STAL15 also revealed significant variations in the elastic modulus at an elevated temperature of 825 °C and a strain rate of 10^{-3} s^{-1}. The experiments involved testing the material in two different crystallographic orientations, $\langle 001 \rangle$ and $\langle 011 \rangle$. For STAL15 $\langle 001 \rangle$, the percentage difference in the elastic modulus was found to be 18.89%, while for the much

more anisotropic STAL15 ⟨011⟩, the percentage difference was significantly higher at 46.33%, almost 2.5 times that of ⟨001⟩. Such high variability in the elastic modulus, especially for the ⟨011⟩ crystal orientation, suggests that without employing multiple cameras and digital extensometer locations, it is very difficult to get an accurate elastic modulus value.

One other point to note is the response of STAL15 ⟨001⟩ to the increase in temperature from 675 °C to 825 °C at strain rate of 10^{-3} s^{-1}. The percentage difference in the elastic modulus of STAL15 ⟨001⟩ decreased from 30.47% at 675 °C to 18.89% at 825 °C, indicating a reduction in anisotropic behaviour with increasing temperature. The diminishing percentage difference suggests a more isotropic mechanical response in STAL15 ⟨001⟩ at elevated temperatures, implying that the material's mechanical properties become less directionally dependent as the temperature increases. However, it is essential to perform experiments at additional temperature levels before reaching any conclusive statements regarding the complete temperature-dependent behaviour of the material.

5.4.1.3 Strain Rates of 10^{-3} s^{-1}, 10^{-2} s^{-1}, 10^{-1} s^{-1}

The study on the impact of strain rate on STAL15 ⟨011⟩ at 825 °C also revealed interesting findings. Tensile tests were conducted at three different strain rates (10^{-3} s^{-1}, 10^{-2} s^{-1}, and 10^{-1} s^{-1}) to assess the material's response to varying loading conditions. The true stress vs. true strain curves obtained allowed us to determine the elastic modulus for each strain rate and explore how the material's mechanical properties changed with different strain rates. The elastic modulus of STAL15 ⟨011⟩ showed significant strain rate sensitivity, exhibiting the highest percentage difference at the lowest strain rate: 46.33% at 10^{-3} s^{-1}, 17.28% at 10^{-2} s^{-1}, and 24.79% at 10^{-1} s^{-1}. These results reveal a noticeable increase in anisotropy at lower strain rates. The mean elastic modulus values also show strain rate dependence up to a point: 139 GPa

at the slowest strain rate of 10^{-3} s^{-1}, 172.2 GPa at 10^{-2} s^{-1}, and 174.6 GPa at 10^{-1} s^{-1}. These results might suggest that the elastic modulus increases with higher strain rates, up to a certain limit. Beyond this limit, the elastic modulus remains relatively constant, indicating a critical strain rate. More tests at different strain rates may help to establish whether or not there is a significant pattern between strain rate and degree of anisotropy.

5.4.1.4 Temperatures of 825 °C, 850 °C, 875 °C, 900 °C

The last set of mechanical tests were done to investigate the effect of temperature on the mechanical behaviour of STAL15 $\langle 011 \rangle$ at a strain rate of 10^{-1} s^{-1}. By conducting tensile tests at four different temperatures (825 °C, 850 °C, 875 °C, and 900 °C), we aimed to explore the temperature-dependent mechanical properties of the material. The choice of a strain rate of 10^{-1} s^{-1} for the mechanical tests at the mentioned temperatures was influenced by intriguing observations from the optical profilometer results of the fracture surfaces. At the lower temperatures of 825 °C and 850 °C, the fracture surface exhibited a mainly single slip-plane morphology, indicating a more uniform and continuous deformation behaviour. However, as the temperature increased to 875 °C, the fracture surface transformed into a complex arrangement of multiple planes. This transition in fracture surface morphology suggests a change in the material's deformation mechanisms and response to external loads at higher temperatures. By selecting a strain rate of 10^{-1} s^{-1}, we aimed to capture and explore these notable changes in the mechanical behaviour of the material at elevated temperatures, enabling a deeper understanding of its response to varying thermal conditions. At 825 °C, the percentage difference in the elastic modulus was 24.79%, increasing significantly to 42.01% at 850 °C, indicating an increase in the anisotropic response of the material. However, at 875 °C, the percentage difference decreased to 23.18%, and at 900 °C, it further decreased to 17.94%, indicating that anisotropy be-

came less prominent at the point where the deformation mechanisms start to change. More tests at different temperatures may help to establish whether or not there is a significant pattern between temperature and degree of anisotropy and where the true peak of anisotropy lies.

During our experiments, digital extensometers 3 (yellow) and 4 (green) generally showed good correlation. However, a noticeable discrepancy was observed at a strain rate of 10^{-1} s^{-1} and a temperature of 850 °C, as seen in Figure 5.9. This issue could stem from several factors, such as the cameras' inability to accurately capture rapid movements at high strain rates or impaired imaging quality due to excessive heat from the furnace. However, the absence of similar issues at comparable strain rates and temperatures suggests that the underlying cause might be related to the material itself rather than the experimental setup. To better understand these unexpected variations, more experiments under these conditions would need to be conducted.

5.4.2 Optical Profilometry

Up to this point, our focus has primarily been on exploring the anisotropy exhibited in the elastic region of the stress-strain curve. However, to gain deeper insights into the material's behaviour, we will now shift our attention to the plastic region. In this phase, we aim to investigate the morphology of the deformed samples instead of solely relying on comparing stress-strain curves, as the plastic region curves produced by the digital extensometers exhibit a high degree of similarity. This approach will allow us to further understand the anisotropic characteristics of plastic deformation, providing valuable information about its response to applied loads and the complex deformation patterns that arise in different crystallographic orientations. By examining the fracture surfaces of the deformed samples, we might be able to establish a connection between elastic anisotropy and plastic anisotropy, gaining a more comprehensive understanding of the material's mechanical behaviour at elevated temperatures and

varying strain rates.

Out of the 12 samples analysed using the optical profilometer, only two exhibited an aspect ratio close to unity. These particular samples were subjected to tests at a strain rate of 10^{-1} s^{-1} and temperatures of 825 °C and 850 °C. Conversely, the remaining samples displayed an aspect ratio around 0.7, indicating the presence of anisotropic deformation. Notably, the distinctive characteristic of the former two samples was their fracture surface morphology predominantly consisting of a single slip-plane. Additionally, the samples with the single slip-plane morphology exhibited the lowest slip-plane angles among the entire group. As temperature was increased or strain rate decreased, the slope angles exhibited a corresponding increase. Despite best efforts to meticulously measure the slope angles from samples exhibiting slip-plane structures, achieving a quantitative plane definition could enhance reproducibility and accuracy in characterising anisotropic deformation.

To enhance our understanding of anisotropy in the elastic region, it is essential to gather stress-strain data from all surfaces of the deforming sample. Employing a minimum of 4 cameras, positioned at equal angles to one another, would facilitate a more comprehensive observation of the sample's behaviour, provided there are no planes of symmetry that could reduce the number of required angles to cover. Additionally, utilising square cross-section samples brings several advantages over circular cross-section samples: it minimises projection distortion when generating 3D visualisations from the 2D DIC strain maps; enables better control and alignment of crystallographic orientations, leading to clearer observations of anisotropic effects along specific directions; simplifies data analysis and visualisation due to the symmetry of the cross-section. Ensuring consistent camera focus across the entire sample area by focusing on each surface and aligning the main crystal orientations perpendicular to the surfaces during sample cutting would further improve visualisation of the anisotropic response, providing valuable insights for future investigations. These

enhancements offer a more comprehensive understanding of the anisotropic behaviour in the elastic region of the tested materials and contribute to the development of more accurate and reliable characterisation techniques.

Including compression testing in the multi-camera configuration could offer a more comprehensive understanding of anisotropic responses from the same materials, complementing the insights gained from tensile testing and providing a more holistic characterisation of their properties.

5.5 Conclusions

This study aims to understand the anisotropic behaviour of Ni-based single-crystal superalloys through a comprehensive investigation encompassing comparative tests for crystal structure, crystal orientation, strain rate, and temperature. By conducting extensive mechanical tests and utilising optical profilometry, we sought to gain deeper insights into the mechanical response of these materials. The main findings of this chapter are:

- When comparing the effect of crystal structure, measuring the elastic modulus and stress-strain curves of polycrystalline samples is a more straightforward process compared to single crystals. The results obtained from polycrystalline samples exhibit a higher level of agreement, making them more trustworthy than results obtained from single crystal samples. Therefore, obtaining measurements of the elastic modulus and stress-strain curves for single crystal samples requires more points of measurement (more digital extensometers at different locations) to better characterise the material in terms of mechanical properties.

- Comparison of crystal orientations by measuring elastic modulus and stress-strain curves also yielded values that vary depending on the extensometer position around the specimen. The $\langle 011 \rangle$ orientation exhibited higher anisotropy

compared to $\langle 001 \rangle$, leading to lower agreement and reliability in measurements. Thus, as before, more points of measurement are required for the material with the higher degree of anisotropy.

- The effect of strain rate and temperature on anisotropy with $\langle 011 \rangle$ was not as clear. The lowest strain rate did indeed give the highest degree of anisotropy, however, there was not a clear trend at higher strain rates. In terms of temperature, the peak degree of anisotropy was at 850 °C but no clear trend could be established with the datapoints obtained. Given these results, there seems to be no direct link between strain rate nor temperature with degree of anisotropy. This means there was not a condition found where an anisotropic material like $\langle 011 \rangle$ was found to behave less anisotropically (which may reduce the number of measurements needed as aforementioned).

- Alterations in strain rate and temperature did appear to impact the slip-plane angles obtained from the optical profilometry results. As strain rates decreased and temperatures increased, the slope angles of the slip-planes tended to increase. This phenomenon might be attributed to the onset of creep deformation at higher temperatures and prolonged experiment durations.

- Anisotropy in the elastic region of a strain curve does not guarantee anisotropy in the morphology of tested specimens. Further investigation is required to establish a link between these characteristics, which could potentially enable us to predict fracture patterns by examining the elastic region of the stress-strain curves.

Chapter 6

Conclusions and Future Work

6.1 Conclusions

The primary goal of this study was to advance the understanding of anisotropic mechanical behaviour in Ni-based single-crystal superalloys, focusing on the STAL15 alloy across two primary crystallographic orientations, namely ⟨001⟩ and ⟨011⟩. This study explored how variations in temperature and strain rate impacts the mechanical properties of these alloys, aiming to provide insights into their performance and behaviour under different operational conditions.

Chapter 3 compared the mechanical responses of the ⟨001⟩ and ⟨011⟩ crystallographic orientations under varying temperatures and strain rates. Key findings indicated that at lower temperatures, the ⟨001⟩ orientation exhibits stage I hardening, whereas the ⟨011⟩ orientation tends to soften. Initially, as temperatures increase, both orientations experience a decrease in yield strength (0.2% offset). This is followed by an increase in yield strength until a critical temperature of 725 °C for ⟨001⟩ and 800 °C for ⟨011⟩, beyond which a sharp decline is observed. Notably, the yield strength of ⟨011⟩ surpasses that of ⟨001⟩ after 800 °C. The elastic modulus determination in the ⟨011⟩ orientation is more challenging due to its higher anisotropy, yet it generally shows a higher modulus compared to ⟨001⟩. The transition from stage I to

stage II hardening is delayed at higher strain rates. Both temperature increases and strain rate decreases lead to a shift from stage I to stage II hardening starting right after yield, with stage II hardening curves becoming steeper after these changes.

In Chapter 4, the exploration into the anomalous yield phenomenon challenged traditional interpretations, suggesting that the presence of anomalous yield strongly depends on the definition of yield strength. Higher offset definitions (0.2% and 0.1%) suggested an increase in yield strength as temperatures rose, indicating the presence of a yield anomaly. However, when using definitions closer to the elastic deformation line (0.01% and proportional limit), the results did not support the presence of this anomaly, suggesting that the perceived yield anomaly in these materials may not indicate actual material strengthening with temperature, but rather the retention of strength. This chapter also highlighted that yield strength values defined at higher offsets are significantly influenced by the development of the plastic region in stress-strain curves as temperatures increased. Determining the most appropriate yield strength definition involves balancing accurate material behaviour with practical measurement considerations, with the 0.01% offset yield strength definition striking this balance most effectively.

Chapter 5 analyses the anisotropic behaviour of Ni-based single-crystal superalloys, through comparative tests for crystal structure, crystal orientation, strain rate, and temperature. The findings reveal that polycrystalline samples yield more consistent elastic modulus and stress-strain curve measurements compared to their single crystal counterparts. Single crystals display significant variability, particularly in the $\langle 011 \rangle$ orientation which exhibits higher anisotropy than $\langle 001 \rangle$. This variability necessitates the use of multiple measurement points to accurately characterise their mechanical properties. Furthermore, while the lowest strain rate tested showed the highest degree of anisotropy, no clear trends emerged at higher strain rates or across varying temperatures, indicating that neither factor directly affects anisotropy. Ad-

justments in strain rate and temperature influenced the angles of slip planes, suggesting possible creep deformation under these conditions. Finally, although anisotropy is detectable in the elastic region of stress-strain curves, it does not consistently predict the morphological behaviour of tested specimens. Further investigation is needed to determine if there is a link between these characteristics, and to predict fracture patterns based on elastic properties.

In summary, this research provides us a strong dataset of the mechanical behaviour of Ni-based single-crystal superalloys, particularly the STAL15 alloy in $\langle 001 \rangle$ and $\langle 011 \rangle$ orientations. The findings underscore the significance of accurately defining yield strength and highlight the complexity of anisotropic behaviour.

6.2 Future Work

The findings of this thesis have identified several key areas for further research, which include:

6.2.1 Exploration of the $\langle 111 \rangle$ Crystallographic Orientation

Our research did not include testing the $\langle 111 \rangle$ crystallographic orientation, which is known to have the highest elastic modulus among the main crystal orientations. An experimental campaign which includes this orientation would provide a comprehensive comparison and enhance our understanding of its unique properties relative to the $\langle 001 \rangle$ and $\langle 011 \rangle$ orientations studied.

6.2.2 Interrupted Testing Around Yield Region

To address the complexities when defining yield strength, future work should include interrupted testing and Transmission Electron Microscopy (TEM) studies around the yield region. This approach will help us quantify deformation occurring before yield

and more clearly identify when it starts. Such insights could help explain the non-linear elastic lines observed and help us in establishing a more scientific definition of yield.

6.2.3 Optimizing Geometry for Anisotropy Analysis

Modifying the sample geometry to have a square cross-section, with the secondary orientations of the material aligned normal to each of the four rectangular surfaces and also normal to the cameras, would enhance visibility of strain localisations and material bending. The flat surfaces of the sample will also improve depth of focus across the entire DIC area, resulting in a more detailed and clear observation.

6.2.4 Development of Accurate Models

The integration of modelling techniques to replicate experimental results could provide invaluable insights into the theory of the observed behaviours. Future models should also accurately represent the experimental setup, including considerations for the slight rotations in tensile force directions due to material bending from anisotropy.

Bibliography

[1] Roger C. Reed. *The Superalloys: Fundamentals and Applications*. Cambridge University Press, 2006.

[2] Daniel Barba Cancho. *Segregation-assisted creep in nickel-based superalloys: experiments, theory and modelling*. PhD thesis, University of Oxford, 2017.

[3] Roger C. Reed and C.M.F. Rae. Physical metallurgy of the nickel-based superalloys. In *Physical metallurgy*, pages 2215–2290. Elsevier, 2014.

[4] R. G. Davies P. Beardmore and T. L. Johnston. On the temperature dependence of the flow stress of nickel-base alloys. *Transactions of the Metallurgical Society of AIME*, 245:1537–1545, 1969.

[5] AJ Goodfellow. Strengthening mechanisms in polycrystalline nickel-based superalloys. *Materials Science and Technology*, 34(15):1793–1808, 2018.

[6] A. Bezold, N. Volz, M. Lenz, C.H. Zenk, E. Spiecker, M. Mills, M. Göken, and S. Neumeier. Yielding behavior of a single-crystalline γ'-strengthened Co-Ti-Cr superalloy. *Scripta Materialia*, 200:113928, 2021.

[7] B.J. Piearcey, B.H. Kear, and R.W. Smashey. Correlation of structure with properties in a directionally solidified nickel-base superalloy. *ASM Trans Quart*, 60(4):634–645, 1967.

[8] Liberty Wu, Toshio Osada, Tadaharu Yokokawa, Yaling Chang, and Kyoko Kawagishi. The temperature dependence of strengthening mechanisms in ni-based superalloys: A newly re-defined cuboidal model and its implications for strength design. *Journal of Alloys and Compounds*, 931:167508, 2023.

[9] X.G. Wang, J.L. Liu, T. Jin, and X.F. Sun. Tensile behaviors and deformation mechanisms of a nickel-base single crystal superalloy at different temperatures. *Materials Science and Engineering: A*, 598:154–161, 2014.

[10] H.K.D.H. Bhadeshia. Slip in CCP Metals. https://www.doitpoms.ac.uk/tlplib/slip/slip_in_ccp.php. Accessed: 2023-08-19.

[11] J.-F. Croteau, E. Pai Kulyadi, C. Kale, D. Siu, D. Kang, A.T. Perez Fontenla, E. García-Tabarés Valdivieso, T.R. Bieler, P. Eisenlohr, K.N. Solanki, D. Balint, P.A. Hooper, S. Atieh, N. Jacques, and E. Cantergiani. Effect of strain rate on tensile mechanical properties of high-purity niobium single crystals for srf applications. *Materials Science and Engineering: A*, 797:140258, 2020.

[12] Hojun Lim, Philip J. Noell, and Jay D. Carroll. Crystallographic orientation dependent fracture behavior in tantalum single crystals. *Scripta Materialia*, 191:76–80, 2021.

[13] Jay D. Carroll, Hojun Lim, Matthew Lane, Corbett Battaile, Brad Boyce, Philip Noell. Crystallographic Rotation and Deformation in Tantalum. https://www.osti.gov/servlets/purl/1524822. Accessed: 2023-08-15.

[14] Weidong Xuan, Xiangyu Zhang, Yujuan Zhao, Junjie Li, Baojun Wang, Xingfu Ren, and Zhongming Ren. Mechanism of improved intermediate temperature plasticity of nickel-base single crystal superalloy with hot isostatic pressing. *Journal of Materials Research and Technology*, 14:1609–1617, 2021.

[15] S.M.C. van Bohemen and H.K.D.H. Bhadeshia. Ductile Fracture. http://www.phase-trans.msm.cam.ac.uk/2008/weld/weld-Pages/Image5.html. Accessed: 2023-08-14.

[16] William T Becker, Roch J Shipley, et al. Failure analysis and prevention. *(No Title)*, 2002.

[17] Wan-peng Yang, Jia-rong Li, Shi-zhong Liu, Zhen-xue Shi, Jin-qian Zhao, and Xiao-guang Wang. Orientation dependence of transverse tensile properties of nickel-based third generation single crystal superalloy DD9 from 760 to 1100 °C. *Transactions of Nonferrous Metals Society of China*, 29(3):558–568, 2019.

[18] JP Wang, ZX Wen, JW Liang, and ZF Yue. Typical characteristics for creep fracture cleavage plane of nickel-based single crystal. *Materials Science and Engineering: A*, 760:141–151, 2019.

[19] Frederick John Humphreys and Max Hatherly. *Recrystallization and related annealing phenomena*. elsevier, 2012.

[20] Aubert & Duval. AD730 - New Ni-based Superalloy for High Temperature Applications. https://www.aubertduval.com/wp-media/uploads/2017/05/2017_Brochure_AD730.pdf. Accessed: 2023-09-04.

[21] Rolls-Royce plc. *The Jet Engine*. John Wiley & Sons, 2015.

[22] CMF Rae, N Matan, and RC Reed. The role of stacking fault shear in the primary creep of [001]-oriented single crystal superalloys at 750 °C and 750 MPa. *Materials Science and Engineering: A*, 300(1-2):125–134, 2001.

[23] Jinghua Zhang, JIN Tao, XU Yongbo, HU Zhuangqi, and WU Xin. Antiphase boundary strengthening in a single crystal nickel-base superalloy. *Journal of Materials Sciences and Technology*, 18(02):159–162, 2009.

[24] GB Viswanathan, PM Sarosi, MF Henry, DD Whitis, WW Milligan, and MJ Mills. Investigation of creep deformation mechanisms at intermediate temperatures in René 88 DT. *Acta Materialia*, 53(10):3041–3057, 2005.

[25] Alberto C Picasso, Angel J Marzocca, and Iris Alvarez. Cross-slip and dislocation climb in nickel-base superalloys. *Materials Science and Engineering: A*, 234:1099–1102, 1997.

[26] Timothy M Smith, Raymond R Unocic, Hallee Deutchman, and Michael J Mills. Creep deformation mechanism mapping in nickel base disk superalloys. *Materials at High Temperatures*, 33(4-5):372–383, 2016.

[27] GB Viswanathan, S Karthikeyan, Peter M Sarosi, RR Unocic, and MJ Mills. Microtwinning during intermediate temperature creep of polycrystalline ni-based superalloys: mechanisms and modelling. *Philosophical Magazine*, 86(29-31):4823–4840, 2006.

[28] Libor Kovarik, Raymond R Unocic, Ju Li, P Sarosi, C Shen, Yunzhi Wang, and Michael J Mills. Microtwinning and other shearing mechanisms at intermediate temperatures in ni-based superalloys. *Progress in Materials Science*, 54(6):839–873, 2009.

[29] Chester T Sims. A History of Superalloy Metallurgy for Superalloy Metallurgists. *Superalloys*, 1984:399–419, 1984.

[30] C.T. Sims, N.S. Stoloff, N.F. Stoloff, W.C. Hagel, and W.C. Hagel. *Superalloys II: High-Temperature Materials for Aerospace and Industrial Power*. A Wiley-Interscience publication. Wiley, 1987.

[31] H.K.D.H. Bhadeshia. Nickel Based Superalloys. https://www.phase-trans.msm.cam.ac.uk/2003/Superalloys/superalloys.html. Accessed: 2023-08-17.

[32] Lin Liu, Jun Zhang, and Cheng Ai. Nickel-based superalloys. In Francisca G. Caballero, editor, *Encyclopedia of Materials: Metals and Alloys*, pages 294–304. Elsevier, Oxford, 2022.

[33] V.C.I. Strutt, B.M. Jenkins, J.M. Woolrich, M. Appleton, M.P. Moody, and P.A.J. Bagot. Effect of microsegregation and heat treatment on localised γ and γ' compositions in single crystal ni-based superalloys. *Journal of Alloys and Compounds*, 949:169861, 2023.

[34] CKL Davies, PW Davies, and B Wilshire. The effect of variations in stacking-fault energy on the creep of nickel-cobalt alloys. *Philosophical Magazine*, 12(118):827–839, 1965.

[35] Pei-Ling Sun, Y.H. Zhao, J.C. Cooley, M.E. Kassner, Z. Horita, T.G. Langdon, E.J. Lavernia, and Y.T. Zhu. Effect of stacking fault energy on strength and ductility of nanostructured alloys: An evaluation with minimum solution hardening. *Materials Science and Engineering: A*, 525(1):83–86, 2009.

[36] Farghalli A Mohamed and Terence G Langdon. The transition from dislocation climb to viscous glide in creep of solid solution alloys. *Acta Metallurgica*, 22(6):779–788, 1974.

[37] Shouichi Ochial, Yoshihiro Oya, and Tomoo Suzuki. Alloying Behaviour of Ni_3Al, Ni_3Ga, Ni_3Si and Ni_3Ge. *Acta Metallurgica*, 32(2):289–298, 1984.

[38] Tresa M Pollock and Sammy Tin. Nickel-based superalloys for advanced turbine engines: Chemistry, microstructure and properties. *Journal of propulsion and power*, 22(2):361–374, 2006.

[39] Catherine MF Rae and Roger C Reed. The precipitation of topologically close-packed phases in rhenium-containing superalloys. *Acta materialia*, 49(19):4113–4125, 2001.

[40] Jack Hall Westbrook and Robert Louis Fleischer. Intermetallic compounds, principles and practice. vol. 1 and 2. *Wiley, John & Sons Ltd, Baffins Lane, Chichester, Sussex PO 19 1 UD, UK, 1994. 1900*, 1994.

[41] Hiroshi Yamagata. 6 - the valve and valve seat. In Hiroshi Yamagata, editor, *The Science and Technology of Materials in Automotive Engines*, pages 132–151. Woodhead Publishing, 2005.

[42] Alan J Ardell. Precipitation hardening. *Metallurgical Transactions A*, 16(12):2131–2165, 1985.

[43] MR Ahmadi, Erwin Povoden-Karadeniz, Lawrence Whitmore, Martin Stockinger, Ahmad Falahati, and Ernst Kozeschnik. Yield strength prediction in Ni-base alloy 718Plus based on thermo-kinetic precipitation simulation. *Materials Science and Engineering: A*, 608:114–122, 2014.

[44] RW Kozar, A Suzuki, WW Milligan, JJ Schirra, MF Savage, and TM Pollock. Strengthening mechanisms in polycrystalline multimodal nickel-base superalloys. *Metallurgical and materials transactions A*, 40(7):1588–1603, 2009.

[45] EJ Lee and AJ Ardell. Superposition of precipitation-hardening mechanisms. In *Strength of metals and alloys*, pages 633–638. Elsevier, 1979.

[46] A Melander and PA Persson. Strength of γ' hardened nickel-base alloy. *Metal Science*, 12(9):391–398, 1978.

[47] Victor A Phillips. Hardening mechanisms in a precipitation hardenable nickel-12·71 at.% aluminium alloy. *Philosophical Magazine*, 16(139):103–117, 1967.

[48] L.K. Singhal and J.W. Martin. The mechanism of tensile yield in an age-hardened steel containing γ' (ordered Ni_3Ti) precipitates. *Acta Metallurgica*, 16(7):947–953, 1968.

[49] V Gerold and H Haberkorn. On the critical resolved shear stress of solid solutions containing coherent precipitates. *physica status solidi (b)*, 16(2):675–684, 1966.

[50] RF Decker and JR Mihalisin. Coherency strains in gamma prime hardened nickel alloys. *ASM TRANS QUART*, 62(2):481–489, 1969.

[51] RF Miller and GS Ansell. Low temperature mechanical behavior of Ni-15Cr-Ai-Ti-Mo alloys. *Metallurgical Transactions A*, 8(12):1979–1991, 1977.

[52] D Raynor and JM Silcock. Strengthening mechanisms in γ' precipitating alloys. *Metal Science Journal*, 4(1):121–130, 1970.

[53] Yi Ru, Haigen Zhao, Heng Zhang, Xinyu Pan, Wenyue Zhao, Yanling Pei, Shusuo Li, and Shengkai Gong. Design for anomalous yield in γ'-strengthening superalloys. *Materials & Design*, 183:108082, 2019.

[54] C Lall, S Chin, and DP Pope. The orientation and temperature dependence of the yield stress of Ni 3 (Al, Nb) single crystals. *Metallurgical Transactions A*, 10(9):1323–1332, 1979.

[55] SM Copley, BH Kear, and GM Rowe. The temperature and orientation dependence of yielding in Mar-M200 single crystals. *Materials Science and Engineering*, 10:87–92, 1972.

[56] S. Takeuchi and E. Kuramoto. Temperature and orientation dependence of the yield stress in Ni {in3} Ga single crystals. *Acta metallurgica*, 21(4):415–425, 1973.

[57] Toshio Saburi, Takatoshi Hamana, Soji Nenno, and Han-ryong Pak. Temperature and orientation dependence of the yield strength of Ni3 (Al, W). *Japanese Journal of Applied Physics*, 16(2):267, 1977.

[58] YQ Sun and PM Hazzledine. A TEM weak-beam study of dislocations in γ' in a deformed Ni-based superalloy. *Philosophical Magazine A*, 58(4):603–617, 1988.

[59] YM Wang-Koh. Understanding the yield behaviour of L12-ordered alloys. *Materials Science and Technology*, 33(8):934–943, 2017.

[60] Tomoo Suzuki, Yoshihiro Oya, and Dang-Moon Wee. Transition from positive to negative temperature dependence of the strength in Ni_3Ge-Fe_3Ge solid solution. *Acta Metallurgica*, 28(3):301–310, 1980.

[61] T Takasugi and M Yoshida. Strength anomaly and dislocation structure at 4.2 k in ni3 (si, ti) single crystals. *Philosophical Magazine A*, 65(3):613–624, 1992.

[62] J.L. Bassani. Single crystal hardening. *Applied Mechanics Reviews*, 43(5S):S320–S327, 1990.

[63] Thomas Gnäupel-Herold, Ganapati Rao Myneni, and Richard E Ricker. Investigations of residual stresses and mechanical properties of single crystal niobium for srf cavities. In *AIP Conference Proceedings*, volume 927, pages 48–59. American Institute of Physics, 2007.

[64] TE Mitchell, RA Foxall, and PB Hirsch. Work-hardening in niobium single crystals. *Philosophical Magazine*, 8(95):1895–1920, 1963.

[65] A.C. Yeh and S. Tin. Effects of ru and re additions on the high temperature flow stresses of ni-base single crystal superalloys. *Scripta Materialia*, 52(6):519–524, 2005.

[66] Stanley P Lynch and S Moutsos. A brief history of fractography. *Journal of Failure Analysis and Prevention*, 6:54–69, 2006.

[67] George A Pantazopoulos. A short review on fracture mechanisms of mechanical components operated under industrial process conditions: Fractographic analysis and selected prevention strategies. *Metals*, 9(2):148, 2019.

[68] Ervin E Underwood. Quantitative fractography. In *Applied metallography*, pages 101–122. Springer, 1986.

[69] André Pineau, Amine A Benzerga, and Thomas Pardoen. Failure of metals i: Brittle and ductile fracture. *Acta Materialia*, 107:424–483, 2016.

[70] Derek Hull. *Fractography: Observing, Measuring and Interpreting Fracture Surface Topography*. Cambridge University Press, 1999.

[71] Donald J Wulpi. *Understanding How Components Fail*. ASM international, 2013.

[72] Jorge Luis González-Velázquez. *Fractography and Failure Analysis*, volume 24. Springer, 2018.

[73] Johan J Moverare, Mikael Segersäll, Atsushi Sato, Sten Johansson, and Roger C. Reed. Thermomechanical fatigue of single-crystal superalloys: Influence of composition and microstructure. *Superalloys*, 2012:369–377, 2012.

[74] A. Sato F. Karlsson M. Hasselqvist R. C. Reed, J. Moverare. A new single crystal superalloy for power generation applications. In *Superalloys 2012*, pages 197–204. John Wiley & Sons, 2012.

[75] Malcolm McLean. *Directionally solidified materials for high temperature service*. Metals Society, 1983.

[76] Daniel Leidermark, Johan J Moverare, Kjell Simonsson, Sören Sjöström, and Sten Johansson. Room temperature yield behaviour of a single-crystal nickel-base superalloy with tension/compression asymmetry. *Computational materials science*, 47(2):366–372, 2009.

[77] Andreas Bezold, Nicklas Volz, Fei Xue, Mathias Göken, and Steffen Neumeier. Anomalous work hardening behavior of a single crystalline co-base superalloy. *Alloys*, 1(3):243–253, 2022.

[78] James G Oldroyd. A rational formulation of the equations of plastic flow for a bingham solid. In *Mathematical Proceedings of the Cambridge Philosophical Society*, volume 43, pages 100–105. Cambridge University Press, 1947.

[79] Carl Ross, John Bird, and Andrew Little. *Mechanics of Solids*. Routledge, 2021.

[80] B.C. Wonsiewicz and R.R. Hart. Finite strain and the 0.01 percent offset yield strength. *Journal of Testing and Evaluation*, 1(5):412–415, 1973.

[81] CS Smith. Proportional limit tests on copper alloys. In *PROC ASTM*, volume 40, pages 864–872, 1940.

[82] Jian-Bo Liu, DD Johnson, and AV Smirnov. Predicting yield-stress anomalies in L12 alloys: Ni3Ge–Fe3Ge pseudo-binaries. *Acta materialia*, 53(13):3601–3612, 2005.

[83] V Paidar, DP Pope, and V Vitek. A theory of the anomalous yield behavior in L12 ordered alloys. *Acta Metallurgica*, 32(3):435–448, 1984.

[84] D Wu, I Baker, PR Munroe, and Easo P George. The yield strength anomaly of single-slip-oriented Fe–Al single crystals. *Intermetallics*, 15(2):103–107, 2007.

[85] Yu N Gornostyrev, O Yu Kontsevoi, AF Maksyutov, AJ Freeman, MI Katsnelson, AV Trefilov, and AI Lichtenshtein. Negative yield stress temperature anomaly and structural instability of Pt_3Al. *Physical Review B*, 70(1):014102, 2004.

[86] Paul A Flinn. Theory of deformation in superlattices. *Transactions of the American Institute of Mining and Metallurgical Engineers*, 218(1):145–154, 1960.

[87] Jiapo Wang, Jianwei Liang, Dongxu Zhang, Yan Peng, and Zhixun Wen. The effect of small orientation deviation from [001] to [011] on high-temperature creep properties of nickel-based single crystal. *International Journal of Plasticity*, 166:103648, 2023.

[88] Akane Suzuki and Tresa M. Pollock. High-temperature strength and deformation of γ/γ' two-phase Co–Al–W-base alloys. *Acta Materialia*, 56(6):1288–1297, 2008.

[89] Joseph R Davis. *Tensile Testing*. ASM International, 2004.